FABRICATION AND CHARACTERIZATION OF THIN-FILM ENCAPSULATION FOR ORGANIC ELECTRONICS

A Dissertation
Presented to
The Academic Faculty

by

Namsu Kim

In Partial Fulfillment
of the Requirements for the Degree
Doctor of Philosophy in the
School of Mechanical Engineering

Georgia Institute of Technology
December 2009

FABRICATION AND CHARACTERIZATION OF THIN-FILM ENCAPSULATION FOR ORGANIC ELECTRONICS

Approved by:

Dr. Samuel Graham, Advisor
School of George W. Woodruff School of Mechanical Engineering
Georgia Institute of Technology

Dr. Bernard Kippelen
School of School of Electrical and Computer Engineering
Georgia Institute of Technology

Dr. David McDowell
School of George W. Woodruff School of Mechanical Engineering
Georgia Institute of Technology

Dr. Sankar Nair
School of Chemical and Biomolecular Egnineering
Georgia Institute of Technology

Dr. Suresh Sitaraman
School of George W. Woodruff School of Mechanical Engineering
Georgia Institute of Technology

Date Approved: [Month dd, yyyy]

ACKNOWLEDGEMENTS

Most of all, I would like to first express my appreciation to my parents for their encouragement, and endless love. Without their help and support, I can't even imagine who I would be. Whenever I am in trouble, their love always guides me on the road of life. I also thank my elder sister and her husband for motivating me to continue my studies.

I acknowledge Prof. Samuel Graham for accepting me as a graduate student and giving me a chance to work in his group. His open mind for discussions and constructive suggestions has motivated me to improve myself and enjoy this work. I also acknowledge his financial support for giving me many chances to present our results and interact with others at conferences. I also thank all my committee members, Prof. Bernard Kippelen, Prof. David McDowell, Prof. Suresh Sitaraman, and Prof. Sankar Nair for their advice and participation in the review and evaluation of this work.

I again acknowledge Prof. Bernard Kippelen for giving me a plenty of chances to test organic electronic devices fabricated by his group, providing access to his students and laboratory equipments. His guidance and expertise allowed me the chance to work efficiently. I am thankful to William Potscavage and his time for making samples, answering my questions, and chatting with me. I thank Prof. Clifford Henderson and his student Annapoorani Sundaramoothi for measuring property of parylene. I also thank Prof. Seunghyup Yoo for his advice about my research and attitude for science.

I want to thank all past and current group members Adam Christensen, Abe Greenstein, Erik Sunden, Ashante Allen, Thomas Beechem, Roderick Jackson, Chris

Ford, Minseok Ha, Mark Gleva, Prem Nagarathnam, Steven Walker, Fernando Reiter, Seokwon Choi, and Yongjin Kim.

I would like to thank my old friends Jinwoo, Juyoung, Taehwan, Hyungrae, Heungsub, Sooki, Jaesan, Chan, Bowoong, and Dohoon who have always been proud of my Ph.D. study in USA regardless of my output. Their overestimating my ability makes me work hard and complete my study. I also thank my University alumni Seol, Iktae, Myungyoon, Donghoon, Sunkyu, Donghyun, Sugnhyun, Jinsik, Woodo, and Bumwoo for fresh news from Korea and welcoming my every visit to Korea. I want to thank all Korean GT tennis club members. I am thankful to Wonjong as my old partner in every double match.

I acknowledge financial support from the National Science Foundation through the Center for Materials and Devices for Information Technology Research (CMDITR).

TABLE OF CONTENTS

LIST OF TABLES

LIST OF FIGURES

LIST OF SYMBOLS AND ABBREVIATIONS

M	Molar mass
δ	Resistivity
ρ	Density
G	Conductance
l	Length of Ca sensor
w	Width of Ca sensor
P	Permeability coefficient
D	Diffusion coefficient
S	Solubility coefficient
e	Porosity
J_{sc}	Short-Circuit Current Density
V_{oc}	Open circuit voltage
V_{mpp}	Voltage at maximum power point
J_{mpp}	Current density at maximum power point
η	Overall power conversion efficiency
P_{in}	Incident light power
I-V	Current-Voltage
L-V	Luminance-Voltage
σ	Residual stress
s	Elastic Stiffness
ε	Strain
v	Poisson's ratio
A	Surface area of indenter

T	Temperature
α	Coefficient of thermal expansion
E	Elastic modulus
d	Thickness of film
m	Mass
R	Radius of curvature
c	Concentration
J	Permeant flux
Q	Cumulative permeation quantity
σ	Standard deviation

OLED	Organic Light Emitting Diode
FOLED	Flexible OLED
PHOLED	Phosphorescent OLED
OPVs	Organic Photovaltaics
OFET	Organic Field Effect Transistor
OTFT	Organic Thin Film Transistor
WVTR	Water Vapor Transmission Rate
OTR	Oxygen Transmission Rate
PECVD	Plasma Enhanced Chemical Vapor Deposition
PVD	Physical Vapor Deposition
ALD	Atomic Layer Deposition
PEALD	Plasma Enhanced Atomic Layer Deposition
SEM	Scanning Electron Microscopy
TEM	Transmission Electron Microscopy

AFM	Atomic Force Microscopy
ITO	Indium Tin Oxide
SS	Steady State
RH	Relative Humidity
Sccm	Standard Cubic Centimeters
RFID	Radio Frequency Identification
FEM	Finite Element Model
FF	Field Factor
RF	Radio Frequency
a-Si	Amorphous Silicon
TMA	Trimethylaluminum
CSM	Continuous Stiffness Method
CTE	Coefficient of Thermal Expansion

SUMMARY

The rapid development of organic electronics is leading to a number of promising devices in the area of energy sources and conservation (e.g., solar cells and solid-state lighting), while also advancing display technology, sensors, and thin-film transistors. One obstacle to this development is the susceptibility of these devices to water vapor and oxygen, which are well known to cause rapid degradation in many organic electronic devices. In order to guarantee the minimum lifetime needed for various applications, high barrier performance encapsulation materials and structures must be developed and has been the object of much experimental research. However, there is a dearth of comprehensive studies which link the characterization, modeling, and integration of ultra-high barrier films with organic electronics. Such studies are necessary in order to advance the understanding of thin-film encapsulation and to find methodologies which greatly improve its performance.

The present work investigates the processing and development of high quality single-layer and multilayer encapsulation architectures for ultra-high barrier films. For compatibility with organic electronics, this study focuses on low temperature fabrication processes which can lead to poor film quality. To circumvent the issue of defects, multilayer encapsulation films with alternating inorganic and organic layers were used to provide ultra-low permeation films. By reducing the complexity of typical multilayer architectures, a new encapsulation processing procedure was developed which combines a plasma enhanced chemical vapor deposition fabricated inorganic film followed by a high quality film deposited by atomic layer deposition. The improvements that this

hybrid film provided were through the quick coating of the device via plasma-based deposition followed by a short atomic layer deposition exposure to seal the defects in the first film. The barrier performance of all thin-film encapsulation was characterized in terms of the effective water vapor transmission rate (WVTR) by using Ca corrosion tests. A detailed study of the water vapor permeation mechanism through thin-film layers was presented. Finally, fully characterized encapsulation layers were integrated with organic solar cells to validate the effectiveness of the barrier layers. The compatibility of the encapsulation process with organic devices was investigated by comparing the performance parameters of organic device before and after encapsulation. The parameters of encapsulated organic devices with various encapsulation structures were compared with their initial values as a function of exposure time to atmosphere to provide a link between effective WVTR and shelf-lifetime of encapsulated organic devices.

CHAPTER 1

INTRODUCTION

1.1 Reliability Issues of Organic Electronic Devices

Over the past decade, rapid advances in organic semiconducting materials and their processing techniques have led to the development of organic light-emitting diodes (OLEDs), organic photovoltaics (OPVs), and organic thin-film transistors (OTFTs) with unprecedented performance (Figure 1.1). Interest in such organic electronic devices arises due to their wide range of tunable properties, multi-functional characteristics, and potential for use in flexible electronics as well as their amenability to wide-area manufacturing processes such as inkjet or gravure printing.[1-3] In light of the many promising results reported in the literature, it is clear that the unique properties of organic semiconducting materials will most likely enable the development of a new class of low-cost electronic devices with highly flexible form factors and properties which are not possible with traditional crystalline semiconductor materials.

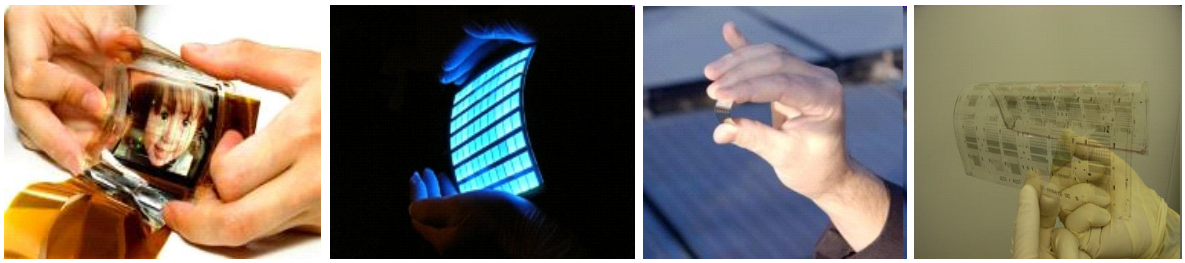

(a) (b) (b) (c)

Figure 1.1 (a) A full color flexible OLED prototype from Sony lab (http://www.digitaltechnews.com/news/2007/05/sonys_flexible.html). (b) OLED as a solid stating light application developed by General Electric and Konica Minolta (www.science.edu/TechoftheYear/EnterNominees.htm). (c) Pentacene/C_{60}-based OPV fabricated on plastic substrate by Bernard Kippelen's group at Georgia Institute of Technology). (d) OTFTs array fabricated entirely by printing process on a plastic film (www.aist.go.jp/2008/20080728/20080728.html

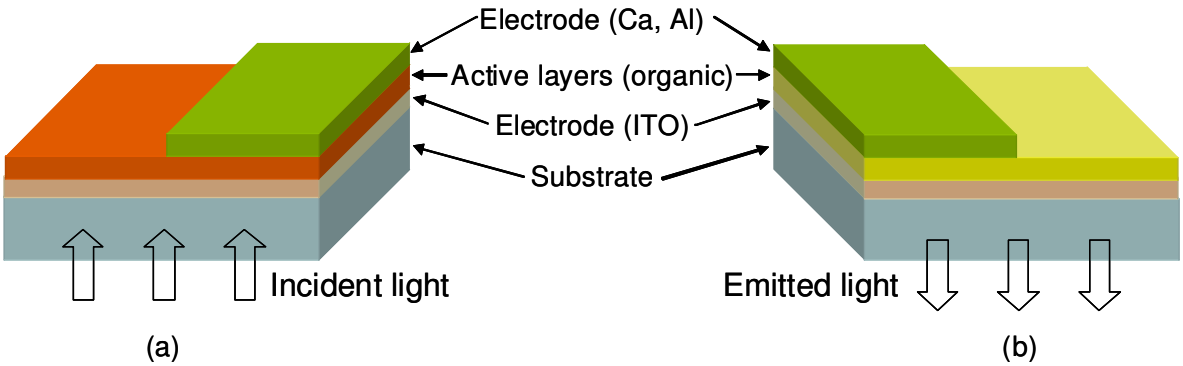

Figure 1.2 Schematic diagrams showing the basic structure of organic diodes: (a) organic photovoltaics and (b) organic LEDs. These devices consist of a transparent anode which is deposited on a substrate followed by the deposition of active layers and a low work function cathode. The device is generally encapsulated to prevent direct exposure to water vapor and oxygen. In the case of polymer substrates, an additional encapsulation layer is generally used on the substrate due to the low barrier properties of polymer substrates.

In spite of the major advances seen in organic devices, their reliability remains one of the greatest challenges which must be addressed prior to wide spread commercial application. Device structures for OLEDs and OPVs are shown in Figure 1.2. Such devices consist of a substrate, a high work function anode, active layers, and a low work function cathode. One of the electrodes is generally transparent. In addition, the devices usually contain some type of encapsulation layer or are hermetically sealed to protect them from exposure to the environment. Device reliability issues, in part, arise due to the environmental instability of both the active materials and low work function electrode in the devices.[1-10] In these applications, low work function metals such as Ca and Li are often used in the cathode in order to obtain efficient electron injection or collection within the device.[11] Low work function metals are highly reactive with oxygen and water vapor and, thus, oxidize very quickly. This results in the formation of insulating oxide barriers, making the injection and collection of charge carriers less efficient. Exposure to water vapor and oxygen in the environment may also result in the formation of black spots in OLEDs, reducing their light output and lifetimes.[12] Another detrimental degradation mechanism which can arise from environmentally-induced

oxidation is delamination within the device. When water vapor permeates through defects into the interface formed by the cathode and an active layer, it may cause chemical reactions which induce outgassing or volumetric expansion leading to delamination.[13, 14]

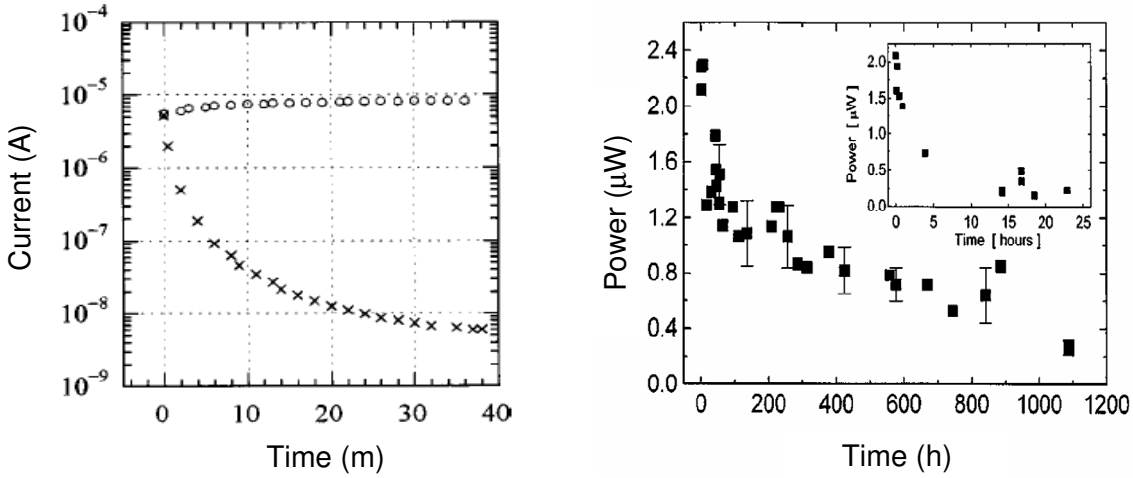

Figure 1.3 (a) Conductance decrease in ambient air for C_{60} thin-film FET at a source-drain voltage of 30 V without alumina covering (crosses) and with alumina covering (circles). Taken from reference. [18] (b) Optical power output of an encapsulated OLED device as a function of time. The inset shows the corresponding response of a bare OLED. Taken from reference.[19]

In addition to the environmentally-induced degradation of the electrodes, environmental exposure of the active layers is also detrimental to the performance of organic electronic devices. Because of direct reactions of water vapor and oxygen with semiconducting small molecules, materials such as C_{60} in organic field-effect transistors (OFETs) have shown rapid degradation of their electrical properties after exposure to air when compared to a transistor with alumina, as shown for instance in Figure 1.3 (a).[15] In the case of OLED applications in Figure 1.3 (b),[16] previous results have also shown that the optical power output rapidly degrades after only 10 hours of exposure to the environment whereas encapsulated devices showed lifetimes at least an order of magnitude longer. Thus, the development of encapsulation technologies is critical to increase the lifetime of organic electronic devices.

1.2 Brief Overview of Existing Encapsulation Technologies

In general, the development of encapsulation technologies is critical to the improvement of lifetime and reliability of organic electronic devices.[13, 16, 17] A number of approaches to encapsulation have been developed including the use of thin-film coatings, metal lids, glass and the sealing of devices between two glass substrates or plastic substrates treated with barrier films.[16, 18] Metal or glass lids with UV-cured sealing epoxy resin have been used for encapsulation as shown in Figure 1.4 (a). An inert gas such as nitrogen or argon fills the sealed volume. Additionally, getter materials such as calcium and barium are used to remove any residual water in the encapsulated volume or water vapor which diffuses through the epoxy sealant.[19] However, these rigid materials are not amenable for use in flexible electronics. Hence, several flexible encapsulation approaches such as barrier-coated flexible lids, ultra-thin glass, and vacuum-deposited thin films have been developed as shown in Figure 1.4 (b) and (c).[20-22] Of the various flexible encapsulation approaches, thin films have attracted the most attention due to their light weight, transparency, and high level of mechanical flexibility. Additional technologies using thin-film barrier layers will be discussed in Chapter 2.

While most of the research in developing encapsulation materials for organic electronics has focused on their barrier performance, other critical aspects must also be considered in the development of this technology. Not only is the development of the encapsulation constrained by the need for a low level of water vapor permeation, but the processing of the encapsulation must also be compatible with organic electronics. For active layers and substrates with low glass-transition temperatures and thermal stability, the processing temperatures at which the barrier layers can be deposited will be limited. This inevitably requires that the inorganic layers which exist in the encapsulation must be deposited at low temperatures for device compatibility if deposited directly on the device. However, processing at low temperature may lead to more defects in the films, limiting

the overall barrier performance.[19] Thus, the development and integration of high-barrier encapsulation films with organic electronics remains a challenging endeavor.

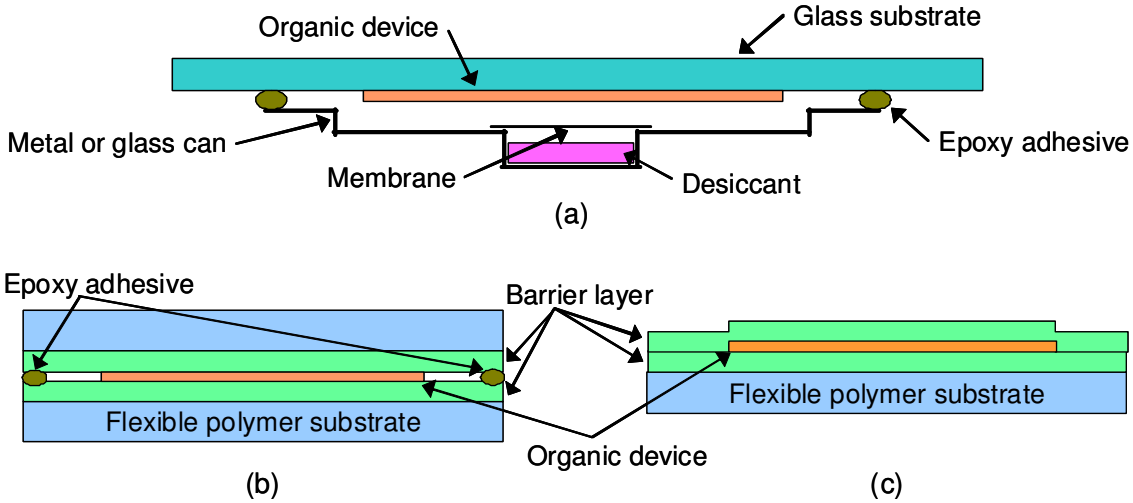

Figure 1.4 Schematic diagrams of encapsulation for OLEDs: (a) typical rigid lid, (b) coated flexible lid, and (c) thin-film.

1.3 Objectives and Organization of Dissertation

As has been discussed above, organic electronic devices have reliability issues which should be addressed prior to widespread commercialization due to their susceptibility of organic devices to water vapor and oxygen. Of the current solutions, thin-film encapsulation is the most promising and challenging encapsulation process. However, its development will allow for unique applications of organic electronics specifically flexible devices. Hence, the primary objective of the present work is to develop high barrier performance thin-film encapsulation which can be integrated with organic devices. First, the fundamentals of diffusion of water vapor and oxygen through single and multilayer films will be addressed. Next, the fabrication and evaluation of barrier layers are presented. Utilizing the Ca corrosion method to quantify ultra low permeation through these films is discussed including permeation mechanism through these films. The second objective is to study the mechanical response of thin films. Starting from the basic understanding of mechanical behavior and limitation of barrier

layers, a highly flexible encapsulation structure is proposed and demonstrated experimentally for the development of flexible organic electronics. Lastly, integration with organic solar cells and their shelf-lifetime is presented to demonstrate the usefulness of the barrier layers and the extended shelf-lifetime.

According to the objectives outlined above, this dissertation is organized as follows. First, the basic principles of water vapor and oxygen permeation through organic and inorganic thin films are reviewed in Chapter 2. The various permeation mechanisms of water vapor and oxygen are reviewed. Barrier performance measurement methods for water vapor and oxygen are introduced in detail for the understanding of the reported barrier performance in the relevant studies. The next section in Chapter 2 introduces and compares recent achievements in various thin-film barrier technologies. The last section briefly covers the basic mechanics of thin-film barrier layers on flexible substrates.

Chapter 3 describes all of the experimental methods used in this study in detail. The fabrication processes for thin films using PECVD, ALD and paryelene CVD are explained. Experimental methods for the measurement of the barrier performance and the mechanical response of these barrier coatings are also explained. Test procedures for device performance organic solar cell are included. In Chapters 4 and 6, the experimental results of original studies on both single and multilayer encapsulation architectures are presented. In the case of multilayer encapsulation in Chapter 4, studies focused on the correlation between the number of barrier layers and the barrier performance are presented. Also, the impact of fabrication processes of thin films on the barrier performance is discussed. Analytical simulations were performed to investigate how permeation properties of individual films impact the overall barrier performance and results are presented in Chapter 5. This study provides a basic guideline for designing barrier layers for each application. A hybrid encapsulation structure, which combines the advantages of single and multilayer structure, is proposed, and the results are presented in

Chapter 6. In Chapter 7, the mechanical response of fabricated thin films is investigated by using nanoindentation and the wafer curvature method. The cracking of various thin films under tensile stress is investigated, and a study of the barrier performance under mechanical deformation is carried out to understand the mechanical limitation of the barrier layers under bending. Furthermore, a newly proposed highly flexible encapsulation structure with a low permeation rate is demonstrated to show its effectiveness as a flexible barrier layer.

Finally, in Chapter 8, the effectiveness of the barrier layers is demonstrated by encapsulating organic devices. The compatibility of the thin-film encapsulation process with organic solar cells is verified by comparing the basic performance parameters of the devices before and after the encapsulation process. The shelf-lifetime of encapsulated organic devices with different encapsulation architectures are investigated to provide a one-to-one correlation between the effective WVTR and the shelf-lifetime. These results provide suggestions concerning the minimum barrier performance required for adequate lifetime of encapsulated organic devices, specifically pentacene/C_{60}-based organic solar cells in the present study.

CHAPTER 2

BACKGROUND AND LITERATURE REVIEW ON ENCAPSULATION

2.1 Introduction

The main goal of this chapter is to provide an overview of thin-film encapsulation technologies for protecting organic electronic devices from water vapor and oxygen in order to extend the shelf-lifetime of devices. We first review the basic principles of water vapor and oxygen permeation through organic and inorganic thin films. The measurement techniques for water vapor and oxygen permeation rates are then introduced in detail with a focus on measuring ultra-high barrier films. Next, we introduce and compare recent achievements in various thin-film barrier technologies comprised of high quality single and multilayer coatings. Along with barrier performance, the extended shelf-lifetime of encapsulated organic devices is discussed. Finally, we briefly cover the basic mechanics of thin-film barrier layers on the flexible substrates. The failures of barrier layers from mechanical deformation and their detection techniques will be presented.

2.2 Basic Principles of Permeation

The basic function of barrier films is to limit the exposure of organic electronics to water vapor and oxygen. This is done by controlling the permeation rate through barrier films. A gradient of the chemical potential such as pressure and concentration is the driving force for the permeation. Formally, the permeation is described as a two-step process combining absorption of a substance into the solid followed by diffusion of the substance.[23] Therefore, in the case of a homogenous film at steady state, the

permeability P is equal to the product of solubility coefficient S and diffusion coefficient D :[24]

$$P = S \bullet D \tag{2.1}$$

The solubility and diffusion coefficients are intrinsic material properties and the permeation rates of barrier films are usually reported in the unit of $cm^3/m^2/day$ at a given temperature and pressure in the case of gas permeation and $g/m^2/day$ at given temperature and concentration (generally described in relative humidity: RH) in the case of water vapor permeation.

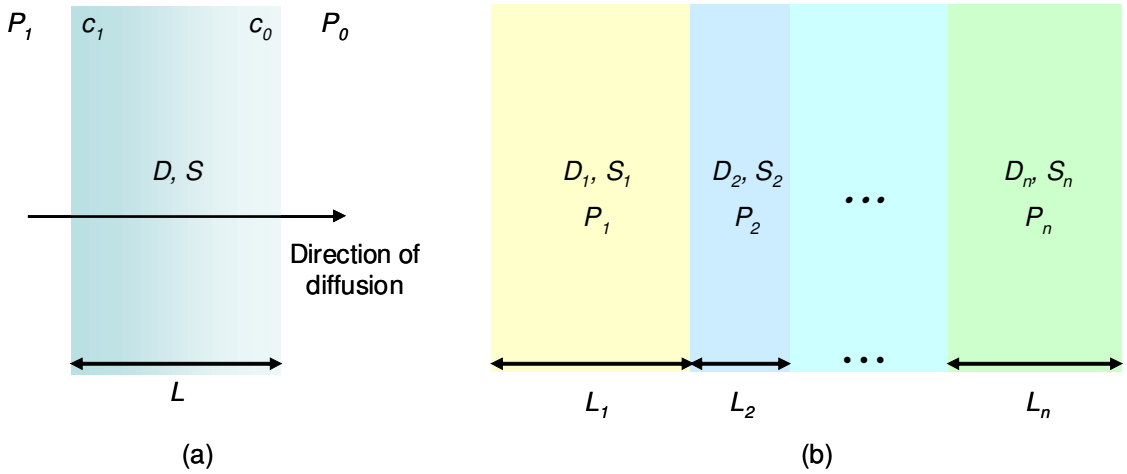

Figure 2.1 Permeation of gas or vapor through single layer (a) and multiple composite (b). *P, c, L, D,* and *S* in (a) indicate vapor or gas pressure, concentration, thickness, and diffusion and solubility coefficients, respectively.

This process also can be described using Fick's first law of diffusion and Henry's law and Figure 2.1 (a) shows permeation model with boundary conditions. The permeant flux J is proportional to the concentration as

$$J = -D \bullet \nabla(c) \tag{2.2}$$

Where, c is the concentration. With the assumption of Henry's law which relates the concentration, c to the partial pressure, ΔP through the linear relationship $c = S\Delta P$, the

concentration in Equation (2.2) can then be replaced using the solubility coefficient and partial pressure. In the case of steady state, well-know equation can be written as

$$J = \frac{DS(P_0 - P_1)}{L} \tag{2.3}$$

and total mass transmitted through this layer can be calculated by multiplying the flux and time.[25] However, the transient study of permeation has attracted much attention due to the introduction of barrier layers having long lag time. In the case of time dependent gas permeation, Fick's second law can be used:

$$\frac{\partial c}{\partial t} = \nabla(D \bullet \nabla c) = D \bullet (\frac{\partial^2 c}{\partial x^2} + \frac{\partial^2 c}{\partial y^2} + \frac{\partial^2 c}{\partial z^2}) \tag{2.4}$$

The diffusion coefficient D is assumed to be concentration-independent and isotropic. Such case is only valid in the absence of chemical reactions between the permeant and solid and gives the well-known solution in the case of infinite source and sink,[26]

$$c(x,t) = C_1(1 - \frac{x}{l}) - \frac{2C_1}{\pi} \sum_{n=1}^{\infty} \frac{1}{n} \sin(\frac{n\pi x}{l}) e^{-Dn^2\pi^2 t/l^2} \tag{2.5}$$

where C_1 is a fixed concentration on one side and l is the thickness of film. In general, the previous equations apply to diffusion through a single-layer film.

In the case of widely used multilayer encapsulation architectures, the diffusion of water vapor and oxygen through multilayer films has become an important problem which must be addressed. The equation for the total permeability coefficient P_T of a multilayer structure with n layers each with a uniform thickness L_n and permeability coefficient P_T as illustrated in Figure 2.1 (b) is

$$\frac{1}{P_T} = \frac{L_{total}}{\frac{L_1}{P_1} + \frac{L_2}{P_2} + \frac{L_3}{P_3} + \cdots + \frac{L_n}{P_n}} \tag{2.6}$$

In Equation (2.6) L_{total} is the total thickness of the multilayer structure. This total permeability coefficient of the multilayer film is derived assuming a constant permeant flux through all layers under steady state conditions. However, recent calculations showed that the permeation rate for a multilayer structure consisting of organic and inorganic layers is determined not only by steady state permeation but also by transient permeation due to long lag time, which can be longer than the required lifetime of organic devices. The transient permeation through multilayer structures can also play significant role in overall barrier performance, by producing an initial region of low permeation rate prior to reaching steady state transport which will be explained in Chapter 6 in detail.

Briefly, the lag time for single-layer barrier film and multilayer film are in the form of equation (2.7) and (2.88), respectively.[25]

$$L = \frac{l^2}{6D} \tag{2.7}$$

$$L = \frac{\sum_{i=1}^{n}\{\frac{l_i^2}{2D_i}\sum_{i=1}^{n}[\frac{l_m^2}{D_m}\prod_{j=1}^{i-1}k_j] - \frac{l_i^3}{3D_i^2}\prod_{j=1}^{i-1}k_j\} + \sum_{i=1}^{n}\{\frac{l_i}{D_i}\prod_{j=1}^{i-1}k_j \sum_{\beta=i+1}^{n}[\frac{l_\beta}{\prod_{j=1}^{\beta-1}k_j}\sum_{m=\beta}^{n}(\frac{l_m}{D_m}\prod_{j=1}^{m-1}k_j) - \frac{l_\beta^2}{2D_\beta}]\}}{\sum_{i=1}^{n}\frac{l_i}{D_i}\prod_{j=1}^{i-1}k_j} \tag{2.8}$$

In Equation (2.8), $K_j=S_j/S_{j+1}$. As shown in Equation (2.7), the lag time for a single-layer film is dependent on the thickness and the diffusion coefficient while the lag time of a multilayer film depends on solubility of the layers as well. It should be noted that analytical approach in this section requires that the transport through all layers behave in a Fickian manner. More analytical simulations and their results for transient permeation studies will be discussed in Chapter 5.

2.3 The Permeation Mechanism of Water Vapor and Gas

It should be noted that the permeation mechanisms of gas and water vapor in organic polymer and inorganic thin films are different. The barrier properties of organic polymers have been investigated and are known well.[27] The internal lattice structure of polymers is dynamic such that the entanglement of polymer chains creates interstitial spaces which can change with time. Water vapor and gas permeate through these interstitial spaces which are often short-lived and of varying size and geometry.[27] In the application of encapsulation for organic devices, single polymer layers themselves have not been employed because they cannot satisfy the stringent criteria for barrier performance. Therefore, polymers coated with an inorganic or multilayer thin film have been used for the achievement of high barrier performance.

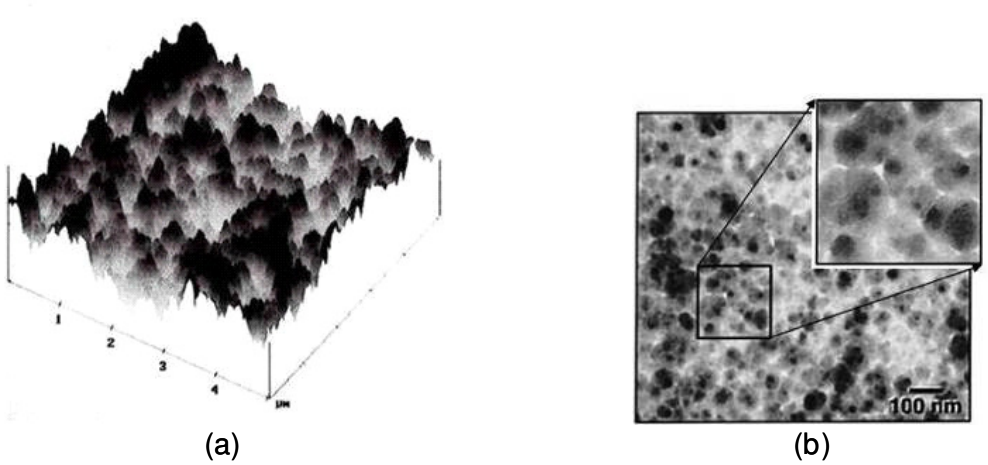

Figure 2.2 (a) AFM image for surface morphology of SiO_x deposited on the PET substrate by PECVD from 45 ° angle. Taken from reference.[29] (b) Energy-filtered (zero loss) TEM image of a relatively poor SiO_x barrier coatings deposited by PECVD on the PET substrate. Enlargement reveals the nano-size defects between adjacent SiO_x grains which provide permeations path for water vapor and gas. Taken from reference.[31]

In lieu of the deficiencies of polymer materials, the development of ultrahigh barrier films has focused on developing inorganic films. However, the permeation mechanisms in inorganic thin films deposited by various techniques such as sputtering, thermal evaporation, and plasma enhanced chemical vapor deposition (PECVD) are still

under investigation. While the diffusion through the broad class of silicon oxides in the bulk form collectively know as "glass" occurs through the very constricted interstitial spaces of the Si-O lattice,[27] the permeation through the deposited thin film is expected to occur through macro defects and nano-scale defects including interstitial spaces.[24] The relative contribution of each component on permeation depends on the size of the permeant molecule and the size and density of defects. These defects originate from the imperfect structure of the deposited inorganic thin film such as voids, columnar structures and grain formation, which have been widely investigated in other reports.[24, 27-30] The atomic force microscope (AFM) image in the Figure 2.2 (a) shows the grain-like structure of PECVD deposited SiO_x film on polyethylene terephthalate (PET) substrate.[27] Transmission electron microscopy (TEM) images in Figure 2.2 (b) reveal the presence of nanoscale defects between adjacent SiO_x grains and these defects can be further reduced by optimizing process condition.[29] For better understanding of imperfect structures of deposited films, Figure 2.3 (a)-(c) show surface morphologies of SiO_x deposited by PECVD on glass substrates with different resolutions which clearly contains voids, and grain formation resulting in relatively rough surface (root mean square (RMS) surface roughness: 3.8 nm). This imperfect structure of the SiO_x provides a permeation path for water vapor and oxygen as illustrated in Figure 2.3 (d) and discussed in other reports.[24, 27-30] Based upon the size of the permeant such as water (diameter: 0.33 nm[31]) and oxygen (diameter: 0.32 nm[31]) molecule and defects, permeation can be categorized into hindered permeation and un-hindered permeation.[24] If the permeant size is comparable to the defect size, the defect provides significant resistance to permeation and vice versa. In most thin film deposition techniques relatively small islands nucleate on the surface of substrate and grow through coalescence with adjacent islands to produce a continuous film.[30] This growth mechanism is not a thermodynamic equilibrium process so it induces imperfect structures which may favor the permeation of water vapor and gas compared to densely packed thin film.

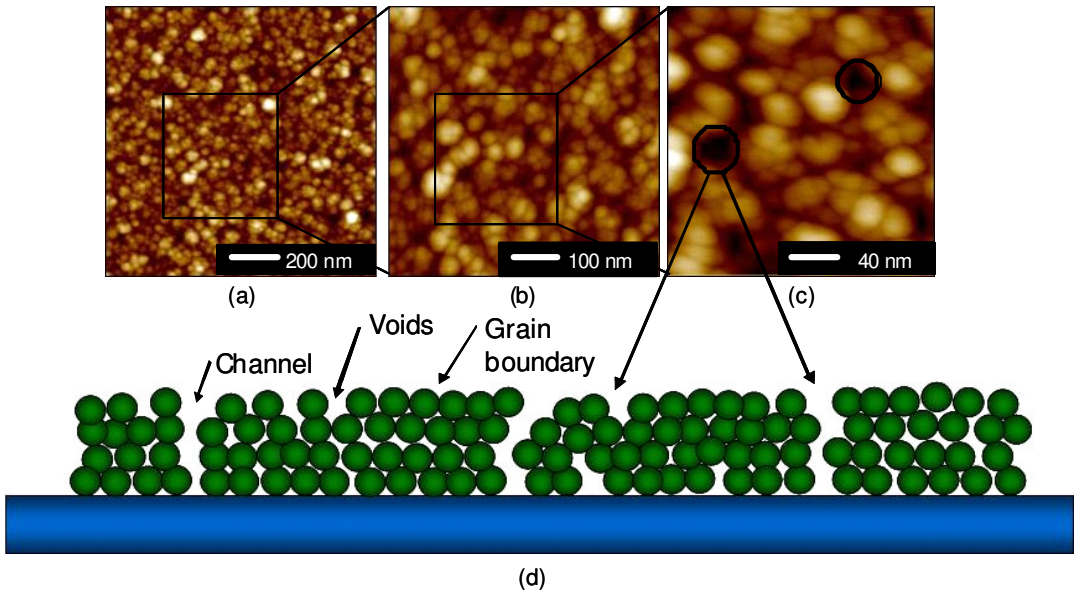

Figure 2.3 AFM images show the surface morphology of SiO_x deposited by PECVD on glass substrates ((a)-(c)) in different resolution on the glass substrate. (d) Schematic illustrates the expected cross-section of SiO_x deposited by PECVD based upon AFM images and shows defects such as void, channel and grain boundary.

Besides these intrinsic defects from the growth mechanism, micro-size defects in films originating from particles on the substrate and geometrics shadowing by structural topography was reported to attribute to defect controlled permeation.[32, 33] Sobrinho et al. reported that these micro-size defects determined dominantly the barrier performance and proposed a defect driven permeation model. They assumed permeation was governed by defect geometries and that the inorganic coatings are impermeable. In this model, the defect size and density in the coatings are dominant factors for permeation so the characterization of defects is critical to predict and understand the permeation. Hence, a new approach to render visible defects on clear plastic substrates was developed by using atomic oxygen etching.[32, 34] More details about this characterization technique are explained in their reports.[32, 34] Briefly, the scanning electron microscope (SEM) image in the Figure 2.4 (a) shows a micro-sized defect caused by a particle and the optical microscope image in Figure 2.4 (b) shows the evolution of defect size with initially a 1 μm diameter after 120 min of atomic oxygen (AO) exposure.[34] Other references also

report that the diameter of defects is ~ 1 μm and a defect density ranges 5 ~ 1000 mm^{-2} according to deposition techniques and materials. These data are summarized in the Table 1.[32, 35-38]

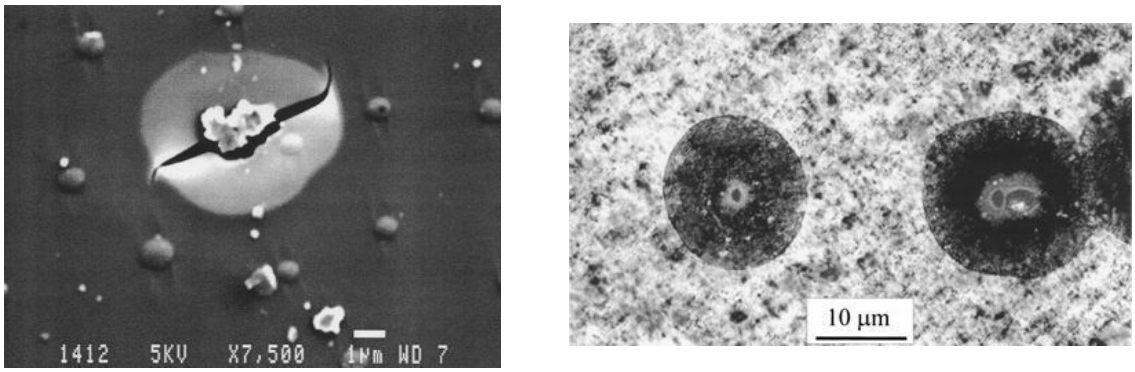

(a) (b)

Figure 2.4 (a) SEM image of defects caused by a dust particle. (b) After 120 min AO exposure, defects can be identified by optical microscope efficiently due to the evolution of defects. Taken from reference.[36]

Table 1. Defect sizes and densities for inorganic films deposited on polymer substrates.

Deposition material	Deposition method	Defect radius (μm)	Defect density ($1/mm^2$)	Substrate
SiO_2	PECVD	0.6	11-1100	PET
Si_3N_4	PECVD	0.6	5-1000	PET
Al	Evaporated	1.0	25-400	PET
Al	Sputtering	2-3	200	PET
AlO_xN_y	Sputtering	0.5-1.4	600	PET
Al	Evaporated	0.4	100-1000	BOPP

For the investigation of diffusion mechanism for water vapor and oxygen, activation rate theory has been widely used in many references.[24, 27, 30, 32] Activation energy for water permeation is a measure of the energy needed to elevate the permeant to the activated state and to distort the barrier matrix so that the permeant may move into the next vacancy. The transport of ideal gas through silicon oxide and glassy polymers below glass transition temperature (T_g) can be described by Arrhenius equation[39];

$$P = P_0 e^{-\Delta E_P / RT} \tag{2.9}$$

where P, P_0 , and ΔE_P, are the permeability, pre-exponential factor, and activation energy for permeation in kJ/mol, respectively, R is ideal gas constant in J/mol/K and T is the temperature in K. Also, this theory can be used to predict the temperature dependency of barrier layers.[40, 41] Sobrinho et al., employed activation rate theory for diffusion of oxygen and water vapor through SiO_x and SiN_x coated PET and bare PET substrate.[32] The activation energy for permeation can be calculated by measuring the permeability at different temperatures. It was found that activation energies for oxygen through bare PET, SiO_x/PET, SiO_x/PET/SiO_x and SiN_x instead of SiO_x are same within the experimental errors suggesting that inorganic barriers such as SiO_x and SiN_x can be considered as imperfect structures allowing gas permeation through defects as discussed above and PET is the dominant rate limiting barrier. In contrast, the activation energies for water vapor through same barrier layer structures differ from that of bare PET substrate as summarized in the Table 2.[32] These results indicate that the diffusion of water vapor deviates from the diffusion of an ideal gas and can't be explained solely by defect dominant permeation mechanisms. It is well known that water vapor interacts strongly with both PET and silicon oxide[27] resulting in more complex mechanism than that of oxygen. Also, other phenomena such as water-induced swelling of polymers[42] and adsorption of water vapor molecules in nanopores of the inorganic barriers are possible reasons for non-Fickian behavior of water vapor through barrier layers.[43] Reported activation energies and their interpretations are still controversial among researchers but it is very persuasive that the interaction of water vapor with barrier layers should be considered to characterize the barrier performance and design adequate thin-film encapsulation for organic electronics.

Table 2. Activation energies for OTR and WVTR through bare PET and inorganic coated PET substrate.

Sample description	ΔE_P for oxygen (kJ/mol)	ΔE_P for water vapor (kJ/mol)
PET	29.3	47.2
SiO_2/PET	30.1	60.5
SiO_2/PET/SiO_2	31.4	62.7
SiN_x/PET	32.8	50.9
SiN_x/PET/SiN_x	31.2	64.5

2.4 Barrier Performance Measurements

The techniques to measure the transmission rate of water vapor and oxygen through barrier layers are essential for the successful design of high quality barrier layers and the requirements of ultra high barrier performance layers for encapsulation of organic electronics have pushed sensitivity limits and accuracy of water vapor permeation tests. Measuring and quantifying ultra-low permeation rates of water vapor (~10^{-6} g/m^2/day) and oxygen with high reliability and accuracy is one of the main challenges of characterizing encapsulation films. The permeation rates of oxygen and water vapor across the barrier layers are characterized in terms of the oxygen transmission rate (OTR) and the water vapor transmission rate (WVTR). Standards (ASTM F1249) and commercial tools (Mocon Aquatran shown in Figure 2.5 (a), modified ASTM 1249) exist for measuring WVTR and OTR independently. Basically, both methods use similar experimental setup in principle as shown in Figure 2.5 (b). The sample in the form of a thin film is placed between wet chamber and dry chambers at ambient atmospheric pressure. Water vapor in the wet chamber flows into the dry chamber through the thin-film sample. Permeated water vapor is carried to a pressure-modulated infrared sensor and absorbs infrared energy. This sensor measures the fraction of absorbed infrared energy and produces an electrical signal which is proportional to water vapor concentration. By comparing the produced electrical signal to that produced with a

calibration film of known water vapor transmission rate, one can calculate the rate of transmitted water through the films being tested.[44] The difference between the two methods is to use a coulometric detector to measure the permeated water vapor in the case of modified ASTM F1249 instead of infrared sensor.

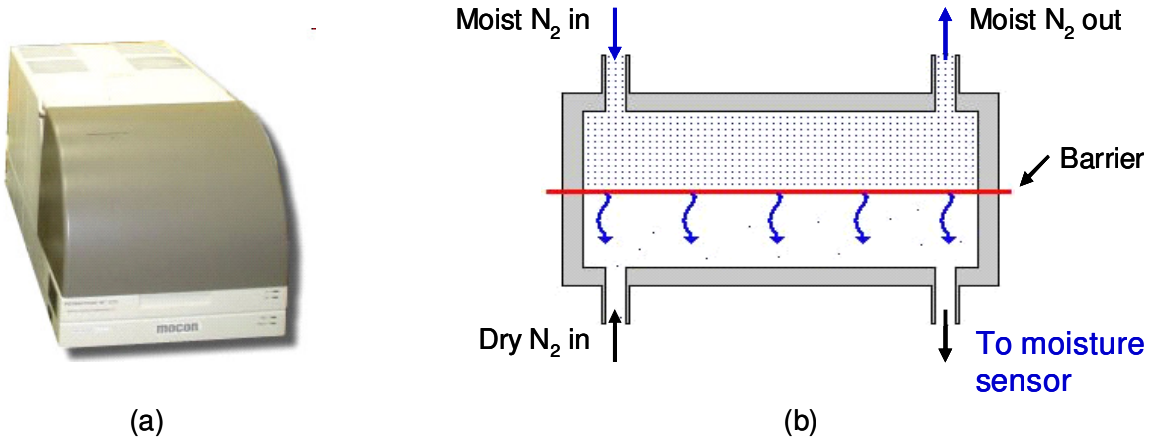

Figure 2.5 (a) Picture shows Permatran-W by MOCON for permeation measurement (http://www.mocon.com/permatran398.php). (b) Schematic shows experimental set-up for ASTM1240.

Typically, commercial systems are useful for analyzing most single-layer and some of multilayer films but are not sensitive enough to detect the ultra-low permeation rates of advanced encapsulation materials, having a lower limit on the order of 10^{-4} g/m^2 /day. On the other hand, the Ca corrosion test, also known as Ca button test, is a widely known method for measuring ultra-low permeation rate barrier films. Calcium is a conducting and opaque metal which becomes non-conducting and transparent after oxidation. It rapidly oxidizes in air due to the highly negative Gibbs free energy of formation of Ca oxides (ΔG = -1200 kJ 1/mole O_2 at room temperature) making it very sensitive for detecting the presence of oxygen and water vapor. Since the oxide is a dielectric and transparent, both of them are possible to monitor the consumption of Ca by either measuring the change in electrical conductance or in optical transparency. Hence, the measurement of Ca conductance or transparency changes provides an indirect method to determine the oxidation and corrosion rates of Ca. Also, this test can distinguish

between bulk permeation and defect-based permeation because the change in transparency is observed using optical microscope or visual inspection. The chemical reaction of Ca in air is as follows the following possible reactions:

$$2Ca + O_2 \rightarrow 2CaO \tag{2.10}$$

$$Ca + 2H_2O \rightarrow Ca(OH)_2 + H_2 \tag{2.11}$$

It has been reported that the reaction with oxygen accounts for less than 5 % of Ca degradation.[45] Hence, the reaction with water in Equation (2.11) dominates the Ca oxidation in the presence of both water vapor and oxygen. However, any measurement of Ca conductance change as a function of time accounts for the permeation rate of both water vapor and oxygen so must be viewed as an effective permeation rate (effective WVTR). In such testing, it is impossible to separate the contribution from either water vapor or oxygen to the Ca corrosion.[45] It should be noted that such distinction between WVTR and effective WVTR is often not discussed in many literature reports using the Ca tests for permeation measurements. For the measurements included in this report as well as those cited from the literature using Ca corrosion test, we will utilize the term effective WVTR to denote the combined effects of water vapor and oxygen permeation. One of the methods to monitor the calcium corrosion is through electrical conductance measurements. Figure 2.6 (a) shows an example of the experimental set-up for monitoring electrical conductance of Ca. In the suggested set-up, a 4.5 × 7 mm^2 Ca sensor and Al interconnects for conductance measurements were used. An encapsulation layer which we study is deposited on top of Ca sensor and conductance change of Ca sensor is monitored by using data acquisition system. The effective WVTR can be determined by monitoring the time rate of change of the electrical conductance of Ca through the use of Equation (2.12).

$$WVTR\,[\mathrm{g^{-1}\ m^{-2}\ day^{-1}}] = -n\,\delta_{Ca}\,\rho_{Ca}\,\frac{d(G)}{dt}\,\frac{l}{w}\,\frac{M(H_2O)}{M(Ca)}\,\frac{Area\,(Ca)}{Area\,(Window)} \qquad (2.12)$$

In Equation (2.12), n is the molar equivalent of the degradation reaction which is assumed as $n = 2$ due to the dominant reaction with water, δ_{Ca} and ρ_{Ca} are the Ca resistivity (3.4×10^{-8} Ω m) and density (1.55 g/cm^3), respectively, while G is the conductance of the Ca and the value of $d(G)/dt$ in equation from the linear fitting in the conductance change versus time as shown in the Figure 2.6 (b). Also in Equation (2.12), $M(H_2O)$ and $M(Ca)$ are the molar masses of water vapor and of Ca, respectively, while l and w are the length and width of Ca sensor, respectively. The ratio of the area of the Ca sensor to the area of the window for water permeation and the ratio of the length is unity due to the geometry of the experimental set-up. Measuring the electrical conductance as well as measuring the optical transmittance is available for the Ca corrosion test. The latter needs no electrical contact for the conductance measurement but needs an optical microscope or camera for the transmittance measurement. Briefly, this test tracks changes in optical transmittance as shown in Figure 2.7[46] instead of electrical conductance resulting from the reactivity of Ca with water vapor and oxygen in air.[40] Hence, it can distinguish between bulk permeation and defect-driven permeation. However, it still cannot distinguish the permeation caused by water vapor and oxygen because both can degrade Ca sensor resulting in changes in optical transmittance.[47] More details about Ca corrosion testing can be found in detail in other references.[45, 46, 48] The use of Ca corrosion testing has allowed the measurement of effective water vapor transmission rates on the order of 1×10^{-7} g/ m^2/day.[40],[46] Hence, Ca corrosion testing is one of the most promising candidates for measuring ultra-high performance barrier films required for organic electronics.

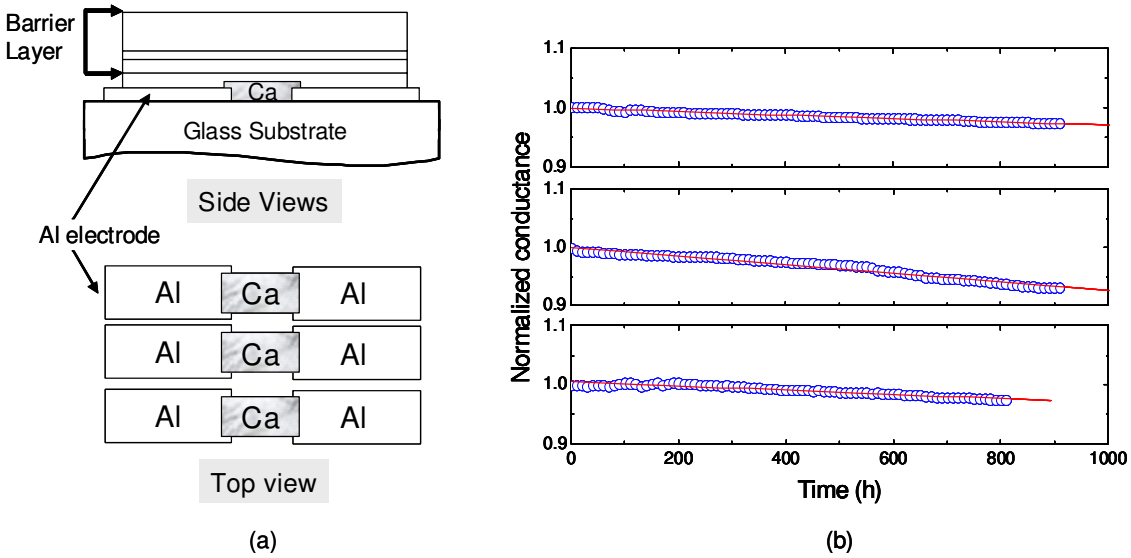

Figure 2.6 (a) Side view of Ca test cell and barrier layer on both Ca (300 nm) and the glass substrate. Top view of Ca test cell with Al electrical contacts. (b) Normalized conductance change as a function of time with linear fit. Symbols are experimental data and solid lines are linear fits corresponding to the value of *d(G)/dt* in equation (2.12).

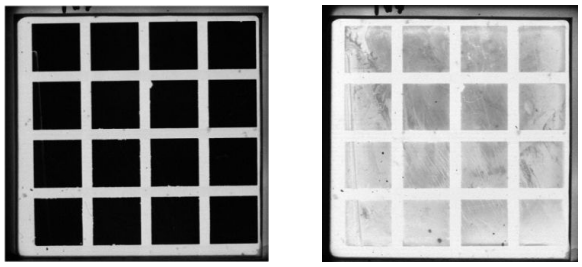

Figure 2.7 Examples of oxidation of optically Ca corrosion test. The Ca square patterns are 5 mm wide and each shows before oxidation (a) and after oxidation (b). Taken from reference.[48]

In order to measure the effective WVTR accurately using electrical monitoring of Ca corrosion, it is assumed that the oxidation takes place uniformly through the encapsulation barrier film. The effect of localized oxidation of the calcium due to defects along the sample edge (side permeation) or defects locally concentrated within the film will give erroneous values of effective WVTR. To check for uniform permeation through the coatings, a visual inspection of the Ca can be performed to observe whether or not the oxidation occurs in a localized region. Typical results from such inspections are shown

in Figure 2.8 (a), (b), and (c) for Ca encapsulated by PECVD deposited SiO_x and CVD deposited parylene thin films. It is evident from Figure 2.8 (a)-(c) that the oxidation occurs evenly and there is no side permeation. The Ca layer becomes transparent and non-conducting, revealing a symbol which was hidden behind the sample. In the case of Figure 2.8 (d) and (e), the Ca was not oxidized evenly due to side permeation and local defects, respectively. Such cases must be excluded from the calcium corrosion test.

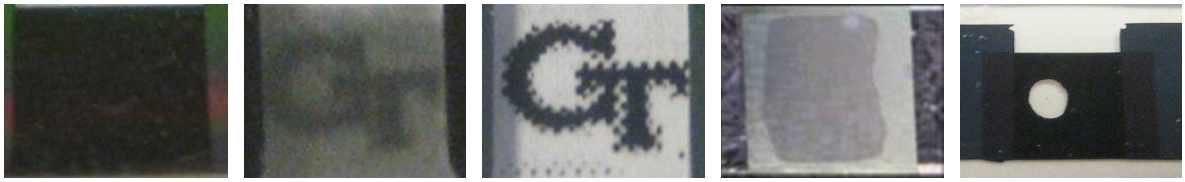

Figure 2.8 Photographs showing the oxidization of an encapsulated Ca layer as a function of time. Pictures (a), (b), (c) show homogenous oxidation, (d) and (e) show non-homogenous oxidation due to side and local permeation.

2.5 Thin-Film Barrier Technologies for Organic Devices

The relatively strong sensitivity of organic devices to water vapor and oxygen, which induces degradation, places stringent demands on the barrier performance of encapsulation. The most stringent barrier performance values estimated to be necessary for adequate lifetimes in OLEDs are on the order of 10^{-6} g/m^2/day for WVTR and 10^{-3} - 10^{-5} cm^3/m^2/day/atm for OTR.[19] Literature reports for OPVs suggest values which are on the order of 10^{-4} - 10^{-6} g/m^2/day for WVTR and 10^{-3} - 10^{-5} cm^3/m^2/day/atm for OTR as shown in Figure 2.9.[49] In general, the true encapsulation requirements for many OPVs and OLEDs are not known and remain the subject of reliability and lifetime studies. Very few studies have linked WVTR measurements with lifetime studies of devices.[18, 50, 51] Thus, a one-to-one correlation between these parameters is difficult to make at this present time for many organic electronic materials and devices. Overall, the barrier requirements of a particular organic device will ultimately depend on the structure and

materials used in fabricating the device as well as the functional requirements of the device itself.

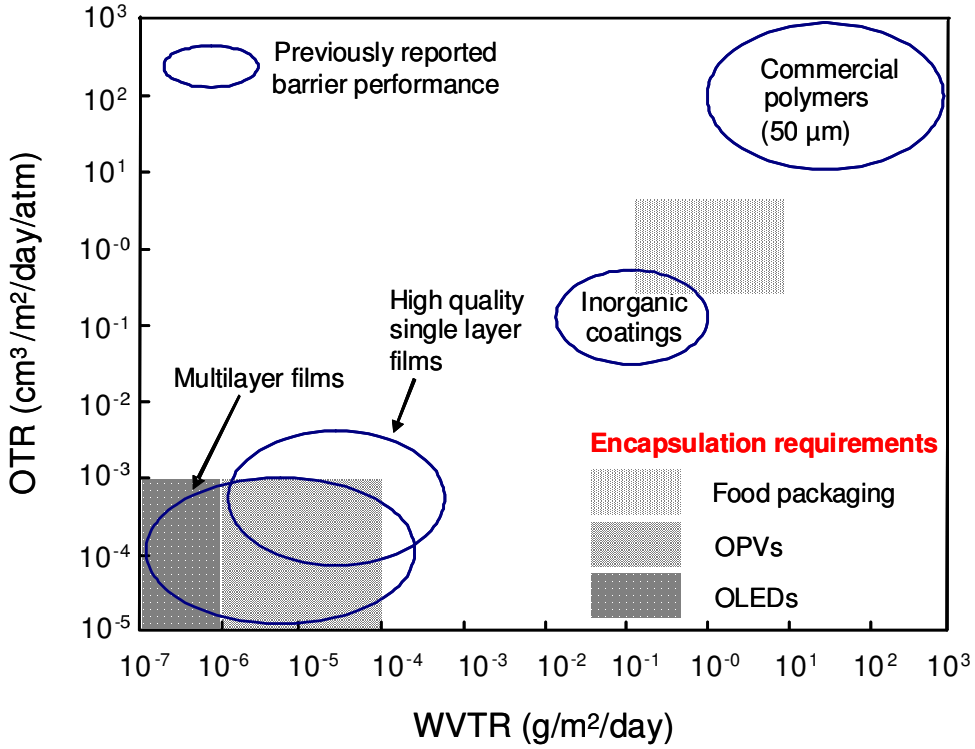

Figure 2.9 Estimates of barrier performance requirements for a number of technological applications, including organic electronics, along with the reported barrier performance for various encapsulation technologies. Adapted from references [21], [30], [51], [54] and [84].

Much of the thin-film encapsulation technology for organic electronics has been developed in the food and pharmaceutical industries for product packaging. Water vapor transmission rates of many of the monolithic polymer films used in food and pharmaceutical packaging range between 1 - 40 g/m^2/day as seen in Figure 2.9.[19, 28, 52] To improve the barrier performance of monolithic polymers, vacuum-deposited inorganic thin films are often used and have been shown to improve the overall barrier performance by a factor of 10 - 100 (Figure 2.9). However, most of the thin-film coating materials developed for the food and pharmaceutical industries are inadequate for use in protecting organic electronics. Thus, research in the development of ultra-barrier encapsulation films is necessary for the commercialization of organic electronics.

2.5.1 Single-Layer Thin-Film Encapsulation

The barrier performance of inorganic materials is the most promising for the development of thin-film encapsulation with the requirements necessary for improving the lifetime and reliability of organic electronics. Single-layer encapsulation films are quite attractive since they simplify the manufacturing process as compared to other multilayer thin-film encapsulation methods which require multiple processing steps. However, inorganic films are limited in their performance mainly due to the presence of defects in the films which provide pathways for water vapor and oxygen to permeate through the barrier layers (See Figure 2.3 (d)). Thus, the main research objective in developing single-layer encapsulation films through methods such as physical vapor deposition (PVD), PECVD, ALD and Plasma enhanced ALD (PEALD) has focused on the reduction of defects to improve barrier performance. At present, the leading processing methods for developing single-layer encapsulation films are based on PECVD and ALD and involve the use of inorganic oxides from the Si-O-N and Al-O-N systems. PECVD is an attractive manufacturing technique due to its high deposition rate as compared to ALD (~ 2 orders of magnitude faster). Most commonly, PECVD-deposited SiO_x and SiN_x films have been utilized to create single-layer barrier films for organic electronics at low deposition temperatures.[53, 54] However, these films contain sufficiently high defect densities which can result in effective WVTR values greater than 0.01 $g/m^2/day$, which are orders of magnitude higher than the target requirement of organic electronics.[52, 54, 55]

As previously stated, few studies correlate the lifetime of devices with known permeation rates in encapsulation layers. Rather, feasibility of encapsulation layers are generally shown by demonstrating improved lifetimes by integrating them with actual devices. For instance, W. Huang et al. reported that the lifetime of encapsulated OLEDs containing a single-layer of PECVD SiN_x was 600 h as compared to 6 h for a bare device (the WVTR of the SiN_x film was not reported in this case).[55] Recently, advances in

PECVD processing of SiO_x:H films have shown remarkable protection ability for OLED devices.[56] By using HDMSO and O_2 as precursors for deposition, researchers found that it was possible to deposit a single composite layer film which consisted of SiO_2 and silicone. While the WVTR of these films has not been measured, data show that they were able to protect OLED devices up to 7,500 h when stored at 65 ºC in 85 % relative humidity (RH).

Promising single-layer encapsulation films have also been achieved using Al_2O_3 deposited by ALD.[52, 57-59] ALD deposited films are desirable due to their high density, low number of defects, and ability to conformally coat surfaces at relatively low temperatures. ALD deposition is a layer by layer buildup of materials beginning with chemisorption of molecular precursors. These precursor gases are introduced into the deposition chamber with an inert carrier gas to form a monolayer coverage on the surface of the sample. Excess precursor is then removed by purging with an inert gas followed by the introduction of the next precursor. These processes are repeated and can produce high quality films with featureless microstructure and conformal coatings. While the measured effective WVTR of the best performing ALD barrier is 1.7×10^{-5} g/m^2/day for 25 nm of Al_2O_3 deposited on a PEN substrate,[60] there was no attempt to integrate such a film with an actual device to observe its impact on lifetime in this report. Other attempts to measure the barrier performance of ALD deposited Al_2O_3 also show variability in the effective WVTR, being as high as 1×10^{-3} g/m^2/day using a tritiated water measurement technique.[40] In addition, laminated structure consisting of Al_2O_3 and ZrO_2 and dual layer structure using SiO_x and Al_2O_3 deposited by ALD have shown excellent barrier performance.[61, 62] While these structures can be considered as multilayer structure due to different materials, they are introduced here because all of them are fabricated using only ALD. Meyer et al. used nano-laminated structure consisting of alternating 2.6 nm thick Al_2O_3 and 3.6 nm thick ZrO_2 film with total thickness of 100 nm deposited at 80 °C and compared its barrier performance with single Al_2O_3 layer with same thickness.[41]

Besides preventing corrosion of Al_2O_3 layer by water vapor, ZrO_2 layer suppress the formation of voids in the Al_2O_3 layers observed in neat Al_2O_3 by stopping the accumulation of unreacted Al-OH species possibly resulting high barrier performance. Also, an Al_2O_3 layer combined with SiO_2 deposited by ALD at 175 °C was reported to improve barrier performance further and this improvement is not explained solely by lamination theory.[62] This improvement by combining two layers argued that SiO_2 layer is filling pinhole defects in the Al_2O_3 layer resulting in further improvement.

The use of Al_2O_3 deposited by ALD has been demonstrated on a number of occasions to provide excellent extended lifetime of encapsulated OLEDs and OPVs. For instance, pentancene/C_{60}-based organic solar cells encapsulated with 200 nm of Al_2O_3 by ALD were shown to be stable for 6,000 h in ambient conditions with negligible deterioration in properties as shown in the Figure 2.10.[57] ALD encapsulation process on the device was performed at a temperature of 100 ºC and any negative impact on the device performance was not found except thermal annealing effect which was already reported previously.[63] Top emitter OLEDs encapsulated with Al_2O_3 deposited by ALD at 100 ºC which is the primary moisture barrier were shown to maintain excellent performance more than 1,000h in conditions of 85 ºC and 85 % RH.[59] While these films show excellent encapsulation performance, their relatively slow deposition rate as compared to PECVD-based methods make them more difficult to use in low-cost mass manufacturing processes. To overcome these long time process issues in ALD, Kim et al. proposed a hybrid encapsulation structure which combines the advantage of fast PECVD deposition and high quality film deposition by ALD.[51] Here, devices were first coated with a layer of PECVD SiO_x or SiN_x which was then sealed with 10-50nm of Al_2O_3 by ALD. Encapsulated pentacene/C_{60}-based organic solar cell maintained their device performance up to 6,000 h with an effective WVTR on the order of 10^{-5} g/m^2/day effective WVTR measured by Ca corrosion test.

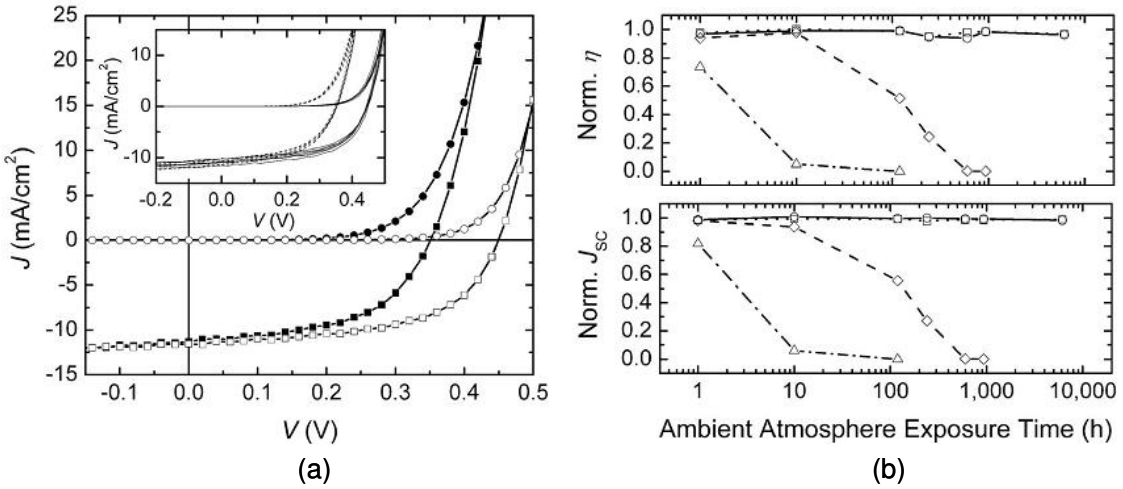

Figure 2.10 (a) Electrical characteristics measurement of pentacene/C_{60}-based solar cells before (filled shapes) and after (empty shapes) deposition 200 nm thick Al_2O_3 by ALD. (b) Relative change in η (top) and J_{SC} (bottom) of encapsulated solar cells with UV epoxy (dashed line, diamond), Al_2O_3 (dotted line, square), and Al_2O_3 and UV epoxy (solid line, circle). Dash-dotted line with triangle is a reference sample without encapsulation. Taken from reference.[59]

Besides the widely used deposition technique such as PECVD and ALD, different attempts to encapsulate organic devices with single layers have been made. For instance, Jung et al. reported that encapsulated by tetratetracontane (TTC) [n-$C_{44}H_{90}$] OTFTs maintain their performance up to 40 days in ambient conditions. TTC (96 % purity), which is hydrophobic, closely packed, and highly crystalline,[64] was deposited directly on OTFTs by thermal vacuum evaporation with thickness of 200 nm.[65] In addition, 100 nm thick SnO_2 fabricated by ion beam-assisted deposition (IBAD) was used to encapsulate OTFTs by Cho et al.[66] They reported that the mobility of device was sustained up to 30 days. Furthermore, spin - casted TiO_x was employed as passivation layer for protecting OFET as well as scavenging layer for recovering degraded device from dipping in water and exposure to air.[66] Encapsulated OFETs based on P3HT and PCBM show extended lifetimes greater than 500 h and 2000 h, respectively. Besides the barrier layer performance, Figure 2.11 (a)-(c) show recovering effects by comparing the transport properties of device either with or without as well as before and after TiO_x

coating.[66] However, reported lifetimes of either TTC, SnO_2 or TiO_x encapsulated organic devices still need to be extended up to 10,000 hr for real application. Furthermore, it is important to note that systematic study between the barrier performance and the lifetime of encapsulated organic device should be investigated to continue to understand barrier performance needs for specific material systems.

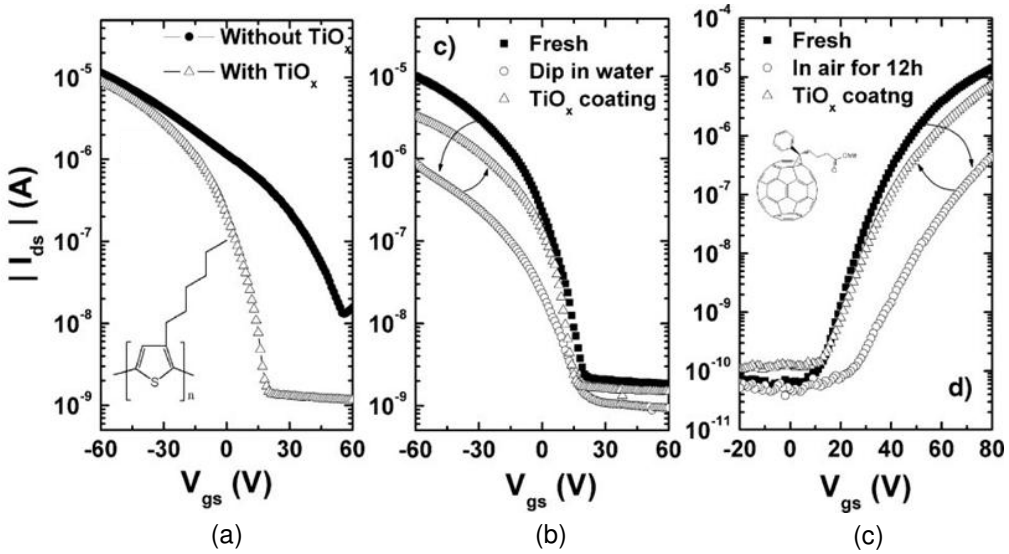

Figure 2.11 (a) Transport characteristics of P3HT FETs with and without TiO_x deposited by spin-casting in air. (b) Recovery effect of TiO_x layer on the degraded P3HT FET after being dipped into deionized water for 15 s. (c) Recovery effect of TiO_x layer on the degraded PCBM FET after storage in air for 12 h. Taken from reference.[68]

2.5.2 Multilayer Thin-Film Encapsulation

Multilayer films are widely used to encapsulate organic electronics and often consist of alternating organic and inorganic multilayers.[18, 19, 67-70] Other examples of multilayer films include alternating layers of inorganic materials such as SiN_x and SiO_x deposited by PECVD or the combination of Al_2O_3/SiO_x deposited by ALD.[60, 62, 71] The multilayer film approach was developed to circumvent the defect issues limiting the barrier performance of single-layer films. By applying multilayer films with alternating materials, defects which span the entire thickness of the individual inorganic layers are interrupted and do not channel continuously through the film structure. This structure

creates a tortuous path resulting in very long effective diffusion pathways, increasing the barrier performance as illustrated in Figure 2.12.[72] In general, the barrier performance of multilayer films is better than the individual films by 3 - 4 orders of magnitude. While a number of polymer films have been used as the "defect interruption layer" in these multilayer structures, most multilayer systems have been able to achieve very low effective WVTRs ($<10^{-4}$ g/m^2/day), showing little dependency on the permeation rates of the specific polymers used in the architecture. While it is clear that controlling the defects in the inorganic layers by applying organic layers is very important, it is still inconclusive which properties and characteristics, beyond planarization and smoothing, the organic layers should possess. Greener et al. investigated the effect of organic layer thickness on the overall barrier performance through a numerical simulation.[73] It is assumed that the inorganic layer is impermeable to water vapor and permeation only occurs through the defects of inorganic layer as illustrated in the Figure 2.13 (a). Based on the ratio of polymer layer thickness to defect size, the plot of WVTR was divided into two distinct regimes as shown in the Figure 2.13 (b). While numerical simulation suggests that dimensionless WVTR is dependent on the thickness of organic layer in the Regime 1, WVTR in Regime 2 is no longer dominated by organic layer thickness. The latter case suggests that there is no additional tortuous path effect from the multilayer structure so it is desirable to design the multilayer structure within the Regime 1. However, there should be a trade off between the thickness of organic layer and the ability of decoupling the defect by organic layer. It is due to the fact that thinner organic layer is beneficial for the barrier performance according to simulation results but thin organic layers cannot passivate or decouple the defects in inorganic layer efficiently. Hence, those issues should be considered during the design of multilayer encapsulation films.

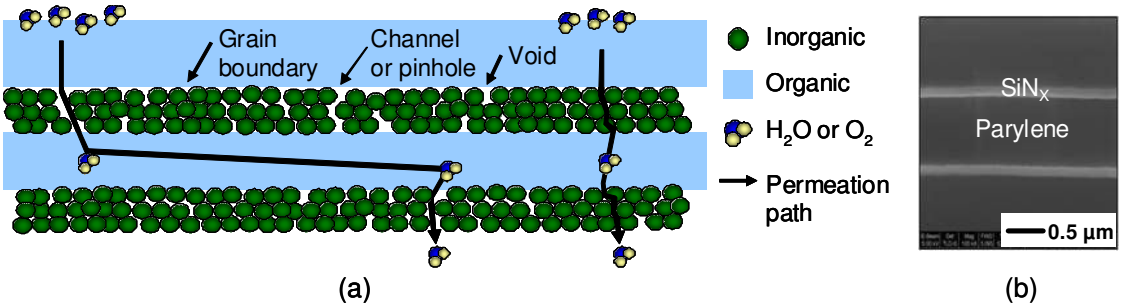

Figure 2.12 (a) Tortuous water permeation path through organic/inorganic multilayer structure. (b) Focused ion beam image shows cross-section of organic/inorganic multilayer structure. Bright films are 100 nm-thick SiN_x and dark films are 1µm-thick parylene. Image taken by Sarah Wagner from the Air Force Research Laboratories, WPAFB, OH.

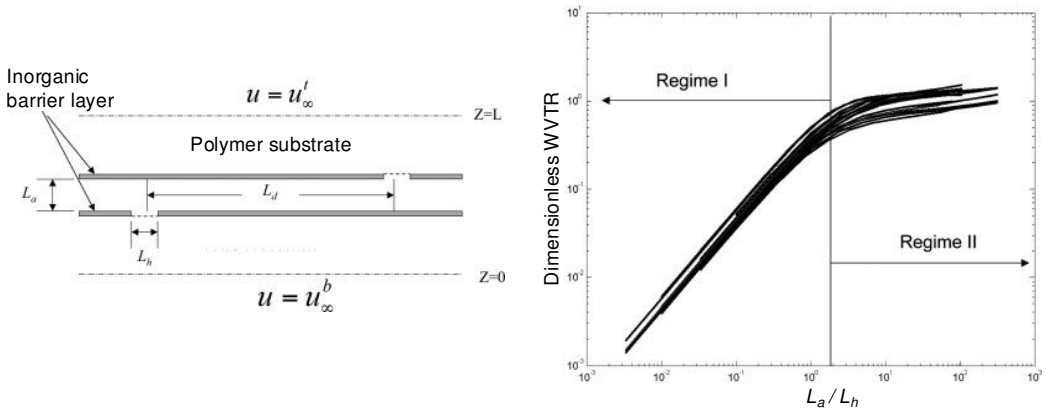

Figure 2.13 (a) Illustration shows the geometry of a laminated structure by organic adhesive. L_h and L_a are the size of defect and the thickness of organic adhesive layer, respectively. (b) Numerical simulation results for Dimensionless WVTR versus the ratio of adhesive thickness to the defect size. Taken from reference.[75]

Commercial companies have reported multilayer barrier coatings with low effective WVTR, such as Barix™ from Vitex with an estimated effective WVTR equivalent to 2×10^{-6} g/m^2/day at ambient conditions measured using Ca corrosion tests.[74] This geometry uses several dyads of PVD AlO_x and UV curable acrylate monomers which can be deposited in a roll-to-roll process in vacuum and the cross-section of this geometry is shown in Figure 2.14 (a). T.-N. Chen et al. reported that the effective WVTR of their combined SiO_x/SiN_x/parylene barrier structure on polycarbonate substrates was found to be 2.5×10^{-7} g/m^2/day at 25 °C and 45 % RH.[68] These values

are to the best of our knowledge the lowest effective WVTR measurements reported and are at least two orders of magnitude lower than those obtained by single-layer encapsulation films. Alternatively, General Electric has developed a graded barrier layer by PECVD and its cross-section is shown in the Figure 2.14 (b).[75, 76] It consists of a single graded layer made up of alternating organic and inorganic layers deposited by PECVD at 55 °C, and its total thickness is less than 1 μm. A combination of organosilicon precursor and Ar gases were used for organic layer and this process creates organic material (SiO_xC_y) having less than 10 GPa modulus. The inorganic process used a combination of silane (2 % silane diluted in He), ammonia, and oxygen gases to create SiO_xN_y having the modulus ranging from 100 to 500 GPa. Reported effective WVTRs for various graded films range from 5×10^{-6} g/m^2/day to 5×10^{-5} g/m^2/day. While multilayer films show high barrier performance, details of the impact of their structure on encapsulation behavior has not been reported.[75, 76] Thus, it is difficult to relate structure, permeation rates, and device lifetime requirements for the development of advanced encapsulation films.

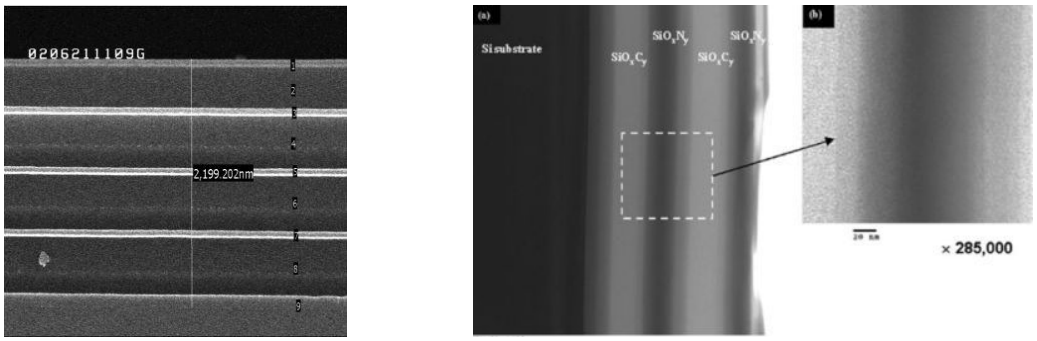

Figure 2.14 Cross-section SEM image of Barix^{TM} encapsulation is shown in (a). Taken from reference.[76] Cross-section transmission electron microscopy (TEM) images of graded UHB coating by GE with low magnification (b) and high magnification. Taken from reference.[77]

In the case of the barrier performance of multilayer structures, it should be noted that the results of multilayer encapsulation do not strictly represent the steady state

permeation rate,[25] since there has been few experimental report about the lag time of multilayered barriers. Recently, analytical calculations indicate that lag time can be up to several years in the case of multilayer barrier systems. Graff et al. reported that obtained results of WVTR are limited not by steady state diffusion but by lag-time effects induced by the extremely long effective water permeation path, especially in the case of multilayered barrier layer as shown in the Figure 2.15.[25] They calculated 1,752 h (~73 days) lag time in the case of five - dyad structure with defect spacing 100 μm as presented in the Figure 2.15 (b) based upon analytical solution. However, this calculation was based upon the assumption that the permeation is controlled dominantly by micro-size defects and sufficient defect spacing (i.e. defect size; ~2 μm, defect spacing; > 100 μm) as shown in the Figure 2.15 (a) and inorganic coatings are assumed to be impermeable. This increased lag time is due to the fact that permeated water vapor through defect in the first inorganic layer should travel along the organic layer before the next defect in the second inorganic layer as illustrated in the Figure 2.15 (a). On the other hands, Tropsha et al. reported that great care for keeping the substrate clean and enough thick deposition over the critical thickness can remove most of micro-scale defects.[27] Dominant water permeation occurs though "imperfect" structures which is an irregular surface array of grain-like structures caused by a thermodynamically non-equilibrium deposition process.[24, 27-30] However, there are still controversial issues in permeation mechanism and some disagreement over the dominant source for permeation through single inorganic and multilayer structure. Therefore, at this stage, it is recommended that the barrier performance of multilayered encapsulation should be investigated by means of the permeability measurement and the lifetime of encapsulated organic device together.

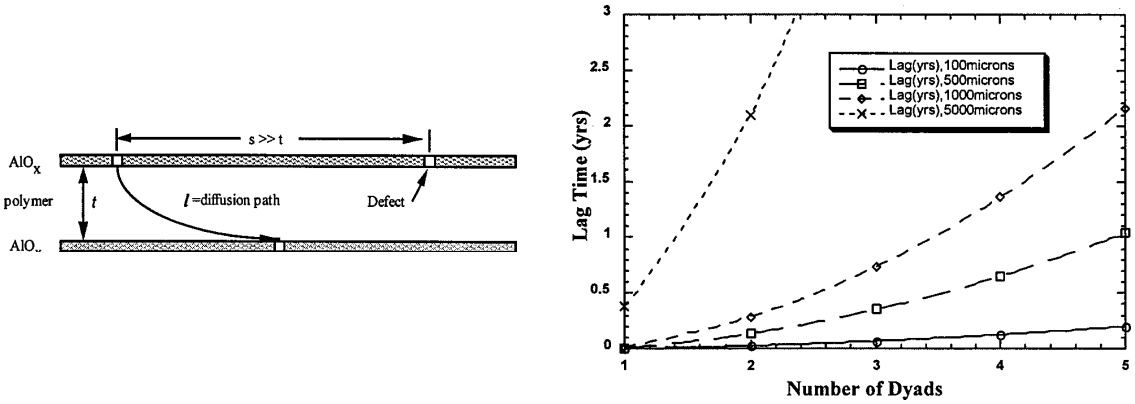

Figure 2.15 (a) Schematic illustration of the effective diffusion length *l* of the polymer layer (approximately half of the defect spacing in Al_2O_3 layer). (b) Calculated lag time as a function of polymer/Al_2O_3 dyads and defect spacing. Taken from reference.[27]

As in the case of single layer films, these multilayer films provide extended lifetimes of encapsulated organic devices. Chwang et al. reported that the lifetime of 3700 h and 2500 h for multilayered encapsulated phosphorescent OLEDs (PHOLEDs) fabricated on glass and barrier coated plastic substrate, respectively, at ambient condition as shown in the Figure 2.16 (a).[70] This encapsulation consists of 4 – 5 pairs of alternating Al_2O_3 and polyacrylate (Barix^{TM} encapsulation) and the total thickness is 5 - 7 μm. Recently, Lungenshmied et al. used alternating SiO_x and organosilicon deposited by PECVD on the PEN substrate.[77] The SiO_x was deposited using volatile organosilicon under oxidative plasma condition and organosilicon was produced from similar organosilicon with non-oxidizing plasma. Encapsulate organic solar cells based on MDMO-PPV devices sustain their function up to 3000 h. By using more stable P3HT for the device, the lifetime was extended to approximately 6,000 h with the same encapsulation structure as shown in the Figure 2.16 (b). These results suggest that developing ultra-high barrier performance encapsulation layer as well as more stable materials for organic device is important for extended lifetime.

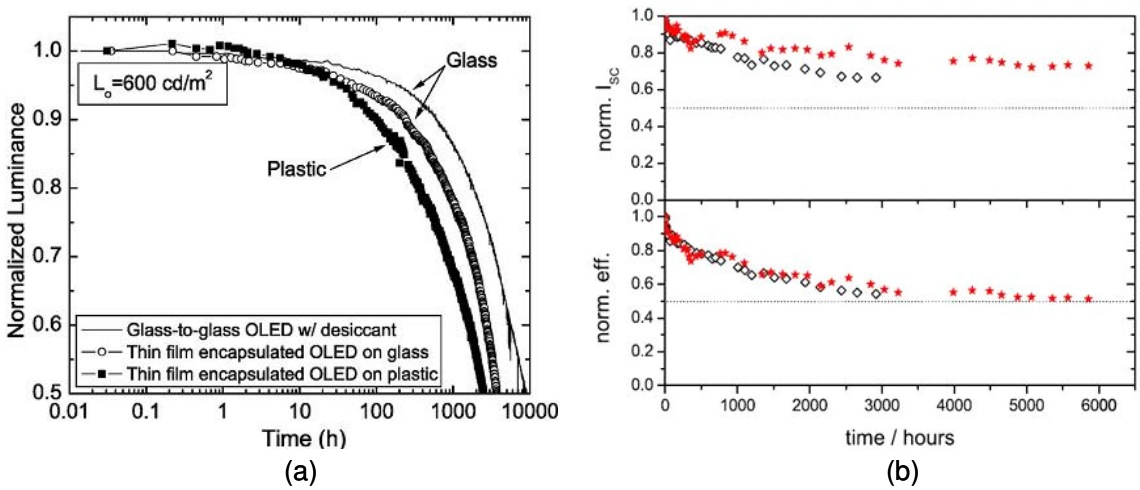

Figure 2.16 (a) Normalized luminance for PHOLED on glass packaged with glass lid and desiccant, thin film encapsulated on glass substrate, and thin film encapsulated on barrier coated plastic substrate. Taken from reference.[72] (b) Normalized I_{sc} and overall efficiency of encapsulated solar cells based on MDMO-PPV:PCBM blends (open diamonds) P3HT:PCBM blends (stars) versus storage time in ambient air. Taken from reference.[79]

Much of the encapsulation methodologies have focused on the development of OLED devices due to their stringent requirements and near term commercialization potential. However, one major technical difference which exists between encapsulating OLEDs and OPVs results from the environmental conditions in which they will be utilized. Due to their direct insolation with solar energy, the barrier layers developed for OPVs should maintain their performance under the exposure of UV irradiation, unless UV blockers are utilized. When OPVs are exposed to irradiation at AM 1.5G conditions, radiation combination of UV exposure and significant heating could result in the degradation of barrier films, especially those containing polymer interlayers. To date, few tests have reported the long term barrier performance of encapsulation or encapsulated devices which have been exposed to direct solar irradiation or controlled AM 1.5G environments. Hauch et al. tested their P3HT:PCMB based solar cells encapsulated with barrier films with a WVTR rate of 0.03 g/m/day measured at 38 °C and 100 % RH under AM 1.5G illumination and at 65 °C and ambient humidity (30-60 % RH).[78] While this study showed the encapsulated organic solar cells under the

described conditions lost ~ 15 % of their initial performance after 1200 h, there was no independent study about the degradation of the barrier performance when exposed to AM 1.5G. Hence, to provide reliable protection for organic devices which are used under insolation with solar energy, it is necessary to investigate the degradation of the barrier performance under the same conditions.

2.6 Mechanics of Thin-Film Encapsulation

In addition to the requirement of low permeation, encapsulation films should maintain their barrier performance during and after mechanical deformation. One of the unique characteristics of organic electronic devices is their ability to be utilized in flexible electronics. Inorganic layers used in the encapsulation provide the largest resistance to water vapor and oxygen, yet limit the mechanical flexibility of the encapsulation and, thus, the device lifetime. These brittle layers in the encapsulation can sustain a limited amount of strain, typically 1.2 - 2.0 % prior to facture.[19, 53, 79, 80] In general, fractures in the encapsulation layers cause rapid device failure due to the increased permeation rates of water vapor and oxygen through the cracks in the encapsulation. Failure of the films may take place through the formation of parallel cracks or debonding which can initiate from preexisting defects in poor quality films. Such cracks can yield pathways for rapid transport of oxygen and water vapor causing device failure. Overall, devices that require extremely low permeation rates, such as OLEDs and OPVs, may necessitate the use of inorganic layers for such low permeation since few alternatives exist.[19] Therefore, the response of thin films under mechanical deformation should be understood, and more mechanically robust encapsulation structures should be developed in order to commercialize flexible organic electronics.

While inorganic layers are necessary for ultra-high barrier performance, they introduce the additional risk of barrier failure under bending. For organic electronics to be flexible, the device as well as the encapsulation layer must be able to withstand

repeated flexural stresses and strains. It is also desirable for these films to maintain their barrier performance under both tensile and compressive stress and to have adequate adhesion to devices. While a number of investigations into the brittle failure of indium tin oxide (ITO) transparent electrodes have been performed,[81, 82] there have been relatively few studies on the mechanical behavior of encapsulation films.[79, 83] While the crack or failure of ITO electrodes can be detected by measuring electrical conductance,[84] the imaging of cracks in transparent thin film is a challenging task. In general, small damaged regions which can not be detected by visual inspection or even optical microscope efficiently in the brittle layer of the encapsulation can quickly accelerate device failure. Due to this reason, reported results about crack formation in transparent thin films under mechanical deformation are limited. While the images of cracks caused by tensile uniaxial [85, 86] or biaxial stress [87]obtained by AFM or SEM have been reported, such studies require a large amount of statistical work for reliable conclusions. To reduce the number of samples required for this analysis, oxygen plasma treatments suggested by Sobrinho et al.[34] for defect detection introduced in Section 2.3 was employed to image cracks caused by bending.[88] This method is based on the etching and undercutting of the polymer beneath the defects. After a certain exposure time to atomic oxygen, the cracks become visible even under an optical microscope as previously explained.[34] However, in-situ imaging of cracks to determine the crack on-set strain under mechanical deformation is still challenging and many approaches are under investigation. Similar to the oxygen plasma treatment method, cracks caused by mechanical deformation can be made visible by using a Ca layer. As previously explained, Ca is opaque and electrically conducting before oxidation and becomes optically transparent and electrically non-conducting. After encapsulation of Ca deposited on the transparent coated polymer substrate with barrier thin films which we study, cracks caused by mechanical deformation can be detected easily due to the change of optical transparency even under low resolution optical microscopy. Images in the

Figure 2.17 show Ca degradation due to the permeation of water vapor and oxygen through cracks which becomes more visible as time passed. Therefore, as we change the mechanical strain on the encapsulation layer by changing the bending radius of curvature, the formation of cracks can be found.

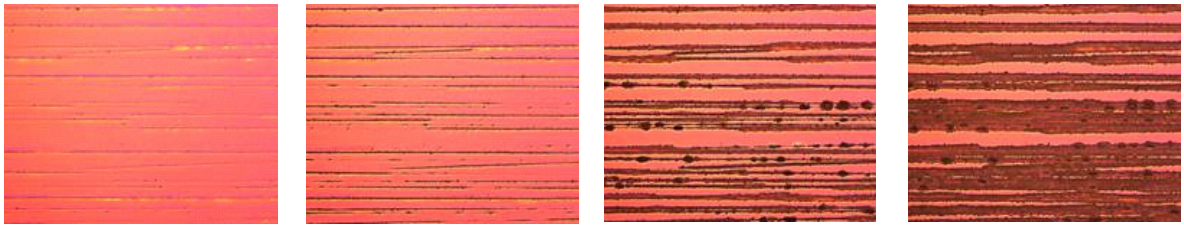

Figure 2.17 Optical microscope images show encapsulated Ca degradation after bending at certain radius of curvature after 1 min (a), 10 min (b), 30 min (c), and 1 h (d).

While most encapsulation films are tested under flexural deformation, they are typically tested in a 2 point bend configuration (collapsing radius). Here, the sample is simply flexed between two points as shown in Figure 2.18 (a).[89] While such experiments are easy to set up, the radius of curvature in the sample is not constant, resulting in a strain distribution throughout the film. Thus, care must be taken in trying to relate the failure of the films to strain due to the non-uniform radius of curvature. To circumvent this issue, a X-Y-θ bending system shown in Figure 2.18 (b) and (c) was developed to overcome the limitation of 2 point bending experimental setup.[84] More details about this bending experimental method compared to collapsing radius method have been discussed elsewhere.[84]

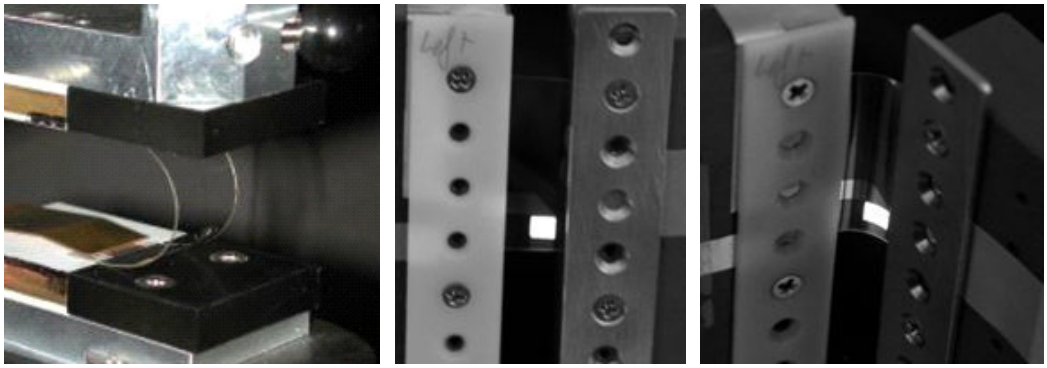

(a) (b) (c)

Figure 2.18 Picture showing a 2 point bending configuration (a) taken from reference.[91] Images (b) and (c) show a X-Y-θ bending system taken from reference.[86].

Grego et al. reported the onset of mechanical failure of 100 nm thick SiO_xN_y film on 130 μm thick PEN substrate by using the newly developed X-Y-θ bending system which enables well defined radius of curvature as illustrated in the Figure 2.19 (a).[88] Results in the Figure 2.19 (b) show cracks initiated from 7 mm radius (~ 0.9 % strain) of curvature bending and crack density increases as radius decreased. This experiment also demonstrated experimentally that a top-coating polymer can improve the mechanical ruggedness of an inorganic layer by passivating its mechanical flaws.[83, 84] Results indicate onset crack radius of SiO_xN_y film with epoxy top-coat is reduced from 7 mm to 5 mm. In addition, the onset crack strain of inorganic films as well as the failure of films caused by repeated bending stress should be considered for the actual application of flexible organic electronics. SiO_xN_y film with epoxy top-coat was bent with 6 mm radius of curvature which does not cause any cracking in this experiment. However, after repeated bending (n= 10, 100, and 1000) a low density of cracks was found although the crack density appeared to saturate. Therefore, the failure of barrier layers caused by single and multiple flexural events should be accounted for designing mechanically robust encapsulation.

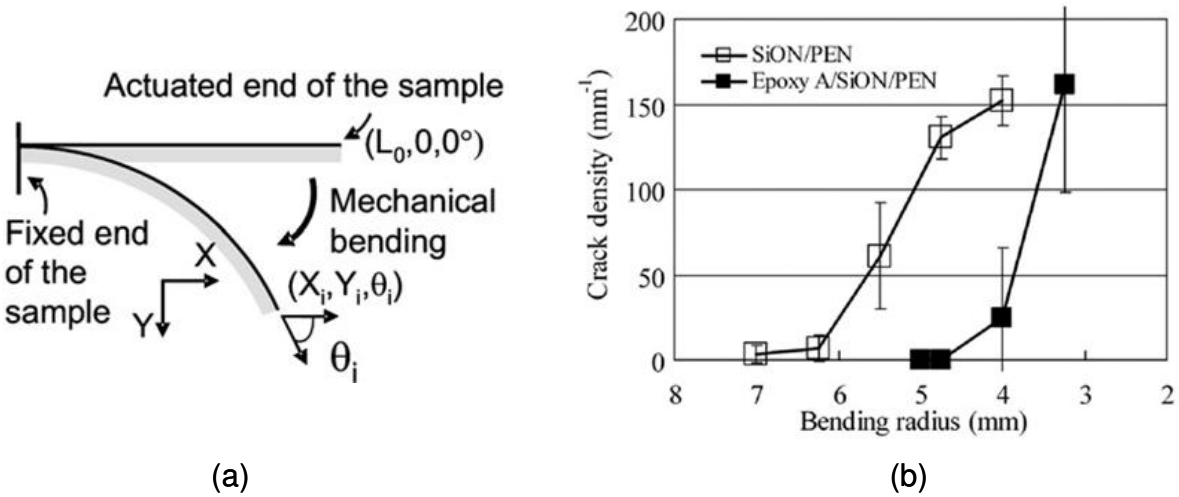

Figure 2.19 (a) Schematic of the mechanical bending test in the *X-Y-θ* apparatus. (b) Crack density as a function of decreasing bending radius for SiO_xN_y on PEN and same film with a polymer top-coat of epoxy. Taken from reference.[90]

In addition to understanding the mechanical response of encapsulation films, it may also be advantageous to find architectures which limit the amount of strain placed on barrier films, thereby increasing their flexibility. As stated earlier, most of the mechanical liability in encapsulation films arises from the limited strain to failure of inorganic layers. However, the strain placed on the inorganic layer is related to the radius of curvature during bending as it position relative to the neutral axis of the devices given by:

$$\varepsilon_z = \frac{z}{R} \tag{2.13}$$

In Equation (2.13), z is the distance from the neutral axis and R is the radius of curvature as illustrate in the Figure 2.20. Thus, the strain can be minimized by reducing z by moving the inorganic layers closer to the neutral axis. A more detailed expression for strain in the non-homogeneous structure was developed by Suo et al. and is given by Equation (2.14)

$$\varepsilon_{film} = \left(\frac{d_1 + d_2}{2R}\right)\frac{(\chi\eta^2 + 2\eta + 1)}{(1+\chi\eta)(1+\eta)} \tag{2.14}$$

Where $\chi = E_1/E_2$ and $\eta = d_1/E_2$. E_1 and E_2 and d_1 and d_2 are the modulus and thickness of film and substrate, respectively. In such systems, the neutral axis can be shifted according the modulus of materials. They reported that neutral axis is shifted towards the brittle film which can reduce the strain by as much as a factor of 5 for given R, d_f and d_s by using different modulus materials.[90] Park et. al. also, proved strain reduction numerically by inserting the compliant material between the substrate and the barrier layer.[91]

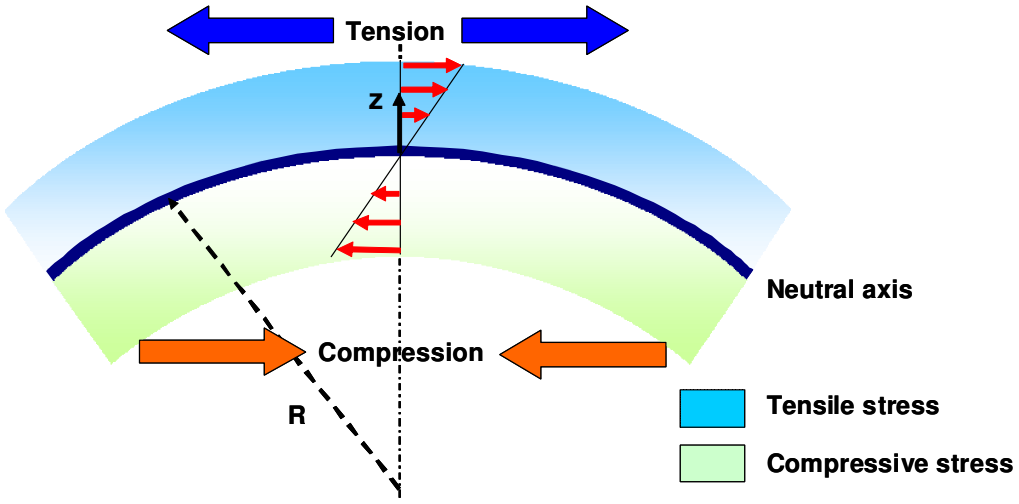

Figure 2.20 Schematic shows strain distribution through film when it is bent with bending radius of R. The region below the neutral axis has a compressive tensile stress, while that above neutral axis has tensile stress.

Furthermore, Sekitani et. al successfully showed that laminated organic FETs as illustrated in the Figure 2.21 (a) are functional at extremely small bending radii (less than 1 mm) as shown in the Figure 2.21(b).[92] They fabricated the device on a 13 μm thick polyimide film and covered by a 13 μm thick poly-chloro-para-xylylene encapsulation layer so the device can be embedded at a neutral surface. Such concepts can also be applied to the development of encapsulation structures to improve the mechanical performance under flexural deformation.

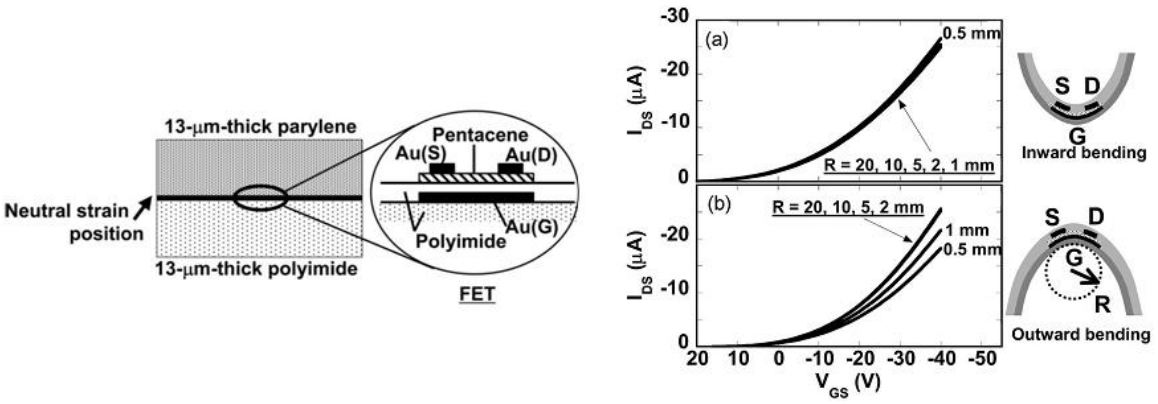

Figure 2.21 (a) Schematic shows the cross-sectional view of sandwiched organic transistor between plastic films and parylene passivation layer. (b) Transfer characteristics with bending radii of R=20, 10, 5, 2, 1, and 0.5 mm; which corresponding to (top) inward and (bottom) outward bending strains. Taken from reference.[94]

CHAPTER 3

EXPERIMENTAL METHODS

3.1 Introduction

The main goal of this chapter is to provide details of the experimental methods used in this dissertation work. It starts with various fabrication techniques for thin films including detailed process parameters. PECVD and parylene CVD were used for multilayer encapsulation structures and PECVD and ALD for single and hybrid structures. Detailed fabricated structures for each encapsulation layer are described in corresponding chapters. The barrier performance of thin-film encapsulation was characterized using Ca corrosion test and detailed test procedures are explained in this chapter. Mechanical responses of the barrier films were also characterized for application of flexible organic electronics. In the last section, test procedure for device performance of organic solar cell is explained.

3.2 Thin-Film Fabrication

Vacuum deposition techniques were used to create barrier films used in this study. Such techniques are well established for the formation of organic and inorganic films which are imperative to the development of ultrahigh barrier films. While a number of vacuum deposition methods can be utilized for creating inorganic layers, this work concentrates on the use of plasma enhanced chemical vapor deposition, chemical vapor deposition, and atomic layer deposition. Such techniques give a wide range of materials and tenability in the deposition of coatings. Detailed aspects of these techniques are discussed in the following sections.

3.2.1 PECVD

PECVD is one of the techniques which allows for industrial-scale deposition of good quality insulating films such as silicon oxide and silicon nitride with good adhesion.[93] One of the main advantages of PECVD is the availability of low temperature deposition compared to other chemical vapor deposition (CVD) methods, such as thermally driven CVD. While temperatures of only 250 °C or lower are sufficient for depositing films by PECVD, deposition temperatures of 700 °C to 900 °C are required to deposit similar films by thermal CVD. This lower temperature capability is very attractive for application to the encapsulation of both organic electronics and flexible electronics because the intrinsic properties of organic materials and polymer substrates for flexible electronics limit the maximum processing temperature (preferably below 100 °C, maximum limit ~ 130 °C).[94]

A Plasma-Therm PECVD was used in this study for the fabrication of both SiO_x and SiN_x and equipment is shown in Figure 3.1 (a). Precursors used were SiH_4, N_2, and NH_3 for SiN_x depositions and SiH_4, N_2O, and NH_3 for SiO_x. These precursors were fed into the vacuum chamber at a user-defined mass flow rate. The precursors were reacted between two parallel plates in a radio frequency (RF) induced plasma to deposit the films. Depositions in our experiments were carried out at 110 °C for compatibility with organic electronic devices. PECVD-fabricated films were used as an inorganic layer in either multilayer or hybrid-layer encapsulation structures and as a buffer layer in both structures for the entire coverage of Ca sensors, which will be explained in section 3.3.1. Table 3.1 lists the detailed processing conditions for the deposition of the SiO_x and SiN_x films. The deposition rates were 32 nm/min and 10 nm/min for SiO_x and SiN_x, respectively. Both of the inorganic films were deposited with a thickness of 100 nm as previous studies have shown that this is the critical thickness for both SiO_x and SiN_x barrier layers.[28, 40] No further improvement in barrier performance is observed for films thicker than the critical thickness.

Table 3.1 Summary of SiO_x and SiN_x film deposition conditions.

Parameter	Unit	Film	
		SiO_x	SiN_x
RF power	W	30	30
Chamber temp.	°C	110	110
Chamber press.	mTorr	900	900
SiH_4 flow rate	Sccm	400	200
N_2O flow rate	Sccm	300	NA
He flow rate	Sccm	NA	560
N_2 flow rate	Sccm	NA	720
NH_3 flow rate	Sccm	NA	14

(a) (b) (c)

Figure 3.1 Thin-film fabrication equipments used in this study: (a) Plasma-Therm PECVD for SiO_x and SiN_x films, (b) Lab Coater PDS2 for parylene films, (b) Savanah 100 for Al_2O_3 film.

3.2.2 Parylene CVD

Parylene was chosen as an organic layer in multilayer structures and as a top protecting layer in both single and hybrid layer structures due to its low modulus and relatively hydrophobic nature. Also, it was reported that parylene keeps water from condensing on the Al_2O_3 films[94] which is known to corrode Al_2O_3. Parylene is a relatively flexible polymer (modulus ~ 4 GPa), which helps with stress relaxation during the fabrication of inorganic layers such as SiO_x and SiN_x by PECVD. Parylene is generally produced by vapor-phase deposition without any additional curing process. For

CVD, parylene dimmer is vaporized to a monomer around 650 °C and condensed below 10^{-5} Torr at room temperature to result in a conformal coating on the all surfaces in the chamber. The deposition at room temperature eliminates all risk of thermal damage of samples, which is favorable for the encapsulation of organic electronic devices as previously described.

In our experiment, a Lab Coater PDS2 shown in Figure 3.1 (b) was used for the parylene deposition. Parylene C dimmer was loaded in the vacuum chamber and converted to a monomer vapor at around 650 °C. Condensation of the vapor on the sample at room temperature resulted in spontaneous polymerization and conformal deposition on the surfaces of all objects in the chamber. Parylene C dimmer was chosen because it has a low permeability for gas and water vapor compared to other parylene dimmers such as parylene N and parylene D. Parylene thickness was controlled by the amount of parylene dimmer loaded in the system. The parylene thickness was measured to be 1 μm in our study with a KLA-Tencor P-15 profilometer. In general, it takes 30 min to deposit this thickness excluding vacuum pump down and furnace heating processes.

3.2.3 ALD

ALD is well-known for its thin, highly uniform, conformal and pinhole-free films with featureless microstructures at relatively low temperature. It was already reported that ALD deposited films show excellent dielectric properties.[95] This is consistent with pinhole-free films, which are required for high barrier performance encapsulation.[95] Insulating materials such as Al_2O_3, SiO_x, and SiN_x as well as transition metals including copper, cobalt, and iron can be deposited by ALD.[96] Al_2O_3 was chosen for fabrication by ALD because it can be deposited with a variety of precursors with high reliability and relatively short cycle times.[97] ALD is a CVD method and is based on sequential pulses of two different chemical precursors. ALD is a layer by layer buildup of materials

beginning with chemisorption of molecular precursors. These precursor gases are introduced into the deposition chamber one by one with an inert carrier gas such as nitrogen to form monolayer coverage on the surface of the sample. Excess precursor is then removed by purging with an inert gas followed by the introduction of the next precursor. These processes are repeated and can produce high quality films with featureless microstructure and conformal coatings.

In our experiment, a Savanah 100 (Cambridge Nanotech) shown in Figure 3.1 (c) was used to deposit Al_2O_3 films. The deposition was performed at 110 °C, which was reported to be compatible with organic devices, using sequential, shelf-limiting exposures to trimethylaluminum (TMA) and water vapor (H_2O). Our ALD cycle for Al_2O_3 consisted of a 0.015 s TMA exposure, a 5 s nitrogen purge, a 0.015 s water exposure, and another 5 s nitrogen purge. One cycle above produces an approximately 0.1-nm-thick Al_2O_3 film, so the thickness of the deposited film is controlled by the number of cycles. For example, 500 cycles are needed to deposit 50-nm-thick Al_2O_3, which corresponds to 1 hr 25 min. Process time depends on the chamber temperature because the precursors take longer to react at lower temperatures.

3.3 Barrier Performance Investigation

3.3.1 Ca Corrosion Test

For the effective WVTR measurements, Ca corrosion tests were performed, and the basic concept of this method was described in Chapter 2. In our experiment, we used Ca corrosion tests with electrical analysis (measurement of electrical conductance change) instead of optical analysis (measurement of optical transmittance change) because the electrical analysis test can be performed in a highly parallel and automated manner. By using an Agilent data acquisition switch unit, we can automatically monitor the resistance changes of 20 samples at the same time.

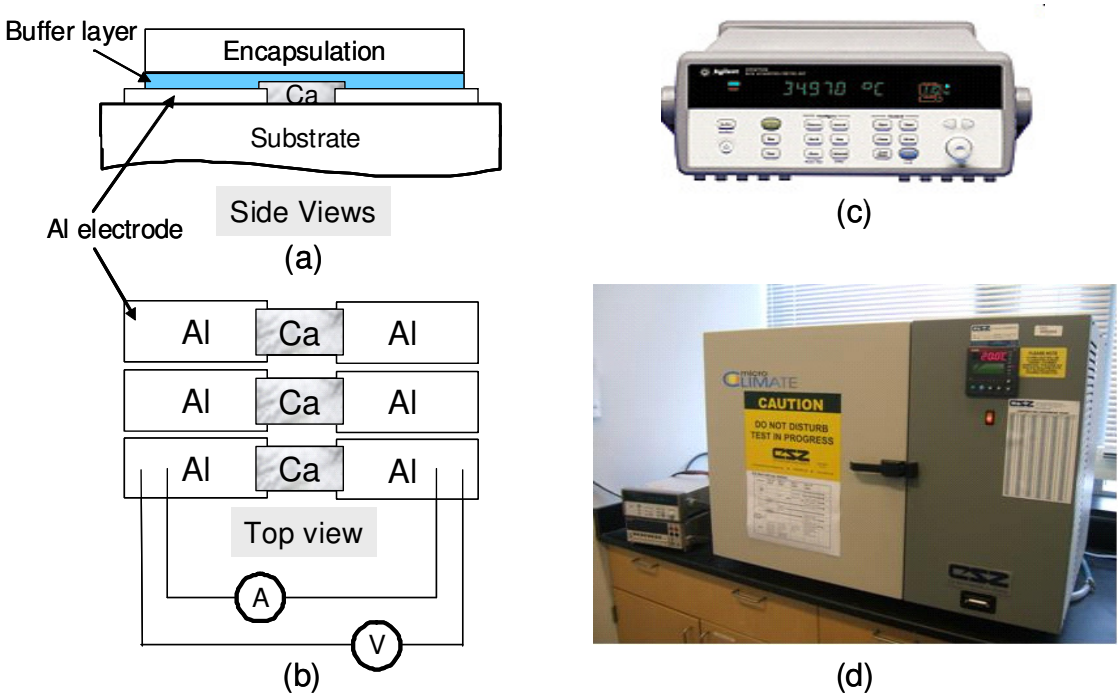

Figure 3.2 (a) Side view of a Ca test cell and encapsulation layer on both Ca and the glass substrate. (b) Top view of three Ca test cells with 310 nm-thick Ca and 100 nm-thick Al electric contacts. (c) Electrical conductance was measured by data acquisition system. (Agilent 34970A) (d) Ca corrosion tests were performed in the shown controlled humidity chamber (Cincinnati subzero micro-climate system) at 20 °C and 50 % RH.

In this experiment, three Ca sensors with an area of 4.5×7 mm^2 and Al electrical interconnects were used for resistance measurements as shown in Figure 3.2 (a) and (b). The thickness of Ca sensor and Al electrode was 310 nm and 100 nm, respectively. Before the fabrication of thin-film encapsulation structures, a 400 nm thick SiO_x buffer layer was deposited on top of Ca sensor as shown in Figure 3.2 (a) to cover Ca sensor entirely. This buffer layer covers entire Ca sensor to prevent side permeation. To reduce the effects of contact resistance during measurements, four wire measurements were carried out with an Agilent 34970A shown in Figure 3.2 (c). The Ca corrosion tests were performed in a controlled humidity chamber (Cincinnati Subzero Micro-Climate System, Figure 3.2 (d) at 20 °C and 50 % RH.

It should be noted that substrates should be cleaned in a clean room environment before the deposition of Ca sensors and Al electrode. Particle contaminations on the Ca

sensor and in the encapsulation layers causes defects leading to localized oxidation giving erroneous values of effective WVTR. The cleaning process employed in this study consisted of five cleaning steps: acetone – methanol – Isopropyl alcohol (IPA) – deionized (DI) water – nitrogen blowing. After cleaning, the substrates were transferred to deposition system. To create the Ca test structure, aluminum (100 nm) and calcium (310 nm) layers were deposited through shadow masks on either glass or coated PET substrates using a vacuum deposition system (Spectros, Kurt J. Lesker) connected to a nitrogen-filled glove box. Deposition rate and thickness were monitored using a calibrated quartz crystal microbalance near the substrate. Al was deposited at a rate of 2 Å/s and Ca at 2 - 3 Å/s with a base pressure of ~ 8×10^{-8} Torr. Both depositions were made without breaking vacuum. After deposition, the Ca sample was transferred in container sealed under nitrogen to a Plasma-Therm PECVD system. The Plasma-Therm system was used to deposit a 400 nm SiO_x layer (buffer layer), which is thicker than the thickness of the Ca sensor to remove the side permeation effects by completely covering the Ca. After depositing the 400 nm SiO_x layer, either multilayer or hybrid-layer encapsulation was deposited. Reported effective WVTR was averaged over data from three Ca sensors.

In order to measure the effective WVTR accurately using electrical resistance monitoring during the Ca corrosion test, it is assumed that the oxidation takes place uniformly through the barrier film. To check for uniform permeation through the coatings, a visual inspection of the Ca can be performed to observe whether or not the oxidation occurs in localized regions. As explained in the previous chapter, a sample with localized oxidation of the Ca sensor would give erroneous values of effective WVTR. Therefore, those samples were avoided when calculating the effective WVTR.

3.3.2 Uncertainty and Error Propagation

In the barrier performance measurement, reported effective WVTR values were calculated based on Equation (2.12). In this equation, the measured values are the conductance change (d*G*/dt) denoted by *E* and dimension of Ca sensor (*l* and *w*) denoted by *D*. The area ratio of Ca to window was assumed to be unity due to geometry of our sample as explained in Section 2.4 and other values were taken from references. Hence, the uncertainty of reported WVTR can be found using derivative method.[98]

$$\frac{\Delta WVTR}{WVTR} = D\frac{\Delta E}{E} + E\frac{\Delta D}{D} \tag{3.1}$$

While other values may have uncertainty, these should be very small compared to the uncertainties of *E* and *D*. Conductance (G) was measured by Agilent 34970A which has uncertainty of 0.8 % calculated based on 50 measurements with 4-wire measurement. The Ca sensors were fabricated using thermal evaporation through a shadow mask of fixed dimensions. As such, those uncertainties from both *E* and *D* are expected negligible compared to uncertainties from statistical variations among three samples encapsulated with same structure. Hence, statistical analysis was applied to report the uncertainties in our measurement. Average values and standard deviations were calculated using equation (3.2) and (3.3), respectively.[99]

$$< x > = \frac{\sum_{i=1}^{N} x_i}{N} \tag{3.2}$$

$$\sigma = \sqrt{\frac{\sum_{i=1}^{N} (x_i - < x >)^2}{N-1}} \tag{3.3}$$

Where, <*x*> and *N* are average value over samples and the total number of samples for each calculation, respectively, and σ is the standard deviation. All effective WVTRs and uncertainties were based on three samples and reported using equation (3.2) and (3.3) in each chapter. Other reported values in this study such as device performance parameters of organic solar cells were also averaged over three samples. Hence, for same reason,

reported uncertainties were calculated using equation (3.3) and reported with averaged values.

3.4 Mechanical Response Investigation

3.4.1 Nanoindentation

In order to investigate the mechanical properties of thin films, nanoindentation tests were carried out on a Nano Indenter XP. For more accurate measurements, we used the continuous stiffness method (CSM) in this study. The elastic modulus and hardness can be calculated from the elastic contact stiffness (*s*). In the classical method, the elastic contact stiffness is determined from the slope of the load-displacement data that is measured during unloading. However, one can get only one elastic contact stiffness at the maximum penetration depth. CSM allows one to get continuous measurements of elastic contact stiffness during loading. The experimental set-up for nanoindentation is shown in the Figure 3.3 (a), and the simple harmonic oscillator used to model dynamic response of a Nano Indenter head in contact with a test sample is in the Figure 3.3 (b).

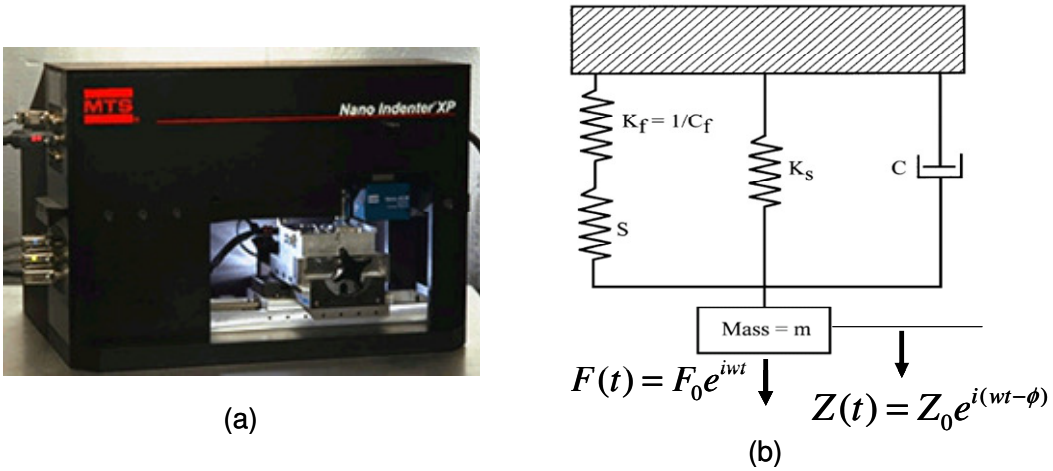

Figure 3.3 (a) Nanoindentation test was performed using Nanoindenter XP (http://www.mse.gatech.edu/Research/Equipment_Facilities/CNC/NanoidenterXP/nanoidenterxp.htm). (b) Schematic illustrates simple harmonic oscillator. Taken from reference. [102]

In CSM, the force balance of the simple harmonic oscillator in Figure 3.3 (b) yields the second ordinary differential equation:

$$mz''+Cz'+Kz=F(t) \tag{3.4}$$

Where, $K=(s^{-1}+k_f^{-1})+K_s$, m and C are mass and damping coefficient in harmonic oscillator shown in Figure 3.3 (b). If a known driving force of

$$F(t)=F_0e^{iwt} \tag{3.5}$$

is applied, then the displacement response of the indenter will be

$$Z(t)=Z_0e^{i(wt-\phi)} \tag{3.6}$$

Substituting equations (3.6) and (3.5) into (3.4) leads to relationships between the contact stiffness and the reduced elastic modulus, and a detailed derivation can be found in the reference.[100] The contact stiffness can be calculated by

$$s=\beta\frac{2}{\sqrt{\pi}}E_{eff}\sqrt{A} \tag{3.7}$$

where β is a constant that depends on the indenter geometry (β =1.034 for a Berkovich indenter [100]) and E_{eff} is the effective elastic modulus, which accounts for the fact that the deformation during indentation occurs in both the sample and indenter. The elastic modulus of the sample can be extracted by

$$\frac{1}{E_{eff}}=\frac{1-\upsilon^2}{E}+\frac{1-\upsilon_i^2}{E_i} \tag{3.8}$$

where E_i and v_i are the elastic modulus and Poisson's ratio of the indenter, respectively, and E and v are those of the sample. For diamond, E_i is 1141GPa and v_i is 0.07 [100]. Therefore, the elastic modulus of the films deposited on the substrate can be calculated. If the films are very thin, the elastic modulus from the experiment can be affected by the substrate. As a rule of thumb, the elastic modulus and the hardness are independent of

the substrate up to some maximum indentation depth in the film. Typically, it is 10 % of the total film thickness for substrates which appears rigid.[101] In this study, we used glass substrates and report the elastic modulus and the hardness measured by nanoindentation experiments with indentation depths no greater than 10 % of the total film thickness.

3.4.2 Wafer Curvature Method

One of the widely used methods for the measurement of residual stress is the wafer curvature method using the Stoney equation.[102] It assumes that the film is very thin compared to the substrate and that the deformations are very small.[103] Residual stress of the film σ_f is then given by

$$\sigma_f = -\frac{1}{6}\left(\frac{1}{R_{post}} - \frac{1}{R_{pre}}\right)\frac{E_s}{(1-\upsilon)}\frac{t_s^2}{t_f} \tag{3.9}$$

where E_s is Young's modulus of the substrate, R_{post} and R_{pre} are the radii of curvature before and after film deposition, and t_s and t_f are the thicknesses of the substrate and the film, respectively. The key parameter in this equation is the change of substrate's radius of curvature. Both R_{post} and R_{pre} were measured using a KLA Tenkor p-15 contact mode profilometer. If the height of the substrate (y) is scanned as a continuous function of distance along the substrate (x), then the radius of curvature at any point may be calculated by

$$R(x) = \frac{(1+y'^2)^{\frac{3}{2}}}{y''} \tag{3.10}$$

where $y' = dy/dx$, and $y'' = d^2y/dx^2$. Each scan is fitted to a 5th order polynomial that gives the least sum of squares, and the polynomial is differentiated to get $y'(x)$ and $y''(x)$. These differentiated functions are inserted into Equation (3.10) to calculate the radius of curvature both before and after deposition. Finally, these two radii of curvature are

substituted into equation (3.9) to calculate residual stress. Negative values from equation (3.9) indicate compressive stress, which results in a convex surface, and positive values correspond to tensile stress (concave surface).

3.5 Device Performance Characterization of Organic Solar Cell

To study the shelf-lifetime of encapsulated organic solar cells, pentacene/C_{60}-based organic solar cells were used. The device geometry consisted of ITO/pentacene (45 nm)/C_{60} (50 nm)/BCP (8 nm)/Al, and the fabrication and testing procedures were identical to those produced by Prof. Kippelen's group at Georgia Tech.[104] As explained in the literature review, organic electronic devices can be damaged by high temperature or plasma during the encapsulation process. Therefore, the main device performance parameters such as power conversion efficiency η, open-circuit voltage V_{OC}, short-circuit current density J_{SC}, and fill–factor FF measured before and after encapsulation were compared to verify the compatibility of the encapsulation process with the organic solar cells. These parameters were extracted from the current density-voltage curves measured under illumination as shown in the Figure 3.4. This graph is a typical current density-voltage curve for the ITO/pentacene (45 nm)/C_{60} (50 nm)/BCP (8 nm)/Al organic solar cells used in this study. The current density is the current divided by device area. The J_{SC} (current density for V=0), V_{OC} (voltage for I=0), and voltage (V_{mpp}) and current density (J_{mpp}) at the maximum power point (P_{max}) are also shown in the figure. FF is defined as the ratio of the actual maximum generated power (V_{mpp} x J_{mpp}) to the theoretical maximum power ($V_{OC} \times I_{SC}$) and is given by

$$FF = \frac{V_{mpp} \cdot J_{mpp}}{V_{OC} \cdot J_{SC}} \tag{3.11}$$

The power conversion efficiency of a solar cell is expressed as follows

$$\eta = \frac{V_{OC} \cdot J_{SC} \cdot FF}{P_{in}} \tag{3.12}$$

where P_{in} is the incident light power. By monitoring those parameters, one can investigate how the encapsulation process affects the performance of organic solar cells.

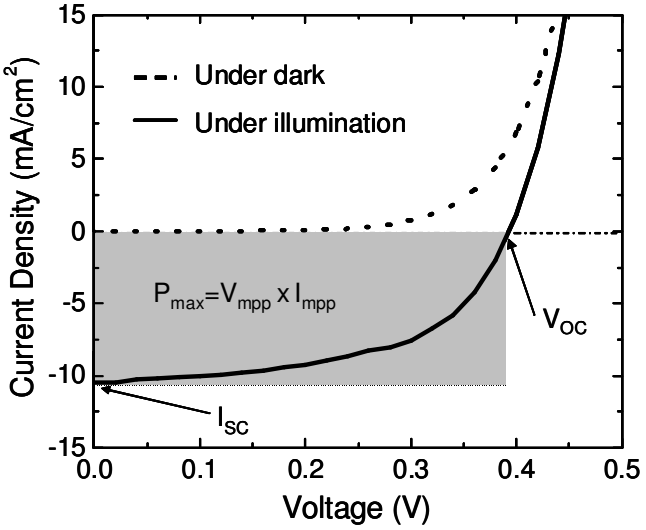

Figure 3.4 Typical current density-voltage curve for a glass/ITO/pentacene (45 nm)/C_{60} (50 nm)/BCP (8 nm)/Al organic solar cell.

After the investigation of the compatibility of the encapsulation process with pentacene/C_{60}-based organic solar cells, encapsulated devices were stored in an environmental chamber (20 °C and 50 % RH). Periodically, encapsulated devices were removed from the chamber, tested in the dark and under illumination in the laboratory environment, and returned to the chamber. The main performance parameters such as η, V_{OC}, J_{SC}, and FF were compared to those of un-encapsulated devices for a study of shelf-lifetime. Degradation and shelf-lifetime of the encapsulated organic solar cells were evaluated from the evolution of those parameters versus time. In this study, shelf-lifetime was defined by a drop in power conversion efficiency of 50 % from its initial value.[105]

CHAPTER 4

MULTILAYER ENCAPSULATION

4.1 Overview

In this chapter, multilayer encapsulation structures based on alternating organic and inorganic layers are introduced. The motivation to use multiple layers instead of a single layer was simply to enhance the overall barrier performance. Many defects exist in most deposited thin films due to the intrinsic properties of vacuum deposition as discussed in Chapter 2, and these defects allow for the permeation of water vapor and oxygen, resulting in low barrier performance. By applying an organic layer between inorganic layers, the defects in the inorganic layer are interrupted and do not channel continuously through the encapsulation structure. The permeation path of water vapor and oxygen become tortuous, which results in improvement of the barrier performance. As such, it is the goal of this chapter to achieve a high performance barrier layer by applying alternating organic and inorganic films and to investigate how the number of layers impact on the overall barrier performance. For a comprehensive study about the barrier layers, the impact of individual constituent films on the barrier performance and water vapor permeation mechanism through these were investigated in this chapter.

In order to investigate the improvement in barrier performance using multilayer films experimentally, SiO_x and SiN_x deposited by PECVD are used as inorganic layers, and parylene is used as the organic layer in this study. PECVD-deposited SiO_x and SiN_x were used to investigate how different quality of single inorganic layers affects the overall barrier performance in the multilayer structure. Barrier performance was examined in terms of the effective WVTR using Ca corrosion tests, and the results are presented in the following section of this chapter. By applying a different number of

dyads (one pair of organic and inorganic layers), one can find the correlation between the number of barrier layers and the effective WVTR. In this study, SiO_x/parylene structures with one to three dyads and SiN_x/parylene structures with one to fives dyads were investigated in terms of the effective WVTR.

Additionally, the impact of the process temperature of the PECVD on the barrier performance was investigated. Of all of the parameters of the PECVD process, only the impact of process temperature was investigated because processing at lower temperatures is more favorable for integration with organic electronic devices. Furthermore, a study of physical changes in the parylene organic layer during the multilayer encapsulation process was performed. Previous reports have shown that the surface roughness and free volume of parylene can be reduced when annealed near its glass transition temperature of 109 ºC. Thus, the impact of parylene annealing on the barrier performance was investigated in both SiO_x/parylene and SiN_x/parylene multilayer structures.

In the last section of this chapter, the dominant permeation path for water vapor in the inorganic layers was addressed based upon the experimental results. The permeation of water vapor and oxygen through thermoplastic polymers has been known and well-exploited, while little is known about the permeation of water vapor and oxygen through inorganic thin films. Therefore, inspection using optical microscopy after reactive ion etching (RIE) and surface characterization using AFM were employed in order to indentify the defects on the surface in the different inorganic layers which can be a permeation path.

4.2 Barrier Performance

In order to investigate the barrier performance of multilayer encapsulation structures, Ca samples were prepared including an interlayer as shown in the Figure 5.1 (a). The buffer layer between the Ca sensor and the first inorganic layer in the multilayer structure was used to prevent side permeation as seen in Figure 3.2 (a) because the

thickness of the first inorganic layer was much thinner than that of the Ca sensor. In this study, 400-nm-thick SiO_x fabricated by PECVD, which was thicker than the Ca sensor, was used as the interlayer to completely cover the Ca sensor as shown in the Figure 4. 1 (a). Then, alternating organic and inorganic layers were fabricated on top of the interlayer to form a multilayer structure. In this study, dyad means the structure consists of one organic layer and one inorganic layer. The cross-sections of multilayer structures are shown in the Figure 4.1 (b) and (c) and their FIB images were shown in (c) and (e).

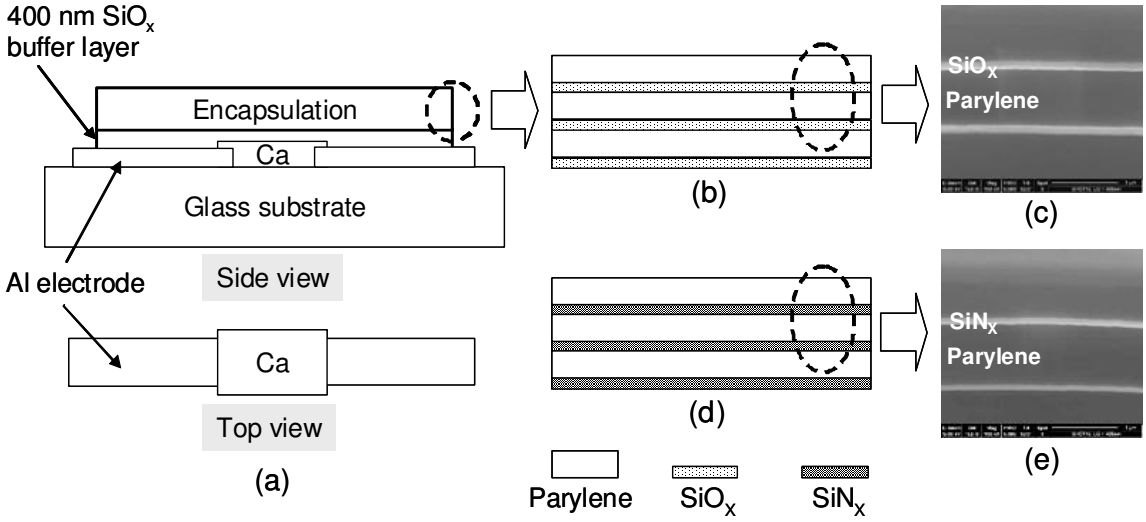

Figure 4.1 (a) Side and top views of a Ca test cell with a 310 nm-thick Ca sensor, 100 nm-thick Al electric contact, 400 nm-thick SiO_x buffer layer, and multilayer encapsulation. (b, d) and (c, e) are schematics and cross-section views by Focused ion beam of multilayer films, courtesy of Sarah Wagner of the Air Force Research Laboratories, consisting of 3 dyads of SiO_x/parylene and SiN_x/parylene, respectively. The dark region is parylene, and the relatively bright lines are either SiO_x or SiN_x layers.

After the fabrication of the multilayer film, encapsulated Ca sensors were stored in a controlled environmental chamber. Conductance of the Ca sensor was monitored automatically by a data acquisition system. The effective WVTR was calculated based upon the theory introduced in Chapters 2. The results of the effective WVTR measurements for SiO_x/parylene and SiN_x/parylene structure as a function of the number of dyads are shown in the Figure 4.2. The data in the Figure 4.2 show a clear trend of improving barrier performance with an increasing number of dyads. For SiO_x/parylene,

the effective WVTR for 1 dyad was found to be on the order of $3.1 \pm 0.7 \times 10^{-2}$ g/m^2/day at 20 °C and 50 % R.H. Additional dyads resulted in a large decrease in the effective WVTR for each dyad added, reaching a level of $6.6 \pm 3.0 \times 10^{-4}$ g/m/day with 3 dyads of SiO_x/parylene. A similar trend of improvement in the barrier performance with more dyads was also seen for SiN_x/parylene structures. However, compared to SiO_x/parylene, the effective WVTR was lower for 1 dyad of SiN_x/parylene with values of $5.8 \pm 2.1 \times 10^{-3}$ g/m/day. With 3 dyads, the barrier performance of the SiN_x/parylene structure was still better than that of SiO_x/parylene films, yielding values of $1.8 \pm 0.6 \times 10^{-4}$ g/m^2/day. These results are in agreement with previous reports that SiN_x has better barrier performance compared to SiO_x.[60, 61] The difference in the barrier performance arising from the choice of SiO_x or SiN_x will be further discussed in the next section of this chapter. Based upon the results, the quality of the single inorganic layer was found to be critical to the overall barrier performance of multilayer encapsulation structures.

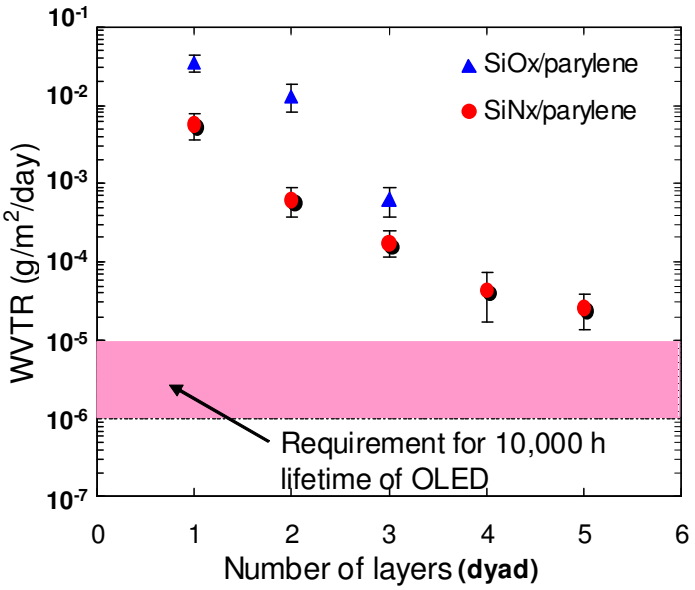

Figure 4.2 Effective WVTR as a function of the number of dyads for SiO_x/parylene and SiN_x/parylene. Clear trends between the number of encapsulation layers and the barrier performance are observed.

Further investigations of multilayer structures with four and five dyads were conducted using SiN_x/parylene instead of SiO_x/parylene because SiN_x/parylene demonstrate better barrier performance compared to SiO_x/parylene. With five dyads of SiN_x/parylene, an effective WVTR value of $2.6 \pm 1.2 \times 10^{-5}$ g/m^2/day was obtained, which is very close to the requirement for the encapsulation of OLEDs. However, the impact of additional dyads diminishes beyond 4 dyads of SiN_x/parylene. Based upon the trend from this investigation, there will not be significant improvement in the barrier performance with more than five dyads in the encapsulation structure. Therefore, in order to improve the barrier performance in the multilayer structure, there should be a additional improvements in either the inorganic layer or organic layer itself instead of an increase in the number of dyads. This will be discussed in details and verified by modeling in Chapter 5.

4.3 Impact of Processing on Barrier Performance

4.3.1 Impact of Processing Temperature

Investigations of individual films were performed in pursuit of improvement in barrier performance as well as to better understand the permeation mechanism of water vapor. First, the effect of process temperature during the PECVD process on the barrier performance was examined. In addition to the 110 °C already discussed, additional deposition temperatures of 50 °C and 170 °C were selected for PECVD. The process temperature of 110 °C, which is the standard deposition temperature in our study, was initially chosen for compatibility with organic electronic devices, while even lower temperatures may remove additional risk from higher temperatures. Hence, a substrate temperature of 50 °C was investigated to explore how lower temperature affects the overall barrier performance in the multilayer structure. On the other hand, substrate temperature was also increased from 110 °C to 170 °C to better understand barrier

performance even though the process may be less compatible with devices. Recently, polymer substrates that are resistant to higher temperatures, like polyethersulfone (PES), have attracted more attention due to their compatibility with both flexible and higher temperature applications. PES can withstand up to 180 °C without any thermal damage, which is higher than the more generally used PET can withstand (120 °C),[93] so the substrate temperature was limited up to 170 °C in this study.

Table 4.1 Impact of deposition temperature on effective WVTR of annealed SiO_x/ parylene multilayers (samples annealed as described in section 4.3.2).

Deposition temp. (°C)	Deposition rate (nm/min)	RMS roughness over 1 × 1 μm (nm)	Size of grain-like features (nm)	Effective WVTR ($g/m^2/day$)
50	37	4.0	~30	$8 \pm 2.0 \times 10^{-5}$
110	30	3.7	~30	$7 \pm 3.1 \times 10^{-5}$
170	50	3.4	~30	$6 \pm 2.5 \times 10^{-5}$

The influence of the process temperature on the deposition rate, surface roughness, grain feature size, and effective WVTR of 3 dyads of SiO_x/parylene are summarized in the Table 4.1. When the substrate temperature was increased from 50 °C to 170 °C, the deposition rate increased and roughness decreased. While higher temperatures induce an increase in the diffusion rate of the reactive species adsorbed on the surface resulting in an increase in the deposition rate, higher temperatures also enable more horizontal surface reactions to take place without simply vertically stacking. Consequently, more horizontal surface reaction can result in a smoother surface. In order to investigate the surface morphology in a systematic fashion, grain size was calculated by using the height-height correlation method[106] and results are summarized in Table 4.1. The corresponding AFM phase images of films deposited at different temperatures in Figure 4.3 also show negligible differences between the samples which were fabricated at different temperatures. Compared to AFM height images, phase images can clearly show the grain structure because the phase change is more sensitive to grain boundaries. While

SiO_x films fabricated at 110 °C and 170 °C show increased barrier performance compared to the films fabricated at 50 °C, the difference is insignificant and within the experimental standard deviation. These results are in agreement with previous reports that have shown that the permeability of silicon oxide films on polymer substrates is independent of the substrate temperature during the PECVD process.[93, 107] Therefore, it is favorable to decrease the substrate temperature during the PECVD process to minimize the thermal damage to the organic layers and polymer substrate during the integration with organic electronic devices.

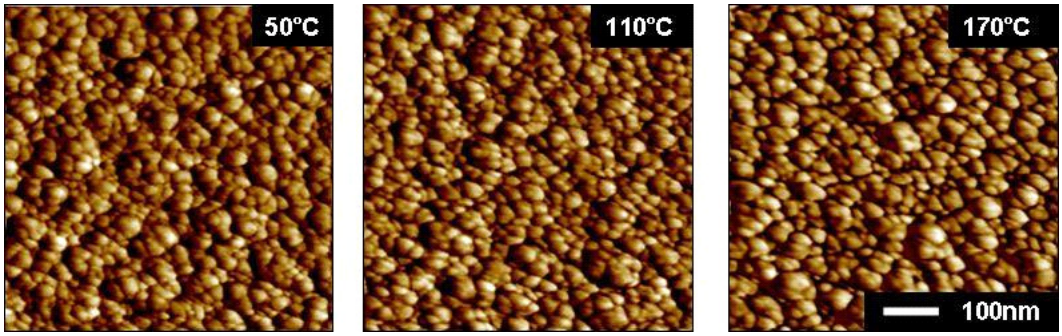

Figure 4.3 AFM phase images of SiO_x layers deposited at 50 ºC (a), 110 ºC (b), and 170 ºC (c), respectively. Images show negligible differences in the structure of the films.

4.3.2 Impact of Thermal Annealing of Parylene

Next, changes in the physical properties of parylene organic layers by annealing were investigated in order to study how annealing parylene affects the overall barrier performance in the multilayer encapsulation structure. Previous reports have shown that parylene can be crystallized and become smoother when annealed near its glass transition temperature (T_g) of 109 ºC.[108] When parylene is annealed around its T_g, the surface of parylene reflows, which results in a smoother surface.[108] In order to evaluate the annealing effect on the barrier performance, the effective WVTR of multilayer films consisting of 1 - 4 dyads of SiN_x/parylene with and without annealing were compared. Parylene was annealed at 110 °C at a pressure of 900 mTorr for 10 minutes in the

PECVD chamber prior to the PECVD process. This annealing step had a significant result on the effective WVTR, resulting in a decrease in the effective WVTR as listed in Table 4.2. In order to compare the effective WVTR before and after annealing, time periods for Ca conductance measurement were identical for each dyad. The improvement in the barrier performance from annealing increases as the number of SiN_x/parylene layer is increased. To verify these results, the same experiment was performed with 3 dyads of SiO_x/parylene. A similar trend was also seen in this structure. This result is very promising because it shows that it is possible to obtain effective WVTR values on the order of 10^{-6} g/m^2/day with only three dyads of SiN_x/parylene by adding an annealing step prior to the PECVD process in the same chamber. The negligible change in effective WVTR between three and four dyads suggests that the maximum benefit of the multilayer system can now be obtained with fewer layers of encapsulation.

Table 4.2 Effect of annealing parylene on effective WVTR.

Film	No. of dyads	Effective WVTR (g/m^2/day)		Decrease in effective WVTR (%)
		Without annealing	With annealing	
SiN_x/parylene	1	$6 \pm 2.1 \times 10^{-3}$	$3 \pm 1.0 \times 10^{-3}$	57
	2	$6 \pm 2.5 \times 10^{-4}$	$1 \pm 0.3 \times 10^{-4}$	82
	3	$6 \pm 0.6 \times 10^{-4}$	$7 \pm 5.0 \times 10^{-6}$	96
	4	$5 \pm 2.8 \times 10^{-5}$	$7 \pm 5.1 \times 10^{-6}$	85
SiO_x/parylene	3	$7 \pm 3.0 \times 10^{-4}$	$7 \pm 3.1 \times 10^{-5}$	89

In order to verify what the exact mechanism is that reduces the effective WVTR, change in crystallinity, permeation properties and surface morphology were investigated. Firstly, characterization of the films using Raman spectroscopy before and after annealing showed no changes in the intensity, linewidth, or location of Raman active peaks as shown in the Figure 4.4, suggesting that no significant structural difference between films before and after encapsulation at these temperatures and time scales. Raman spectroscopy was performed with a Renishaw InVia system utilizing a 488 nm

laser with a 3000 l/mm grating. To investigate this effect further, x-ray diffraction (XRD) experiments were carried out on the parylene films before and after annealing, and the results were found to agree with those from the Raman experiments. (Courtesy of Yeny Hudiono of Prof. Nair's group at Georgia Institute of Technology)

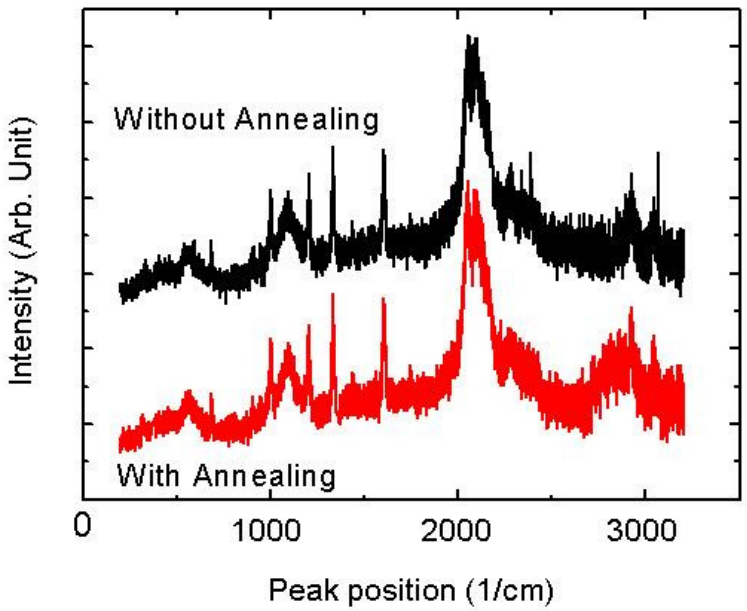

Figure 4.4 Raman spectroscopy scans show the dominant phonon vibrations in the parylene C film before and after annealing. The lack of change in the phonon vibrational frequency and linewidth suggests that there are no major structural differences between the films before and after annealing. (Courtesy of Thomas Beechem of Prof. Graham's group at Georgia Institute of Technology)

Secondly, permeation properties such as diffusion and solubility coefficient of parylene were measured by using a quartz crystal microbalance (QCM). Detailed experimental procedures for the QCM experiments are explained in Appendix A. Both permeation properties were measured before and after annealing and results are summarized in Table 4.3. It was found that both diffusion and solubility coefficients were not changed significantly after annealing. Additionally, if the permeation properties of parylene do not decrease by several orders of magnitude, it is not expected to impact on the barrier performance. This will be further explained in Chapter 5.

Lastly, surface morphology was scanned by using an AFM because it was expected that smoothing of the parylene layer during the annealing process could help in producing a subsequent inorganic layer with higher quality in the initial nucleation steps of the PECVD process. AFM scans of the parylene layer before and after annealing revealed a reduction in RMS roughness from 3.4 ± 0.4 nm to 3.0 ± 0.4 nm. These data clearly show that there is no statistically significant change in surface roughness and it cannot be considered a contributor to the reduction in apparent WVTR. It is also known that annealing the parylene can reduce the absorbed water vapor during the encapsulation process resulting in a decrease in permeation rate, especially in the transient region. Simulation results in Figure 4.5 by finite element method (FEM) show the impact of absorbed water during encapsulation on the WVTR in the transient region. After the transient region, there is no impact on steady state region. According to the amount of absorbed water which could not be characterized experimentally in this study, the WVTR in the transient region can be decreased significantly by the removal of residual absorbed water in the organic layer. Hence, reducing the absorbed water in the multilayer structure by annealing process is critical to decreasing the permeation rate in the transient region. This is very important for organic device encapsulation because high permeation rates in an early stage can damage the device performance which can't be recovered.

Table 4.3 Effect of annealing parylene on *D* and *S*. (Courtesy of Annapoorani Sundaramoothi of Prof. Henderson's group at Georgia Institute of Technology)

Diffusion coefficient, D (cm^2/s)		Solubility coefficient, S (g/cm^3atm)	
Before annealing	After annealing	Before annealing	After annealing
$8.0 \pm 1.0 \times 10^{-9}$	$1.2 \pm 4.0 \times 10^{-8}$	0.025 ± 0.004	0.027 ± 0.002

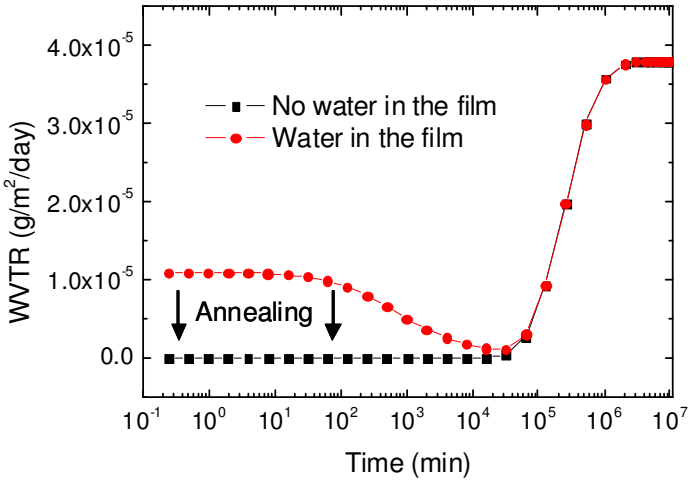

Figure 4.5 FEM simulations were carried out with two different initial conditions; no absorbed water and absorbed water condition in the film. Results show WVTR reduction in the early stage of permeation with no absorbed initial condition.

4.4 Discussion: Water Vapor Permeation through Inorganic Films

It is proposed that the permeation of water vapor and oxygen through inorganic films is comprised of three permeation paths in this study: unhindered permeation through micro-scale defects (>200 nm), unhindered permeation through nano-scale defects (~30 nm), and hindered permeation through the amorphous lattice (<1 nm). Most micro-scale defects result from particles on the surface of the substrate causing geometric shadowing during the deposition and from cracks due to high compressive stress.[34] Optical micrographs in Figures 4.5 (a) and (b) show some examples of micro-scale defects in both SiO_x (a) and SiN_x (b) films deposited by PECVD on a PET substrate. These defects are detrimental to the barrier performance and cause partial oxidation of Ca sensors as shown in the Figure 4.5 (c). For accurate calculation of the effective WVTR, these samples possessing micro-scale defects were excluded from our Ca corrosion tests. However, these defects were reduced after multiple-step cleaning processes (Acetone –

Methanol – IPA – DI water – Blowing compressed purified nitrogen) in a clean room environment.

For more accurate characterization of microscopic defects, a recently developed technique based on reactive ion etching (RIE) was employed. Theoretically, optical microscopy has a detection limit of 200 nm due to the wavelengths of visible light. Therefore the detection of defects within this size in a transparent film on a transparent substrate is challenging task. Using the RIE technique, an inorganic film deposited on a polymer substrate is exposed to oxygen plasma, which attacks the polymer substrate at the location of the defects in inorganic films selectively as previously explained in Chapter 2. Due to the undercutting of the polymer substrate underneath the micro-scale defects in the inorganic film by oxygen plasma, the location and size of defects can be detected. However, repeated observation of over 10 areas of PECVD-deposited SiO_x and SiN_x on PET substrates revealed no obvious microscopic defects after careful cleaning and handling in a clean-room environment. These results are in agreement with previous reports that great care for keeping the substrate clean and depositions thicker than the critical thickness can remove most micro-scale defects.[27, 29] This experiment strongly suggests that nano-scale defects and the amorphous lattice of the films are the dominant permeation paths for water vapor and oxygen when very poor barrier coatings which possess micro-scale defects are excluded.

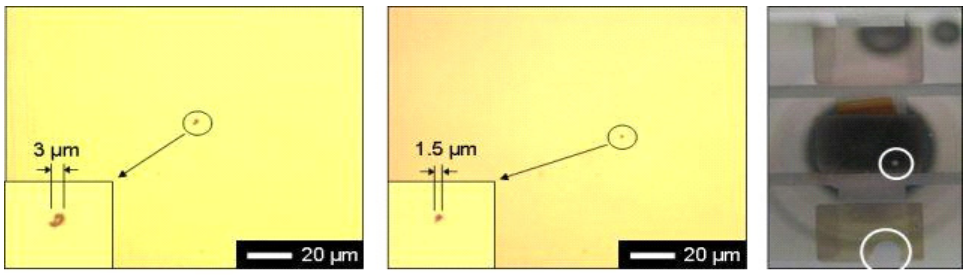

Figure 4.5 Optical microscope images show the micro-defects on SiO_x–coated PET (a) and SiN_x–coated PET (b). Image (c) shows the partial oxidation of a Ca sensor due to micro-defects on the substrate.

The permeation through both nano-scale defects and the amorphous lattice results from the "imperfection" of the PECVD process. Bulk SiO_x (amorphous glass) is impermeable to water vapor and oxygen due to the very constricted interstitial spaces in the Si-O lattice,[29] while either SiO_x or SiN_x thin films fabricated by PECVD have many defects resulting in the dominant permeation paths for water vapor and oxygen. Both SiO_x and SiN_x deposited by PECVD start to grow in the form of islands, and these islands nucleate on the substrate surface. Films are produced by coalescence with adjacent clusters as shown in the Figure 4.6. This growth mechanism of the PECVD process results in a series of columns or cones around individual nucleation sites at the end of the deposition as shown in the surface morphology of Figure 2.3 and Figure 4.7. However, it should be noted that the formation of islands and nucleation are not equilibrium processes; that is, these processes during the film growth never reach the thermo-dynamic equilibrium. As a result of the non-equilibrium process, it produces an "imperfect" glass structure with nano-scale defects and an irregular surface providing the primary permeation paths for water vapor and oxygen. Some of the defects are passivated by other coalescence processes (circled area in the Figure 2.3 (c)) during the PECVD process, while others are not passivated and result in unhindered permeation paths for water vapor and oxygen (described as a channel in the Figure 4.6 (d)).

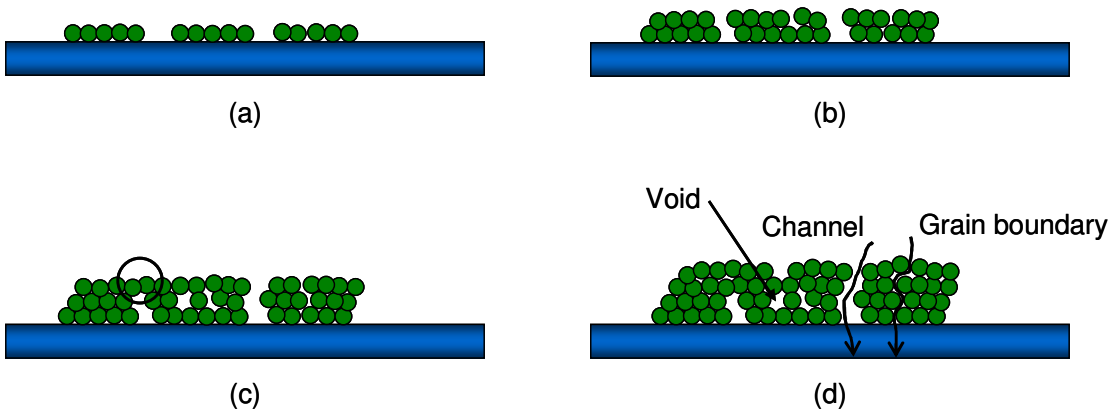

Figure 4.6 Schematics show the mechanism of PECVD deposition. In the first nucleation step during the PECVD deposition, there are many permeation paths as shown in (a) and (b). As the thickness of film is increased, it produces a more continuous film resulting in good surface coverage with limited permeation pathways as seen in (c). After certain thickness called as critical thickness, most defects have been sealed with only a characteristic porosity remaining as seen in (d) and the film quality does not change with thickness.

These imperfect structures of PECVD-deposited thin films were also proven using treatment with activated rate theory by Sobrinho et Al. as explained in section 2.3. [32] The reported activation energy (ΔE_p) for oxygen transport through PECVD-deposited SiO_x on polycarbonate (PC) substrates ranges between the value of bare polymer substrate (17 kJ/mol for PC substrates) and amorphous glass (80 – 100 kJ/mol for a well-constricted SiO_x matrix). Activation energy was defined as a measure of the energy required to elevate the permeant to the activated state and to distort the barrier matrix so that permeant can move into the next vacancy.[109] Therefore, activation energy of oxygen through the fabricated thin film is strongly dependent on the film quality.[29] For example**,** if unhindered permeation through nano-scale defects such as channels or relatively wide grain boundaries is dominant over the hindered permeation through the amorphous lattice or very narrow grain boundaries (comparable with the dynamic diameter of the permeant, 0.33 nm for oxygen[31]), the activation energy of oxygen is closer to that of bare substrate. If the situation is converse, the activation energy should reflect closely that obtained for amorphous glass.

Therefore, it is crucial to investigate the surface morphological characteristics of these layers in order to identify the expected permeation path for water vapor and oxygen through the inorganic layers. Surface characterization of these coatings by AFM has shown that such coatings can be described as a grain like structure,[110] and this was also verified by AFM scanning in this study (Figures 2.3 and 4.7). AFM roughness measurements have shown that the barrier performance generally improves with decreasing surface roughness.[29] A Dimension 3100 scanning probe microscope (Veeco) with tapping mode was used for surface morphology characterization of PECVD-deposited inorganic films. First, height data images of PECVD-deposited SiO_x on a glass substrate are shown in Figures 2. 3 (a) - (c) in different resolutions. A number of areas were scanned in the same manner, and the shown images are typical morphologies of SiO_x films on a glass substrate. Based upon these images, the principal defect structure of the PECVD coatings consists of nano-scale defects instead of micro-scale defects, which were detected by neither AFM scanning nor optical microscopy after RIE. It is suggested that such nano-scale defects provide permeation paths for the unhindered permeation of water vapor and oxygen as explained in the previous section.

Identical AFM studies were conducted on SiN_x on glass substrates to investigate the difference in the barrier performance between the two coatings arising from the surface morphology and roughness, and corresponding images are shown in Figures 4.7 (a) - (d). The RMS roughness of SiO_x and SiN_x are 3.7 nm and 0.5 nm (over 1μm × 1μm), respectively. Compared with the surface of SiO_x, that of SiN_x consists of densely packed grains with smaller lateral size resulting in less defects and a smoother surface. Such fine features in SiN_x are responsible for the low permeation rate of water vapor and oxygen. Furthermore, the grains and grain boundaries of SiO_x are clearer and better defined, which may favor the formation of defects in the films and form diffusive pathways in the coatings.[29] The difference in the surface morphologies between two coatings can be seen clearly in the 3-D topographical images included in Figure 4.7.

When compared on a fixed vertical scale (height range of 15 nm), the topography of the SiN_x coatings appears to consist of small grain features. This suggests that SiN_x coating are fabricated more densely, resulting in less nano-scale defects compared to SiO_x coating.

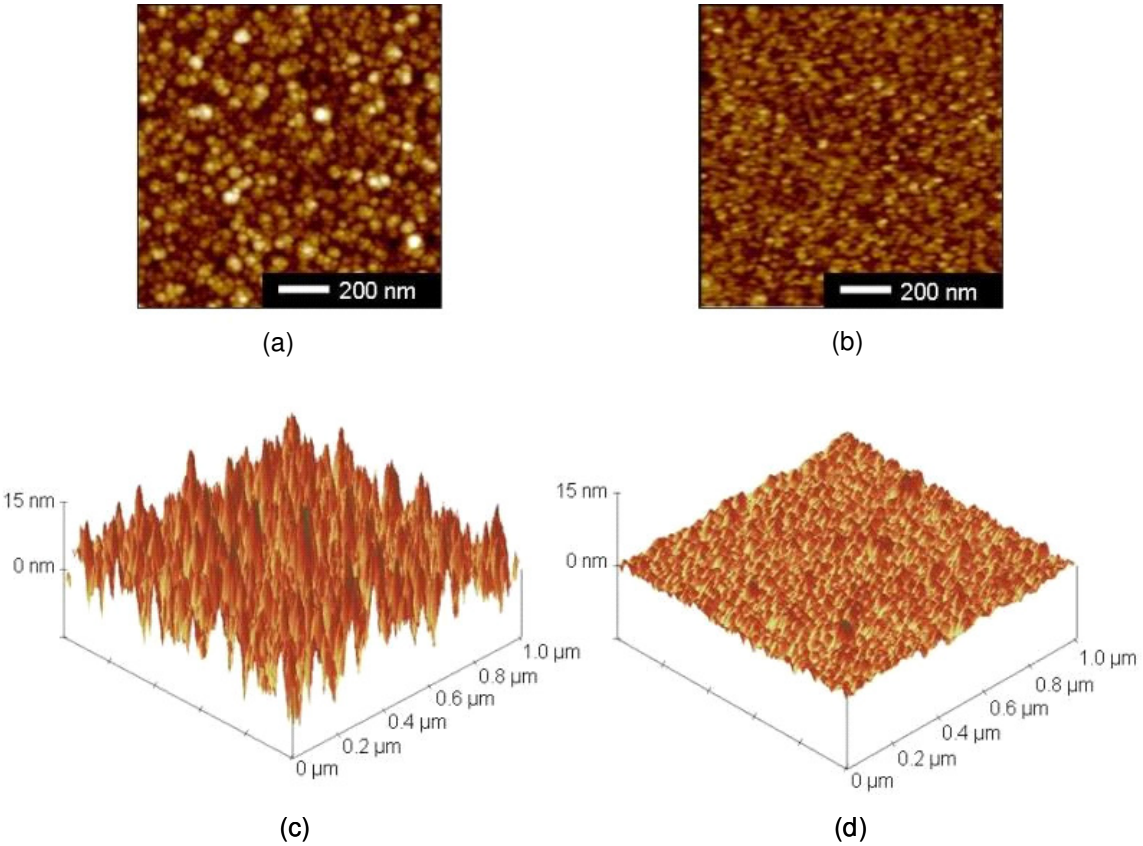

Figure 4.7 AFM images show the surface morphologies of SiO_x and SiN_x coatings deposited by PECVD on glass substrates from an orthogonal perspective (a) and (b), respectively, and 45° angle (c) and (d), respectively.

4.5 Summary

The goal of this chapter was to achieve high performance barrier films by applying alternating organic and inorganic films and establish the correlation between the number of barrier layer and the barrier performance. To this end, multilayer films consisting of both SiN_x/parylene and SiO_x/parylene were evaluated using Ca corrosion test and they demonstrated the ability to provide high barrier performance. The effective

WVTR values for 3 dyads of annealed SiN_x/parylene and SiO_x/parylene were $7.3 \pm 5.0 \times 10^{-6}$ and $6.6 \pm 3.1 \times 10^{-5}$ g/m^2/day, respectively. The effective WVTR of the multilayer encapsulation was found to be a strong function of the number of dyads. Overall, SiN_x/parylene structure outperformed SiO_x/parylene suggesting the quality of the inorganic layer is dominant on the overall barrier performance in multilayer structures. In addition, the barrier performance is improved significantly by up to 96 % by annealing the parylene layer. By annealing parylene including stacked multilayer structure, water absorbed in multilayer structure can be reduced resulting in significant WVTR drop in the transient region. Investigation by optical microscopy after RIE suggests that the dominant permeation path for water vapor is not the defects caused by particle contamination but the imperfect structure of inorganic film. Great care for cleaning and putting the fabrication process in a clean room environment can reduce the defects originating from particle contamination. The surface characterization of inorganic film was performed using AFM to investigate the structure of inorganic films. While it is believed that water permeates through the imperfect structure of inorganic layer such as channels, voids, and grain boundaries, it is still controversial which path is more dominant for water permeation. However, it is possible to investigate how the permeation properties of each constituent films impacts the overall barrier performance. This study will be presented in the next chapter.

.

CHAPTER 5

PEMEATION MECHANISMS THROUGH MULTILAYER FILMS

5.1 Overview

Some of the recent analytical calculations show that the barrier performance of multilayer structures is dependent not only on the equilibrium permeation rate but also on lag time.[25] The lag time indicates how long it takes to reach equilibrium state permeation and can be up to several years, which may be longer than the required lifetime of the encapsulated organic devices. In addition, the permeation rate in the transient region is generally lower than the steady state (SS) permeation rate, so characterizing the barrier performance simply from the initial transient period yields an underestimation of total permeation rate for long-term applications. As a result, the overall barrier performance should include the permeation rate in SS conditions as well as the lag time in the case of multilayer structures. In this chapter, we introduce the analytical calculation of lag time for both single and multilayer structures and the calculation of the total permeability and the permeation rate from the individual properties of each constituent film. By comparing calculated data with experimental data, the range of effective diffusion coefficient (D) and solubility coefficient (S) of constituent films are extracted.

The first goal of this chapter is to simulate the impact of the D and S on the calculated lag time and SS WVTR of the multilayer structure. Then, the second goal is to deduce the range of D and S for water vapor permeation through the films of the multilayer structure by comparing calculated lag time and SS WVTR with experimental data from Ca corrosion test. These deduced values of D and S for each film cannot represent the actual constituent films in the multilayer structure precisely because we

neglect the effects which may arise at the interface of organic and inorganic films and non-ideal behavior of water vapor in the calculation. Such effects are lumped into the *S* and *D* values extracted from the experiments. However, through this study, we can estimate the rages of effective *D* and *S* and explore how those parameters impact the overall barrier performance in the multilayer structures and this can be critical guidelines for designing efficient encapsulation structures.

5.2 Basic Theory

5.2.1 Lag Time

Lag time was defined as required time for system to become equilibrium state. In order to help understand this concept in the diffusion, Figure 5.1 shows initial and boundary condition with zero concentration for one side and constant for the other side and conceptual plot of time dependent concentration. As shown in Figure 5.1 (b), concentration becomes time independent when system is at steady state after lag time.

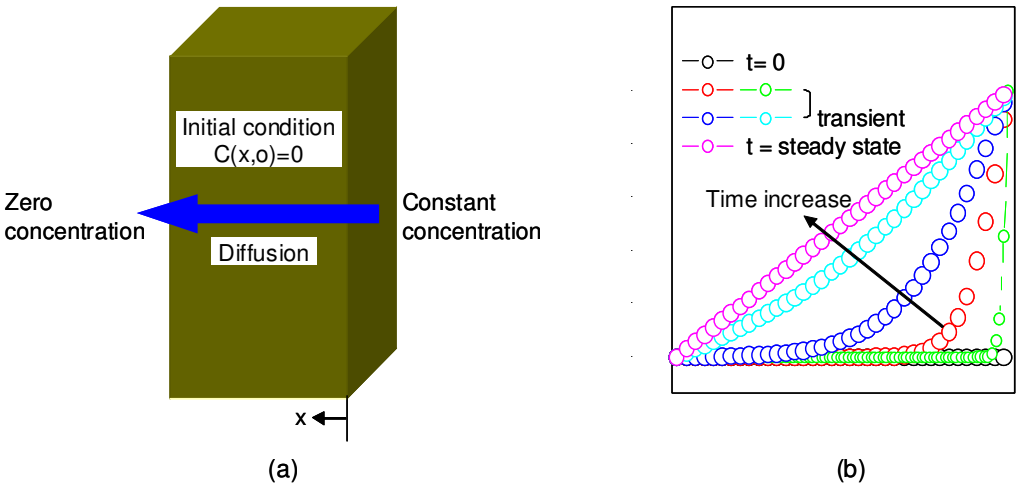

Figure 5.1 (a) Diffusion through a single layer showing initial and boundary conditions. (b) Conceptual plot for time dependent concentration.

We consider the diffusion of water vapor through a multilayer consisting of *n*-component films. Each constituent film is formed of a different material with a different thickness as shown in Figure 5.2. Here, we provide simply the basic idea of this

approach for lag time calculation. A detailed derivation can be found in other references.[25, 111, 112] In this study, we assume that the properties of all materials are independent of concentration and that the diffusion follows Henry's law. The concentration at interface, λ, and flux, J, are time dependent in the transient region, but they become independent of time after the lag time. In the case of the steady state condition,

$$\lim_{t\to\infty} J(t) = J_{ss} \tag{5.1}$$

and J_{ss} can be written in the form of equation (5.4) derived from equation (5.3) which is the diffusion equation for 1-dimensional and steady state condition. Similarly, time dependent $J(t)$ is in the form of (5.6) from (5.5) which is that for 1-dimensional and transient condition. Also, $C_i(x,t)$ is the concentration at position x in the ith component and it becomes steady state as time goes to infinity,

$$\lim_{t\to\infty} C_i(x,t) = C_i(x) \tag{5.2}$$

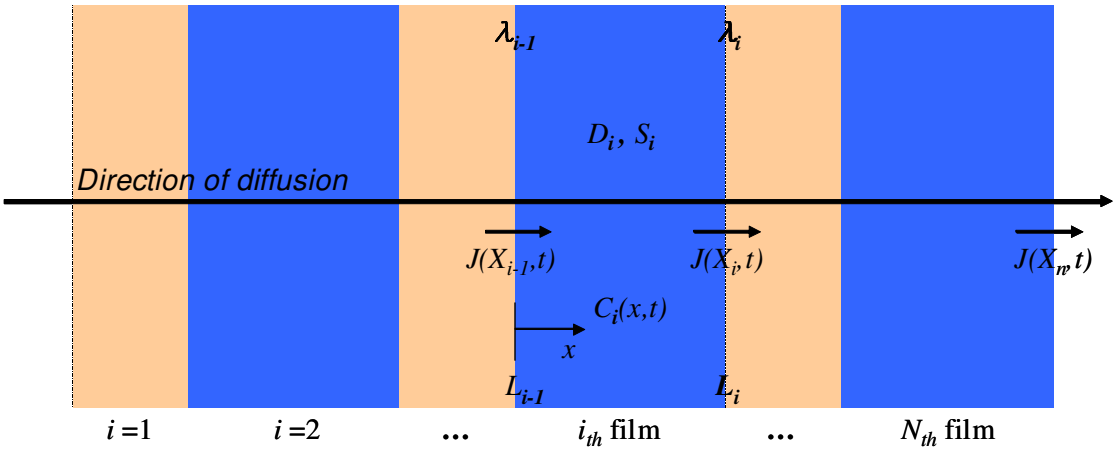

Figure 5.2 Diffusion through a multilayer consisting of n layers showing concentration, flux, and location notations.

$$\frac{d}{dx}\left(D_i \frac{dC_i(x)}{dx}\right) = 0 \tag{5.3}$$

$$J_{ss} = \lambda_1 \sum_{i=0}^{n} \frac{D_i}{\prod_{j=0}^{i-1} k_j} \tag{5.4}$$

$$\frac{\partial C_i(x,t)}{\partial t} = \frac{\partial}{\partial x}(D_i \frac{\partial C_i(x,t)}{\partial x}) \tag{5.5}$$

$$J(X_n,t) = [\sum_{i=1}^{n} \{H_i\}^{-1}[\lambda_1 - \sum_{i=1}^{n} \{\frac{1}{D_i}(\prod_{j=0}^{i-1} K_j)\int_{X_{i-1}}^{X_i}\int_{x}^{X_i} \frac{\partial C_i(x,t)}{\partial t} dx dx\} - \sum_{i=1}^{n} \{H_i \sum_{b=i+1}^{b} \int_{X_{b-1}}^{X_b} C_b(x,t) dx\}] \tag{5.6}$$

The total quantity of permeant, $Q(t)$, up to time t through a unit area can be calculated by integrating the transient flux, $J(X_n,t)$, from 0 to time t. This value is the same as the area under the curve $J(X_n,t)$ as a function of time, t as shown in the Figure 5.3 (a). As time goes to infinity, $Q(t)$ approaches Q_a which is the asymptotic value as shown in Figure 5.3 (b). This Q_a should be equal to $J_{ss} \times (t\text{-}L)$ (Equation (5.8)), where L is the lag time and J_{ss} is the flux of permeant at the steady state condition as shown in equation (5.4).

$$Q(t) = \int_0^t J(X_n,t) dt \tag{5.7}$$

$$\lim_{t\to\infty} Q(t) \to Q_a = J_{ss} \times (t - L) \tag{5.8}$$

Hence, on substituting equation (5.4) and (5.6) into equation (5.8), the lag time can be derived as follows:

$$L = \frac{\sum_{i=1}^{n} \{\frac{L_i^2}{2D_i} \sum_{i=1}^{n} [\frac{L_m^2}{D_m} \prod_{j=1}^{i-1} k_j] - \frac{L_i^3}{3D_i^2} \prod_{j=1}^{i-1} k_j\} + \sum_{i=1}^{n} \{\frac{L_I}{D_I} \prod_{j=1}^{i-1} k_j \sum_{\beta=i+1}^{n} [\frac{L_\beta}{\prod_{j=1}^{\beta-1} k_j} \sum_{m=\beta}^{n} (\frac{L_m}{D_m} \prod_{j=1}^{m-1} k_j) - \frac{L_\beta^2}{2D_\beta}]\}}{\sum_{i=1}^{n} \frac{L_i}{D_i} \prod_{j=1}^{i-1} k_j} \tag{5.9}$$

where $k_j = S_j/S_{j+1}$. In the case of n=1 (single layer), lag time is simply a function of thickness and D of the film as follows:

$$L = \frac{L_{film}^{\ 2}}{6D} \tag{5.10}$$

In contrast to the case for a single layer, the lag time for multilayer (n ≥ 2) is a function of thickness and *D* as well as *S* of the films. Hence, *D* as well as *S* should be considered for analyzing the overall barrier performance. In this section, the overall barrier performance includes SS permeation rate as well as lag time because long lag time can effectively extend the lifetime of organic devices as explained previously.

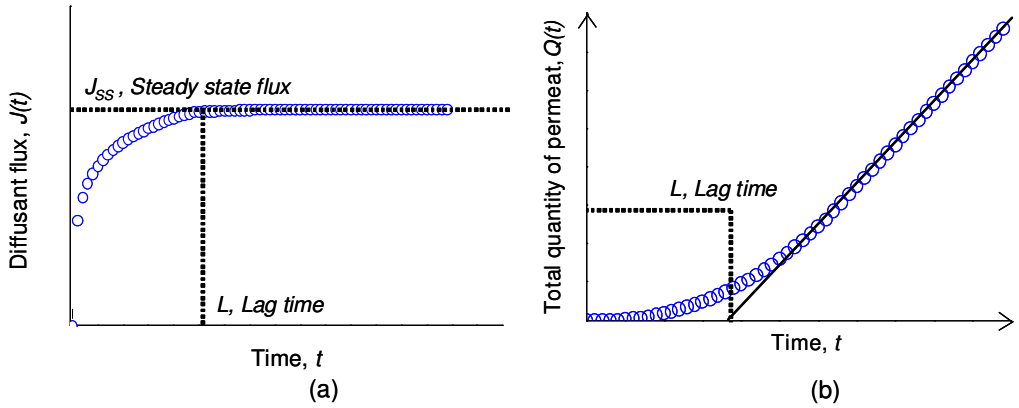

Figure 5.3 (a) Conceptual plot for permeant flux, *J(t)* and it becomes steady state after transient state. (b) Conceptual plot of total (cumulative) quantity of permeant, *Q(t)* and it can be calculated by integrating *J(t)* with time. After transient state, *J(t)* becomes constant and *Q(t)* approaches asymptotic value (Q_a).

5.2.2 Steady State Permeability

Calculation and prediction of water vapor permeability or permeation rate through multilayer films from the permeability data of each constituent film is important in designing high barrier encapsulation for organic electronics. We summarize the equations for the calculation of permeability or permeation rate of water vapor through multilayer films in steady state. Transmission rate (*TR*) refers to the amount of permeant (*Q*) passed through the unit area (*A*) of a tested film during time (*t*) under a pressure difference (Δp) of permeant across the film thickness at a certain temperature and vapor pressure.

$$TR = \frac{q}{At\Delta p} \tag{5.11}$$

$$P = TR \cdot L = \frac{qL}{At\Delta p} \tag{5.12}$$

For multilayer structures, total TR_T and total permeability P_T of films with n layers can be calculated with the equations below.

$$TR_T = \frac{1}{\frac{1}{TR_1} + \frac{1}{TR_2} + \frac{1}{TR_3} + \ldots + \frac{1}{TR_n}} = \frac{1}{\frac{L_1}{P_1} + \frac{L_2}{P_2} + \frac{L_3}{P_3} + \ldots + \frac{L_n}{P_n}} \tag{5.13}$$

$$P_T = \frac{L_T}{\frac{L_1}{P_1} + \frac{L_2}{P_2} + \frac{L_3}{P_3} + \ldots + \frac{L_n}{P_n}} \tag{5.14}$$

By using these equations, we can calculate and predict the total permeability and transmission rate of multilayer films based on the data of individual materials.

5.3 Analytical Simulations

We simulate how D and S impact the calculated lag time and effective SS WVTR using the equations explained in the previous section. By comparing the simulation data with experimental data from Ca tests, the ranges of D and S can be deduced. Experimental results in the Figure 5.4 show lag time data for multilayer encapsulation structures from 1 to 4 dyads of SiN_x/parylene, and the results are summarized in Table 5.1. As listed in Table 5.1, lag time increases as the number of dyads increases, but no clear correlation such as a linear or exponential correlation between the lag time and the number of dyads exists. Also, the effective WVTR in the SS region are summarized in Table 5.1 for comparison with calculated results. Figures 5.4 and 5.5 show the normalized conductance change as a function of time for each dyad to show transient and SS region and those in specified ranges for each sample, respectively. The effective SS WVTR dropped at least one order of magnitude in samples with more than 2 dyads of SiN_x/parylene. Although one order of magnitude drop in SS WVTR was measured between 2 and 3 dyads, it is not clearly understood. It is just believed that the non-ideal

behavior of water vapor, such as an interaction with the films and accumulation of water vapor between films, becomes more significant as the number of dyads increases.

Table 5.1 Lag time and steady state effective WVTR for multilayer structures with 1 ~ 4 dyads of SiN_x/parylene evaluated by Ca corrosion tests

	1 dyad	2 dyads	3 dyads	4 dyads
Lag time (h)	10	355	1250	1980
Effective WVTR in SS region ($g/m^2/day$)	0.036	0.029	0.0032	0.0026

Table 5.2 The values of *D* and *S* from the literature, and the ranges of *D* and *S* for the parametric study.[25, 113]

	Inorganic layer (Effective values)			Organic layer		Defect spacing (μm)
	S ($g/cm^3/atm$)	*D* (cm^2/s)	*P* (g/cm/atm/s)	*S* ($g/cm^3/atm$)	*D* (cm^2/s)	
Ref. values	0.029*	10^{-11}-10^{-13}*	2.9×10^{-14}*	0.05*	2.6×10^{-9}*	0 ~ 1000**
Ranges in this study	N/A	10^{-11} ~ 10^{-14}	10^{-13}-10^{-16}	0.005 - 0.1	10^{-8} ~ 10^{-11}	0 ~ 1000

* [27], ** [115]

To deduce the values of *D* and *S* of the constituent films, we first investigate how *D* and *S* of each individual film in the multilayer structure impacts the calculated lag time and SS WVTR, and then compare them with the experimental data. For this purpose, we set the baseline for the ranges of *D* and *S* for inorganic and organic films based on the reported data in the reference, which are summarized in the Table 5.2. The presented values for *D* and *S* of inorganic films are not direct measurement data but are instead deduced from lag time data.[25] It is difficult to measure individual permeation properties of inorganic film. Furthermore, simple measurement of a single inorganic layer may not present the individual film properties of those found in the multilayer structures because it was reported that alternating organic and inorganic barriers results in synergistic effects such as the reduction of substrate-induced defects through surface planarization.[114] Also,

it is generally characterized by a diffusion coefficient and porosity instead of solubility in the case of water vapor permeation through inorganic film because permeation of water vapor occurs through defects in inorganic layer.[24] Hence, *P* is described by *D* multiplied by porosity (*e*) instead of *D* and *S*. However, for our purpose of this chapter, we use *P* instead of separate *D* and *e* for simplicity.

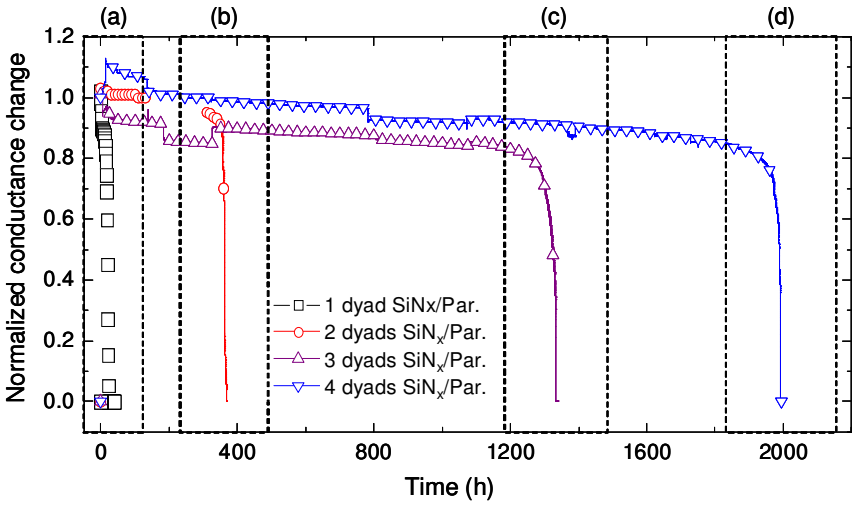

Figure 5.4 Change in the normalized conductance of Ca sensors as a function of time shows that lag time depends on the number of dyads for 1~4 dyads of SiN_x/parylene.

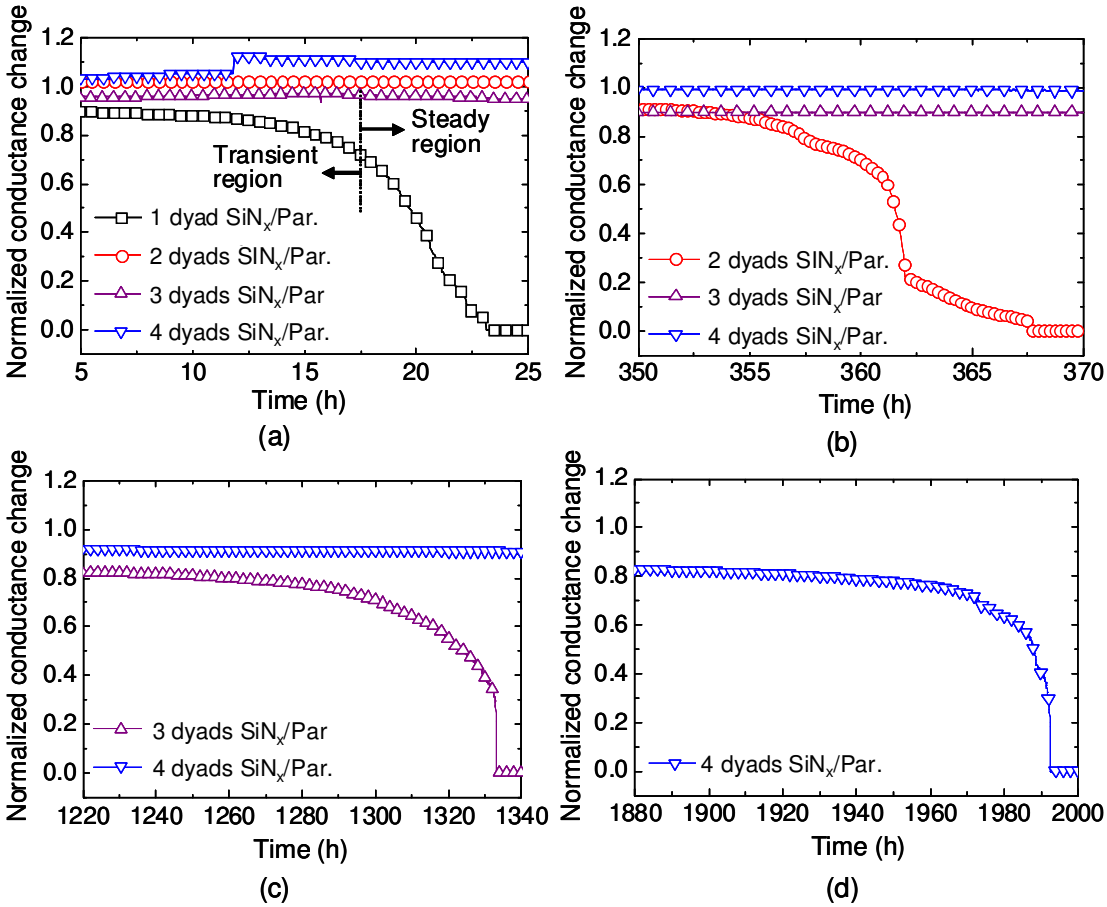

Figure 5.5 Graphs (a) - (d) show the same data in Figure 5.3 with specified ranges for each sample.

5.3.1 Impact of Permeation Properties of Organic Film

First, the value of *D* for organic films were varied within the ranges and other values are fixed as listed in Table 5.2. Figure 5.6 shows effect of *D* of organic film on the lag time and the SS WVTR. Changes in *D* of organic film have only a minor effect on both lag time and the effective SS WVTR within the general range of values for polymeric films. The ranges of the diffusion coefficients of organic films are far higher than those of the inorganic films, so they have negligible effect on the overall barrier performance of multilayer structures. Next, the effect of the *S* of the organic films was investigated to explore its impact on the overall barrier performance. *S* of the organic film has only a minor impact on the SS WVTR, while it has impact on the lag time as

shown in the Figure 5.7. Increasing *S* of the organic film results in longer lag time without increasing the SS WVTR. While this change is beneficial to the overall barrier performance, it should be noted that high *S* of organic film causes additional problems related to dimensional stability, adhesion, and mechanical integrity of the multilayer structure.[25]

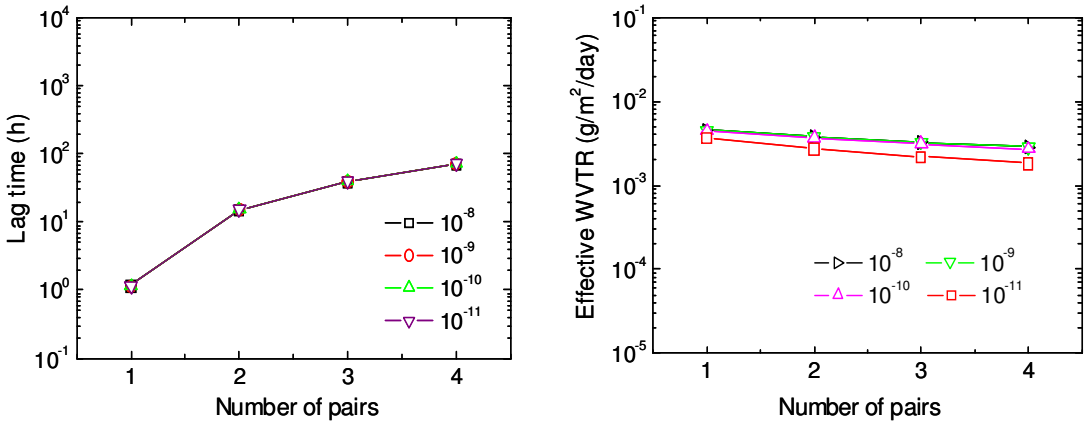

Figure 5.6 Calculated lag time (a) and the effective SS WVTR (b) as a function of the number of dyads for different *D* values in the organic films.

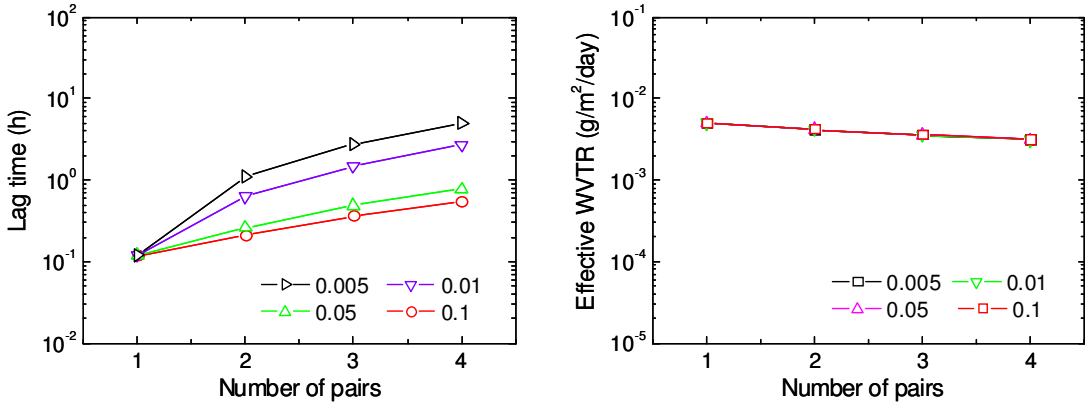

Figure 5.7 Calculated lag time (a) and the effective SS WVTR (b) as a function of the number of dyads for different *S* values in the organic films.

5.3.2 Impact of Permeation Properties of Inorganic Film

As previously mentioned in the beginning of this section, we use only *P* instead of separate *D* and *S* because the use of *S* for the inorganic layer is not physically consistent with permeation mechanism of water vapor through inorganic films. The value of *P* for inorganic films were varied within the range of those shown in Table 5.2 while other values were fixed. To obtain *P*, we utilized the diffusion coefficient and effective solubility shown in other references, combining them to create the reference permeability range for *P* (*P*= *DS*). Figure 5.8 shows the effect of *P* of the inorganic film on the lag time and the SS WVTR. *P* has a significant effect on both the lag time and the effective SS WVTR. Hence, *P* of the inorganic film plays an important role in the barrier performance of multilayer structures.

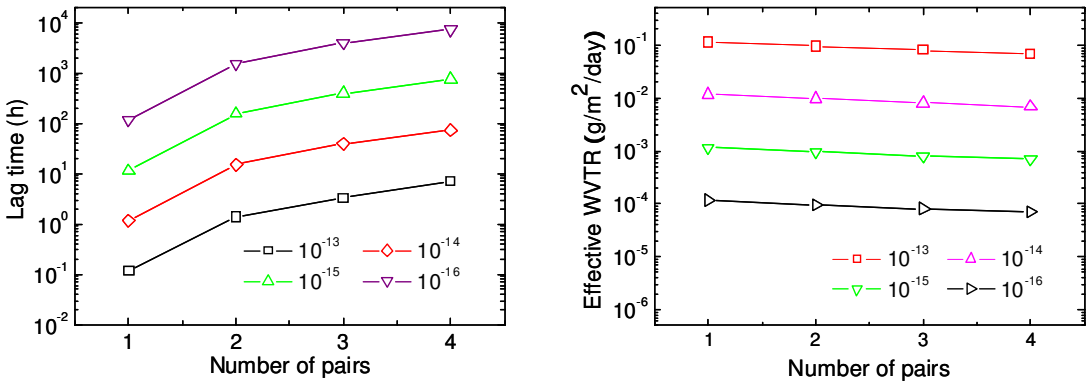

Figure 5.8 Calculated lag time (a) and the effective SS WVTR (b) as a function of the number of dyads for different *P* values in the inorganic films.

5.3.3 Impact of Effective Permeation Path

For the calculated SS WVTR to match the experimental data summarized in Table 5.1, *P* of the inorganic film should be on the order of 10^{-14} cm^2/s and on the order of 10^{-17} cm^2/s to match the lag time. Required *P* values of inorganic film for each dyad were summarized for each criterion in Table 5.3. Based upon these results, there are at least

two orders of magnitude difference in the *P* of inorganic film needed to match both lag time and the effective SS WVTR simultaneously. Hence, it leads that different permeation mechanism of water vapor in the multilayer structure is expected to be different from what has been assumed for these calculations. As shown in the Figure 5.8, water vapor permeates through either micro-size defects such as channels or nano-size defects such as grain boundaries, and it is not clear which mechanism is more dominant for water vapor diffusion through inorganic thin film. Hence, "effective" diffusion permeation path is used instead of diffusion permeation path simply. Those permeation mechanisms through inorganic films were explained in details in Chapter 2 and 4. As a result, the permeation through micro-size defects should be considered when defect spacing, *L*, is much longer than the physical thickness of organic layer, *t*, as shown in Figure 5.9. In this case, permeated water vapor via defect in inorganic layer keep flowing through organic layer until there is another defect in the next inorganic film resulting in long effective permeation path as well as long lag time. Hence, the effective diffusion length, *L,* for water vapor permeation should be the defect spacing instead of physical thickness of organic layer, *t*.

Table 5.3 *P* of inorganic film required to match WVTR and lag time, respectively.

	1 dyad	2 dyads	3 dyads	4 dyads
P (cm^2/s) based on SS WVTR	2.1×10^{-13}	2.2×10^{-13}	1.0×10^{-14}	2.1×10^{-14}
P (cm^2/s) based on lag time	2.7×10^{-16}	3.6×10^{-17}	1.7×10^{-17}	2.0×10^{-17}

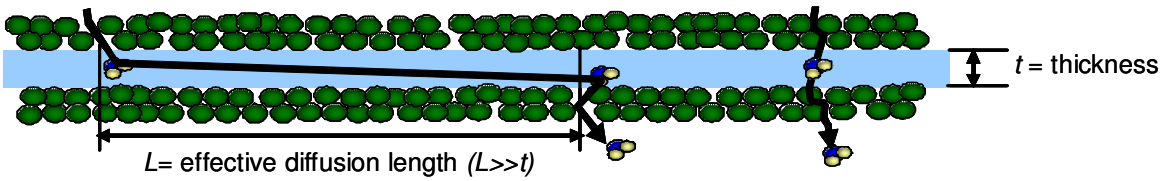

Figure 5.9 Diagram which shows that water vapor permeates via defects in an inorganic film and flows through effective diffusion path in an organic film with an effective permeation path *L*.

By considering this effective long permeation path, *P* of inorganic film required to match both lag time and effective WVTR simultaneously can be deduced. Required length of effective permeation path is summarized in Table 5.4 for each dyad. For the purpose of deducing *P* of inorganic film, results using QCM in the chapter 4 were used for *D* and *S* of organic films. In order to match the measured lag time as well as the effective SS WVTR simultaneously, the value of *P* of inorganic film should be 2.3×10^{-14} g $cm^2/cm^3 s$ atm with 539 μm effective permeation path in the case of 3 dyads SiN_x/parylene. As previously mentioned, it is more practical to report permeation properties with *P* instead of separate values for *D* and *S* in the case of inorganic film.

Table 5.4 Length of effective diffusion path for each pair required to match lag time and SS WVTR simultaneously.

	1 dyad	2 dyads	3 dyads	4 dyads
Length of effective permeation path (μm)	NA	558	539	494

Based on deduced values from criteria for 3 dyads of SiN_x/parylene, Table 5.5 shows comparison between calculated and experimental values of lag time and SS WVTR for each dyad. As listed in the Table 5.5, SS WVTR mismatch in samples of 1 and 2 dyads might be partially due to critical thickness issue. It is well know that permeation rate is not inversely proportional to the film thickness in the case of deposited thin film but the rate is inversely proportional to the thickness in the caser of calculation. Also, lag time mismatch in samples of 2 and 3 dyads is expected due to absorbed water during encapsulation process which could not be considered in lag time calculation.

Table 5.5 Calculated and experimental SS WVTR and lag time for each pair based on values deduced from criteria for 3 dyads of SiNx/parylene.

		1 dyad	2 dyads	3 dyads	4 dyads
SS WVTR (g/m^2day)	Experiment	0.036	0.029	0.0032	0.0026
	Calculation	0.0044	0.0037	0.0032	0.0027
Lag time (h)	Experiment	10	355	1280	1980
	Calculation	2	448	1280	2273

In addition, this analytical calculations show that a lag time can be achieved up to four years (35,000 h) which is much longer than the standard lifetime of an OLED (10,000 h) in the case of four dyads of organic/inorganic films with defect spacing of 500 μm, 10^{-15} g cm^2/cm^3s atm of the inorganic film. This suggests that combining organic and inorganic layers in a multilayer structure provides not only low steady-state permeation rate in both transient and steady state region but also an additional effect of long lag time. Hence, the lag time should be considered when designing multilayer encapsulation for efficient designing encapsulation structure. Furthermore, lag time can be further increased by employing dessicant in the encapsulation structures.

5.4 Summary

The goal of this chapter was to calculate how *D* and *S* of organic and inorganic films impact on the overall barrier performance of multilayer encapsulation structure. To this end, equations for calculating lag time and SS WVTR were derived and presented. Based on the calculation using these equations, it was found that *P* of inorganic film have a significant impact on both lag time and SS WVTR. In the case of organic film, *D* has a negligible effect on both lag time and steady state WVTR. In contrast, *S* of organic film has a significant impact on lag time as in the case of inorganic film but negligible on SS WVTR. This is because the permeability ($P=DS$) of inorganic film is at least three orders of magnitude lower than that of organic film so most resistance to water vapor is from

inorganic film. Hence, the total permeability of multilayer structure by lamination theory which was introduced in section 5.2.2 is dominantly dependent on the permeability of the inorganic film.

By comparing the calculated lag time and the effective SS WVTR with experimental data from Ca corrosion tests, the values of effective *P* of inorganic film were deduced. However, there was no value to match both calculated lag time and SS WVTR with experimental data simultaneously with a given geometry. Hence, it was necessary to allow the thickness of organic layer to vary, which corresponds the length of effective permeation path of permeant through organic film. Value for effective *P* of inorganic film were then found to be 2.3×10^{-14} g cm^2/cm^3s atm with 539 μm effective permeation path in the case of 3 dyads SiN_x/parylene.

Based on simulation results, it suggests that combining organic and inorganic layers in a multilayer encapsulation structure provides not only low SS WVTR but also an additional effect of long lag time. Hence, the lag time should be considered when designing efficient multilayer encapsulation structure for organic devices. Also, it should be noted that lag time and SS WVTR were calculated based on assumptions of ideal behavior of water vapor. It means that there is neither interaction between water vapor and barrier layers nor accumulation of water vapor between barrier films in our simulation.

CHAPTER 6

SINGLE AND HYBRID-LAYER ENCAPSULATION

6.1 Overview

In this chapter, single-layer encapsulation films based on an Al_2O_3 layer deposited by ALD is introduced. While PECVD-deposited SiO_x and SiN_x were investigated by using Ca corrosion tests, neither layer has sufficient barrier performance to be the sole encapsulation layer for organic electronic devices. In the case of a single 100 nm layer of either SiO_x or SiN_x on a Ca sensor, oxidation of the encapsulated Ca sensor was observed to be very rapid. Films deposited by PECVD were found to have many defects which provide unhindered permeation paths for water vapor and oxygen resulting in low barrier performance. Therefore, thin films deposited by PECVD, which are desirable for their fast deposition rates at low temperatures, can be used effectively only in hybrid structure, which will be presented in this chapter and multilayer structures, Single layer and hybrid layer films are desirable as they simplify the encapsulation architecture and can possibly reduce processing time when compared to multilayer films. The key is to develop processing methods which can reduce the number of defects in order to eliminate unhindered permeation through the films.

In contrast to PECVD films, ALD processing provides a method to deposit high quality films with low defect density. Hence, the first goal of this chapter is to fabricate high performance single barrier layer having equivalent barrier performance of multilayer structure. The barrier performance was characterized using Ca corrosion tests and results are presented in the next section. Additionally, the long-term stability of Al_2O_3 films was investigated because it was reported that water condensation on Al_2O_3 can cause corrosion of the film. While single layer films deposited by ALD has a high barrier

performance, its processing time is too long for high-speed and low-cost manufacturing. Hence, the second goal of this chapter is to circumvent long processing time of ALD and propose newly developed hybrid encapsulation structure. This structure combines the advantages of fast deposition of PECVD and high quality of ALD processing, and results are presented. The proposed hybrid encapsulation structure can satisfy the stringent barrier requirements for the encapsulation of organic devices as well as can be produced with a simplified fabrication process.

6.2 Single-Layer Encapsulation

Single-layer encapsulation films made from Al_2O_3 deposited by ALD were first analyzed to determine their WVTR properties. Samples were deposited directly on Ca samples and measured in an environmental chamber as discussed below.

6.2.1 Barrier Performance

Barrier film measurements for ALD deposited films were created with a single layer of 100 nm-thick Al_2O_3 which was deposited directly on top of Ca sensors without any interlayer which was in the case of multilayer structures. ALD is a conformal coating, so the side walls of the Ca sensors were expected to be covered by the Al_2O_3 film. Compared to PECVD-deposited SiO_x and SiN_x films, Ca sensors encapsulated with Al_2O_3 oxidized slowly and uniformly enough that the effective WVTR could be measured by Ca corrosion tests. A single layer of ALD-deposited Al_2O_3 with a thickness of 100 nm yielded effective WVTR values of 4×10^{-4} g/m^2/day at 20°C and 50% RH. However, some of samples showed localized oxidation during the Ca corrosion tests as shown in the top and bottom samples in Figure 6.1 (a). By employing optical microscopy on the area where Ca was oxidized partially, the non-uniform oxidation was found to be due to the delamination between the Ca sensors and Al_2O_3 as shown in Figure 6.1 (b)

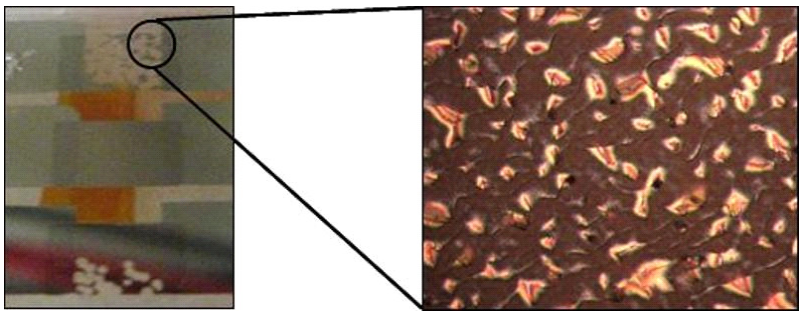

(a) (b)

Figure 6.1 Top and bottom Ca sensors in (a) show partial oxidation while center sensor shows uniform oxidation. Optical microscopy image in (b) shows delamination of Al_2O_3 layer. Uniformity in the Ca oxidation was obtained by using a 1 μm parylene layer underneath the Al_2O_3 which showed negligible impact on the magnitude of WVTR.

To help circumvent the issue of non-uniform Ca oxidation caused by delamination, a 1 μm parylene layer was deposited between the Ca sensors and Al_2O_3. This resulted in very uniform oxidation of the Ca sensors without any statistically significant change in the effective WVTR. No delamination was found with the additional parylene layer. Additional testing of Al_2O_3 was performed by reducing the thickness of the Al_2O_3 layer to 50 nm with a 1 μm-thick parylene interlayer. Again, very uniform oxidation was observed in all samples. This resulted in an average WVTR of 2.8 $\pm$ 1.3 $\times$ 10^{-4} g/m^2/day. As previously mentioned in Chapter 2, an Al_2O_3 films grown by ALD directly on polyethylene naphthalate (PEN) has shown WVTRs on the order of 10^{-3} g/m^2/day as measured by the radioactive tracer method[115] and an effective WVTR of 1.7 $\times$ 10^{-5} g/m^2/day at 38 °C and 85 % RH by using the Ca corrosion test.[40]

6.2.2 Discussion: Long-Term Stability of Al_2O_3 Layer

As shown in previous results, Al_2O_3 films deposited by ALD showed promising results having low permeation rate. However, a previous report has shown that water can corrode Al_2O_3 films.[94] This can be detrimental for long term encapsulation applications. To investigate the long-term stability of Al_2O_3 film, two different types of encapsulation structures were tested on Ca sensors: Al_2O_3 and Al_2O_3/paryelene as illustrated in Figure

6.2. As explained in previous section, 1 μm thick parylene as a buffer layer between Ca sensor and 50 nm thick Al_2O_3 film was deposited. The additional 1 μm thick parylene layer was deposited on top of the Al_2O_3 film to prevent water from condensing directly on top of the Al_2O_3 film. The additional parylene layer does not affect the overall barrier performance because the Al_2O_3 film is primarily responsible for the large resistance to water vapor and oxygen.

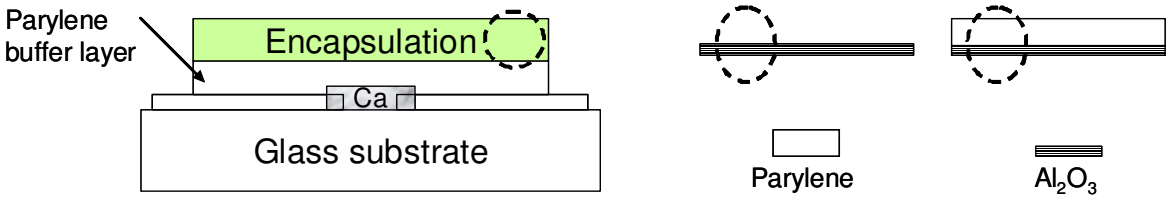

Figure 6.2 Schematics for long-term stability test of Al_2O_3 film on the glass substrate. Circled are indicates encapsulation consisting with either single 50 nm thick Al_2O_3 or Al_2O_3 protected by 1μm thick parylene layer.

The data in Figure 6.3 show that both encapsulation structures maintain similar barrier performance up to 20 days. After 20 days, Al_2O_3 without an additional parylene protecting layer on top of the Al_2O_3 film lost its barrier performance, while the structure with a parylene protecting layer on top of the Al_2O_3 maintained its barrier performance after 4 months. Some of the Ca sensors encapsulated with Al_2O_3 without a parylene protecting layer lost their barrier performance within 20 days. Based upon these results, an additional parylene protecting layer should be used to guarantee the barrier performance of Al_2O_3 thin-film encapsulation in long-term applications.

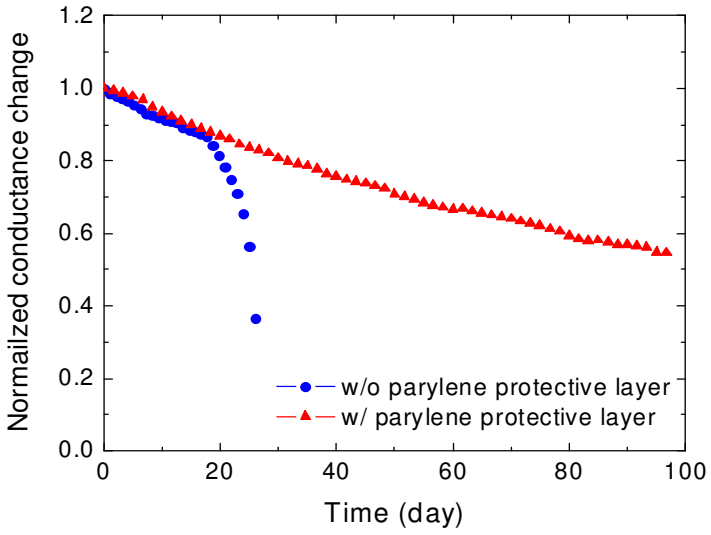

Figure 6.3 Normalized conductance change as a function of time in both Al_2O_3 and Al_2O_3/parylene structures.

6.3 State-of-Art Hybrid Encapsulation

The development of thin-film encapsulation has focused primarily on high quality single layers of inorganic materials as well as multilayer films often containing alternating layers of organic and inorganic materials. Research has shown that the effective WVTRs for multilayer structures have achieved permeation rates of 10^{-5} – 10^{-6} g/m^2/day for structures using 3 – 6 dyads of Al_2O_3/polyacrylate, SiO_x/parylene, or SiN_x/parylene as mentioned in the Chapter 2 and 4.[18, 68] However, their complex architecture and/or the long processing times have proven to be barriers themselves to their integration in actual devices. Overall, it is desirable to develop vacuum deposition methods for thin-film encapsulation which reduces the complexity and processing time while providing high quality films which are scalable to large areas. As an alternative approach, high quality single-layer encapsulation has also been developed While single layer films fabricated by ALD have shown promising results as previously mentioned, the processing time for ALD is too long for high-speed, low-cost fabrication (~ 4 hr for a

25 nm-thick Al_2O_3 film).[40, 115] Therefore, we propose an encapsulation structure which combines the fast processing of PECVD and the high quality of ALD coatings.

Most thin films deposited by PECVD have pinholes and defects, which provide permeation pathways for water vapor and oxygen. Hence, single-layer films deposited by PECVD cannot satisfy the stringent encapsulation requirements of organic electronic devices. This barrier performance of films deposited by PECVD can be improved by combining a high quality and conformal deposition, such as ALD. In this manner, the defects on the first deposited film can be passivated by next film. The-state-of-art for this method is that the first deposited film can be fabricated quickly by PECVD to form the base of encapsulation and the second defect filling layer needs to be deposited ultra-thin, reducing the process time of ALD. This structure showed ultra barrier performance similar to that of multilayer encapsulation but with a simplified geometry.

6.3.1 Barrier Performance

Hybrid encapsulation structures were investigated, and their performance was also examined using Ca corrosion tests. To study the hybrid encapsulation, Ca samples on glass substrates including a 400 nm-thick SiO_x buffer layer, which prevents side permeation as previously described, were prepared in the same way as the multilayer encapsulation structures. After this interlayer was deposited by PECVD, 100 nm of either SiO_x or SiN_x was deposited by the same PECVD process on top of the interlayer to begin the hybrid encapsulation structure. This was followed by depositing 50 nm of Al_2O_3 by ALD. Finally, a 1μm thick parylene layer was deposited on top of the Al_2O_3 layer to prevent corrosion of the Al_2O_3 by water condensation. The schematics in the Figure 6.4 shows the hybrid structure including Ca sensors and buffer layer.

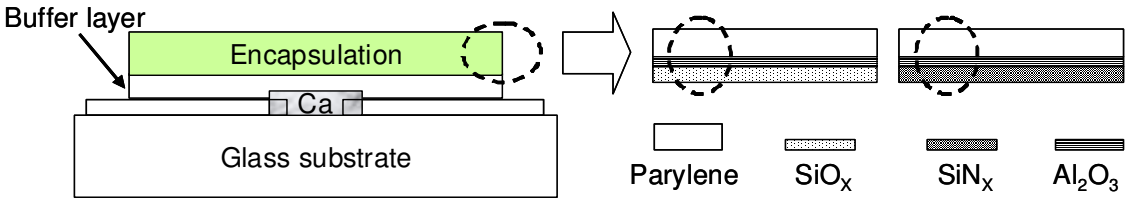

Figure 6.4 Schematics for hybrid encapsulation test structure on the glass substrate. Circles indicate hybrid layer consisting with either 100 nm-thick SiO_x or SiN_x/ combined with 50 nm-thick Al_2O_3 and 1μm thick parylene layer.

The SiN_x/Al_2O_3/parylene and SiO_x/Al_2O_3/parylene barrier films yielded effective WVTR values of $2.3 \pm 1.5 \times 10^{-5}$ g/m^2/day and $3.0 \pm 1.4 \times 10^{-5}$ g/m^2/day, respectively. While multilayer films containing SiN_x deposited by PECVD have been reported to show better barrier performance than SiO_x,[116, 117] our results show that there were no significant difference between the two films when utilized in the hybrid structure. These results suggest that the water permeation through the defects and pinholes in both SiO_x and SiN_x films are well passivated by the Al_2O_3 layer, providing a barrier film with performance similar to multilayer encapsulation but with a far simpler architecture. As performed previously, Al_2O_3 (100 nm)/parylene (1 μm) films and SiO_x (100 nm)/parylene (1 μm) yielded effective WVTR values of $2.8 \pm .3 \times 10^{-4}$ g/m^2/day and $3.1 \pm 0.7 \times 10^{-2}$ g/m^2/day, respectively. Based upon lamination theory calculations,[23, 25] the effective WVTR of the two films combined is expected to be on the order 10^{-4} g/m^2/day, which is one order of magnitude higher than that of the actual measured value. The measured lower permeation rate of the hybrid film is believed to originate from the passivation of defects in the SiO_x layer by the Al_2O_3 layer. Such synergistic effects have been reported in the cases of interlayers between inorganic and organic multilayer encapsulation as well as ALD-deposited Al_2O_3 and SiO_x, and ALD-deposited Al_2O_3, ZrO_2.[19, 41, 62]

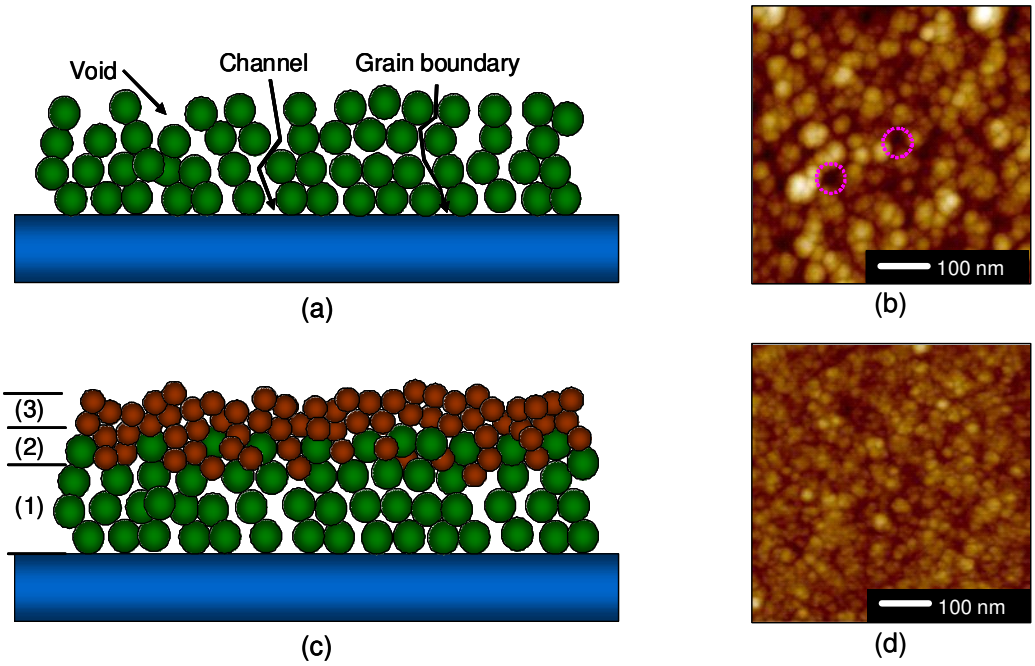

Figure 6.5 (a) Schematic shows expected imperfect structure of PECVD deposited SiOx deposited by PECVD based on AFM images (b). (c) Schematics illustrates the sealing effect of Al_2O_3 on a SiO_x surface: (1) SiO_x, (2) interlayer of SiO_x and Al_2O_3, and (3) Al_2O_3. (d) Surface morphology of Al_2O_3 deposited by ALD on glass substrate.

Figure 6.5 (a) shows the expected imperfect structure of SiO_x film deposited by PECVD from the surface morphology of this film using AFM, which clearly contains voids, and grain formation resulting in relatively a rough surface (root mean square (RMS) surface roughness: 3.8 nm). This imperfect structure of the SiO_x provides a permeation path for water vapor and oxygen as discussed in other reports.[4-8] In contrast, the Al_2O_3 surface in Figure 6.5 (d) consists of densely packed, smaller spherical clusters of Al_2O_3 resulting in a uniformly deposited and smoother surface (RMS surface roughness: 0.5 nm). Therefore, by applying Al_2O_3 by ALD on the SiO_x, the defects in SiO_x can be sealed resulting in expected interlayer region consisting of both SiO_x and Al_2O_3 between the two films (See Figure 6.5 (c)).

Additional studies on the hybrid films were performed by reducing the thickness of the Al_2O_3 to determine its impact on the effective WVTR and defect passivation. By decreasing the thickness of the ALD layer to 10 nm, the effective WVTR of SiO_x-based

hybrid film was $4.0 \pm 0.5 \times 10^{-5}$ g/m^2/day. Therefore, a 10 nm-thick Al_2O_3 film deposited by ALD was enough to seal the defects and pinholes in the SiO_x film, reducing the overall processing time. With a deposition rate of 0.5 nm/min for the Al_2O_3 layer along with a deposition rate of 33 nm/min for the SiO_x layer (3 times faster than that of SiN_x), this hybrid encapsulation architecture provides a good combination of barrier performance and reduced processing time when compared to some multilayer structures with similar permeation rates. This is afforded by utilizing the fast deposition process of PECVD and minimizing the deposition time needed for ALD, especially when the 10 nm-thick layer is used. Overall, we have observed a decrease in processing time of a factor of 5 when compared to the multilayer structure with similar effective WVTR values consisting of SiO_x/parylene which we have produced.

In considering the encapsulation of devices on flexible polymer substrates, it is necessary to seal the polymer substrate due to the high water permeation rates of many polymer substrates. To test the performance of the hybrid layers in this role, a SiO_x/ Al_2O_3/parylene layer was deposited on a 100 μm-thick polyethylene terephthalate (PET) film. A calcium sensor was then deposited on this sealed polymer substrate followed by the deposition of another hybrid encapsulation structure. This resulted in the Ca layer being sandwiched between two hybrid layers. The effective WVTR was measured to be $2.4 \pm 1.5 \times 10^{-5}$ g/m^2/day at 20 °C and 50 % R.H. which is very similar to the performance on glass substrates.

6.3.2 Activation Rate Theory

The synergistic effect from the interlayer in the hybrid structure is investigated using activated rate theory. The permeation of an ideal gas through silicon oxide[39] and glassy polymers below their glass transition temperature (T_g) can be described by an Arrhenius equation:

$$P = P_0 e^{-\Delta E_P / RT} \quad (9)$$

P, P_0 , and ΔE_P, are the permeability, pre-exponential factor, and activation energy for permeation in kJ/mol, respectively. R is the ideal gas constant in J/mol/K and T is the temperature in K. ΔE_P is a measure of the energy needed to elevate the permeant to the activated state and to distort the barrier matrix so that the permeant may move into the next vacancy.[118] Hence, by comparing the values of activation energy, which barrier layer is more tightly packed can be deduced. Also, this theory can be used to predict the temperature dependency of barrier layers.[40, 41]

The activation energy for water vapor through the hybrid layer (SiO_x/Al_2O_3/Parylene) is calculated by measuring the permeability at constant temperatures of 10, 20, 30, 40, and 50 °C in this study. Figure 6.6 shows the Arrhenius behavior of the permeation of water vapor through the hybrid barrier layer, and the value of ΔE_P was calculated to be 91.04 ± 13.17 kJ/mol. For a single layer of Al_2O_3 by ALD, values of ΔE_P in the range of 52 – 58 kJ/mol have been reported and the value of 92 kJ/mol for nano-laminated Al_2O_3/ZrO_3 fabricated by ALD was also reported.[27, 40, 41] By comparing those reported data, ΔE_P of the hybrid barrier layer shows a higher activation energy than a single Al_2O_3 layer and similar to a nano-laminated structure. This higher value of ΔE_P for the hybrid layer supports the idea that an interlayer between the Al_2O_3 and SiO_x films results in an additional rate limiting layer as illustrated in Figure 6.5 (c). The rate limiting permeation step can be interpreted as not solely a function of permeation through the Al_2O_3 layer but also a function of the interlayer. In support of this interpretation, the measured permeability of the hybrid layer is also lower than the permeability calculated using lamination theory based on the values of individual Al_2O_3 and 1 dyad of SiO_x/parylene layers as presented in section 6.3.1.

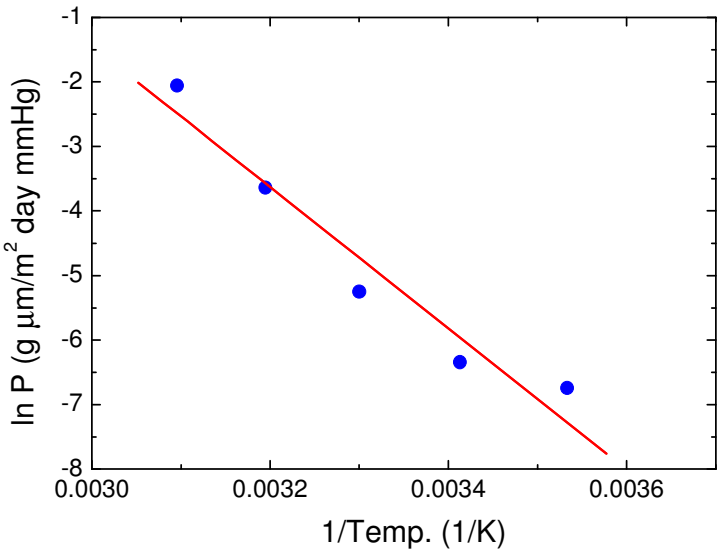

Figure 6.6 Plot of ln(P) as a function of 1/Tempareture for water and oxygen permeation through the hybrid barrier layer. Filled circles are experimental data, and the solid line is a linear fit.

6.4 Summary

The first goal of this chapter was to fabricate high performance single barrier layer having equivalent barrier performance of multilayer structure. To this end, an ALD process was employed to deposit Al_2O_3 single layer films and their barrier performance was evaluated using the Ca corrosion test. While the barrier performance of this layer shows equivalent or superior properties to that of 2 dyads of SiO_x/parylene or SiN_x/parylene, the deposition rate for ALD films is typically an order of magnitude lower than PECVD processing, resulting in very long deposition times.

The second goal of this chapter was to circumvent long processing times of ALD and propose newly developed hybrid encapsulation structures. To this end, a hybrid encapsulation structure was proposed and this structure combines the advantages of fast deposition of PECVD and high quality of ALD processing. Very thin Al_2O_3 layers which can reduce the processing time needed by ALD were deposited on either SiO_x or SiN_x

produced by PECVD to seal their defects. This structure was demonstrated to have an effective WVTR as low as $3.0 \pm 1.4 \times 10^{-5}$ g/m^2/day, which is similar to that of multilayer barrier films but with far simpler structure. This low permeation rate is expected to be originated from the interlayer between either SiO_x or SiN_x deposited by PECVD and Al_2O_3 deposited by ALD.

CHAPTER 7

MECHANICS OF THIN-FILM ENCAPSULATION

7.1 Overview

One of the unique characteristics of organic devices is their ability to be utilized in flexible electronics. To realize this, stiff glass substrate will be replaced by flexible plastic substrate such as PET or PEN. However, general plastic substrates are too permeable to water vapor and oxygen, so these substrates will be coated with barrier films. Inorganic layers used in this purpose provide the largest resistance to water vapor and oxygen, yet limit the mechanical flexibility of the encapsulation and, thus, the device lifetime. In general, fractures in the encapsulation layers cause rapid device failure due to the increased permeation rates of water vapor and oxygen through the cracks in the encapsulation. Therefore, the response of thin films under mechanical deformation should be understood, and mechanically robust encapsulation structures should be developed in order to realize flexible organic electronics.

The first goal of this chapter is to investigate mechanical properties of various thin films to understand their mechanical response under deformation. As explained in section 2.6, the geometry of the structure such as thickness and bending radius of curvature as well as mechanical properties impact the mechanical response of encapsulation structures. Hence, nanoindentation experiments were performed for the study of the modulus of the deposited thin films. Secondly, the deformation induced cracking was investigated to study mechanical limitation of both individual and combined thin-film structures. In addition, the barrier performance of multilayer structures under bending was investigated for same reason. Based on these results, it was concluded that a more flexible encapsulation structure should be developed for the

application of flexible encapsulation. Hence, the second goal of this chapter is to propose a flexible encapsulation structure. Coating the device with an epoxy layer resulted in a shift in the neutral axis for bending towards the encapsulation, reducing the induced strain. It was observed that this new structure was able to maintain barrier performance under deformation at smaller radii of curvature.

7.2 Mechanical Properties of Barrier Films

In order to investigate the mechanical behavior of thin films, the nanoindentation explained in the Chapter 3 was employed. It is very important to understand the mechanical response of thin films to address concerns about their reliability. Furthermore, the mechanical behavior of materials in the form of thin films can be quite different from those of materials in bulk form resulting in unexpected mechanical behavior.[119] Therefore, it is a necessary step to characterize the mechanical properties of thin films to understand, predict, and improve the flexibility of encapsulation containing thin films.

Nanoindentation tests on 1 μm-thick parylene layers yielded elastic modulus values of 4.3 GPa. The modulus of 100 nm-thick SiO_x and SiN_x were found to be 42.1 GPa and 87.7 GPa, respectively. These results for SiO_x and SiN_x deviate from reported values for the bulk materials. The modulus of bulk SiO_x was reported as 70 GPa, and SiN_x was in the range of 202 GPa to 307 GPa.[120] The differences in mechanical properties between thin films and bulk materials are due to micro-structural differences and surface oxidation.[121] As expected, the elastic modulus of the parylene film are far lower than those of inorganic materials such as SiO_x and SiN_x by at least an order of magnitude. Hence, in addition to the benefit of decoupling defects in inorganic layers as explained previously, a soft organic layer between inorganic layers has an important role in stress relaxation during the deposition of multilayer encapsulation structures.

7.3 Film Residual Stress and Crack On-set Strain in Barrier Films

The residual stress of SiN_x and SiO_x deposited by PECVD and Al_2O_3 by ALD were investigated. The residual stress is very important because the film stress can affect the mechanical properties and flexibility of the barrier films.[122] It was also reported that compressive residual stress in the films is beneficial to the barrier performance and adhesion.[19] However, high compressive stress can cause various problems such as buckling of the films.[122] Measured stresses of films are listed in Table 7.1, and these results prove that deposition conditions and methods can change the residual stress. Residual stress of the film is the summation of both the stress induced by the growth mechanism and the stress caused by CTE mismatch between the deposited film and substrate. Hence, total residual stress is given by [123]

$$\sigma_{total} = \sigma_{growth} + \sigma_{thermal} \tag{7.1}$$

Stress induced by CTE mismatch is written in a form as follows,[124]

$$\sigma_{thermal} = E\frac{(\alpha_f - \alpha_s)\Delta T}{\alpha_s \Delta T + 1} \tag{7.2}$$

where E is the modulus of the film, ΔT is the temperature difference, and α_s and α_f are the thermal expansion coefficient of the substrate and film, respectively. As listed in Table 7.1, both SiN_x and SiO_x deposited by PECVD have compressive stresses (negative value) due to the ion bombardment of the growing film with energetic particles induced by the plasma. Both of them have very small thermal stress because CTE mismatch between the films and substrate is insignificant as listed in Table 7.2. On the other hand, the residual stress of ALD-deposited Al_2O_3 is highly tensile (positive value) because there is no ion bombardment in the case of ALD, and CTE mismatch between substrate and Al_2O_3 cannot be neglected. Hence, thermal stress dominates the residual stress in the case of ALD-deposited Al_2O_3. This highly tensile stress can be detrimental to the flexibility of the barrier layer because the top surface of the barrier layer experiences tensile stress during inbound bending. By applying an additional layer of PECVD-deposited SiO_x,

which has compressive stress, on the Al_2O_3, the resultant film stress was measured with 28 MPa, which is very low compared to the initial stress of Al_2O_3 and more preferred for a flexible encapsulation structure.

Table 7.1 Residual stress of thin films deposited by different processes.

Deposition Method	Film	Thermal Stress (MPa)	Total Stress (MPa)
PECVD (Plasma Therm at 13.56 MHz)	SiO_x	-7.9	-196
	SiN_x	+5.5	-54
ALD (Cambridge Nano Tech.)	Al_2O_3	+148.5	+183

Table 7.2 CTE of the deposited films and substrate.

Materials	SiO_x	SiN_x	Al_2O_3	Silicon
CTE	0.5	3.3	8.1	2.6

Next, the development of cracks as a function of strain were investigated in SiO_x and SiN_x layers deposited by PECVD and in Al_2O_3 layers by ALD. All coatings were fabricated on substrates of 100 μm-thick PET coated with 1 μm-thick parylene film. Samples were bent on cylinders with different radii of curvature. Crack patterns were characterized by means of optical microscopy. Cracks started to appear at a radius of curvature of between 6.4 and 10 mm, which corresponds to a strain of 0.8 % (6.4 mm) in both SiO_x and SiN_x layers. The crack densities increase as the radius of curvature is further reduced (see Figure 7.1 (a)-(c)). The strain of the top surface of film is calculated by using equation (2.14) which was introduced in Chapter 2.5.

In this experiment, Young's moduli measured for PET and parylene of 3.0 GPa and 4.3 GPa, respectively, were used. In principle, a more complicated equation should be used in this calculation. However, it can be assumed that PET and parylene are the same materials because the modulus is almost same. Hence, the neutral axis shifts toward PET substrate, and the top surface experiences less tensile stress compared to a

uniform material with same thickness. Cracks appear in the films for strains greater than or equal to 0.8 % for a 6.4 mm bending radius of curvature, and this is supported by other references.[53, 83] Typical crack onset strains of brittle films are reported as 0.5-2.5 %.[53, 83] The reason why these reported data are different is because the properties of fabricated films can vary stochastically according to the processing and substrate conditions. In the films of Al_2O_3, parallel and branched cracks appear, as shown in Figure 7.1 (d). The highly tensile stress of Al_2O_3 is expected to induce these many branched cracks. It should be noted that highly tensile residual stresses in deposited films are more detrimental to the barrier performance of films under mechanical deformation. Thus, it is imperative to consider both the residual stress state and barrier properties when designing and developing encapsulation layers for flexible devices.

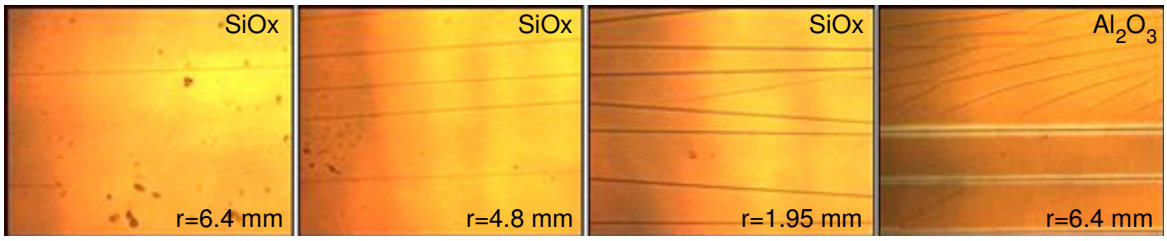

Figure 7.1 Optical micrographs show the crack pattern and density in SiO_x (a) - (c) samples bent to different radii of curvature. In image (d) on Al_2O_3, there are many branched cracks (R = 6.4 mm), which suggest that the tensile stresses in the film provide additional driving force for crack propagation and damage in the film.

7.4 Barrier Performance under Mechanical Deformation

In order to investigate the barrier performance of encapsulation barriers under mechanical deformation, bending tests were performed in the same way as the crack density measurements on encapsulated Ca sensors, as shown in Figure 7.2. In this experiment, Ca sensors were fabricated on electrically insulated 50 μm-thick stainless steel substrate. Stainless steel substrates were used because they are flexible and impermeable to water vapor and oxygen. However, the surface of the stainless steel is

too rough for the deposition of thin Ca and Al layers (100-300 nm), so chemical and mechanical polishing (CMP) was used to smooth the surface of the substrates before the deposition of insulating films. Also, both parylene and PECVD deposited SiN_x were used as insulating layers between the Ca sensors and the stainless steel substrates as shown in the Figure 7.2 (a). The Ca sensors and Al electrodes were deposited on top of the insulation layer, and finally, encapsulation layers of 3 dyads of SiN_x/parylene or SiO_x/parylene were deposited on the Ca sensors. The encapsulated Ca sensors on stainless steel were bent at fixed radii of curvature between 6.4 – 29 mm as shown in the Figure 7.2 (b) in order to investigate the barrier performance under bending conditions.

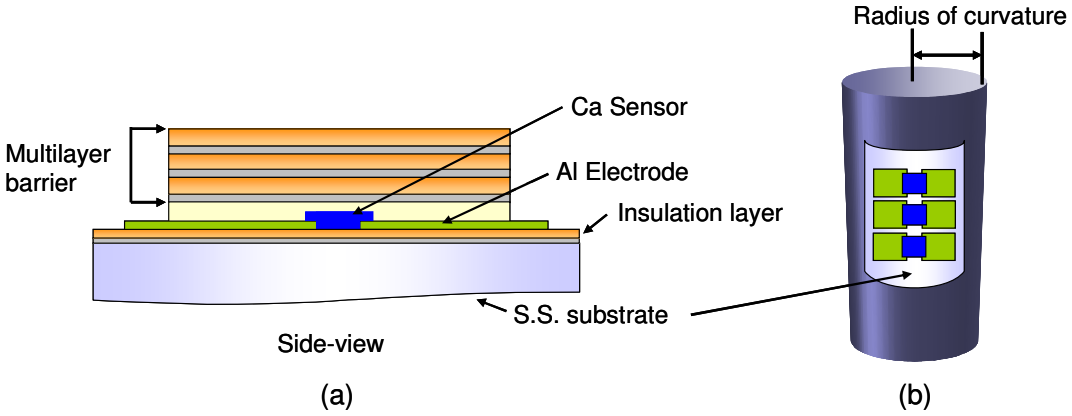

Figure 7.2 Schematic describes (a) the side view of encapsulated Ca on an electrically insulated stainless steel substrate. Encapsulated Ca sensors were bent on a cylinder at a fixed radius of curvature (b).

The results in the Table 7.3 show that the effective WVTR as a function of the radius of curvature. The barrier performance appears to be constant down to a radius of curvature of 10 mm, after which a drastic increase in WVTR is observed for both structures. These data suggests that damages in SiO_x/parylene and SiN_x/parylene layers were initiated between 6 mm and 10 mm radii of curvature. Previous results about cracking development with bending (6.4 mm radius of curvature) of SiO_x and SiN_x are also supported by the effective WVTR measurement experiments performed under bending. This effective WVTR experiment under bending suggests that crack onset

strain is very important because multilayer encapsulation layers lose their barrier performance immediately after crack initiation regardless of the number of cracks. This experiment shows that the flexibility of the encapsulation structure is not sufficient for the realization of highly flexible organic electronics. Therefore, a new encapsulation structure is proposed in the next section.

Table 7.3 Effective WVTR of 3 dyads of SiO_x/parylene and SiN_x/parylene as a function of radius curvature.

Radius of curvature (mm) [Strain (%)]		29 [0.2]	13 [0.4]	9.5 [0.6]	6.4 [0.9]
Effective WVTR ($g/m^2/day$)	SiO_X/ parylene	$1.3 \pm 0.6 \times 10^{-3}$	$1.1 \pm 0.2 \times 10^{-4}$	$9.3 \pm 0.9 \times 10^{-3}$	Rapid oxidation [a]
	SiN_X/ parylene	$3.1 \pm 0.6 \times 10^{-4}$	$8.5 \pm 1.9 \times 10^{-4}$	$2.3 \pm 1.7 \times 10^{-4}$	Rapid oxidation [a]

[a] Ca was oxidized through cracks in the encapsulation, so effective WVTR cannot be calculated

7.5 Highly Flexible Encapsulation Structure

As introduced in section 2.6 the flexibility of an encapsulation layer can be improved by placing the brittle barrier layer on or close to the neutral axis because there is neither compressive nor tensile stress along the neutral axis as described in the Figure 7.3 (a). While the top and bottom surfaces experience tensile and compressive stress, respectively, these materials are very soft compared to the inorganic barrier layer resulting in no cracks from the bending.

In order to demonstrate the effectiveness of placing the barrier layer on the neutral axis, a hybrid barrier layer was employed on a PET substrate because PET itself is too permeable to water and oxygen. A hybrid-coated PET substrate was shown in the previous chapter to provide enough high barrier performance to replace the stainless steel substrate. However, it was also found that the hybrid layer lost its barrier performance when it was bent at a radius of curvature of 6.4 mm, which produced a tensile strain of 0.8 % in the hybrid layer. Optical micrographs in Figure 2.17 show that Ca is oxidized

by reaction with water that permeated through cracks. Therefore, this study stresses that the neutral axis should be placed close to the hybrid layer to prevent these cracks. After sealing PET with a hybrid layer, Ca sensors and Al electrodes were deposited on the coated PET followed by deposition of another hybrid layer. Consequently, the Ca sensors were sandwiched between two identical hybrid layers. In order to shift the neutral axis to the hybrid layer, a layer of parylene was deposited on the hybrid layer to match the 100 μm-thick PET substrate, which was used for easy handling. The thickness of the deposited parylene was determined based upon following equation:

$$Y_1 d_1^2 = Y_2 d_2^2 \tag{7.4}$$

where Y_1 and d_1 and Y_2 and d_2 are the modulus and thickness of the PET and parylene, respectively. As a result, the Ca sensor and hybrid barrier layer can be located on or close to the neutral axis resulting in no or less strain induced by bending.

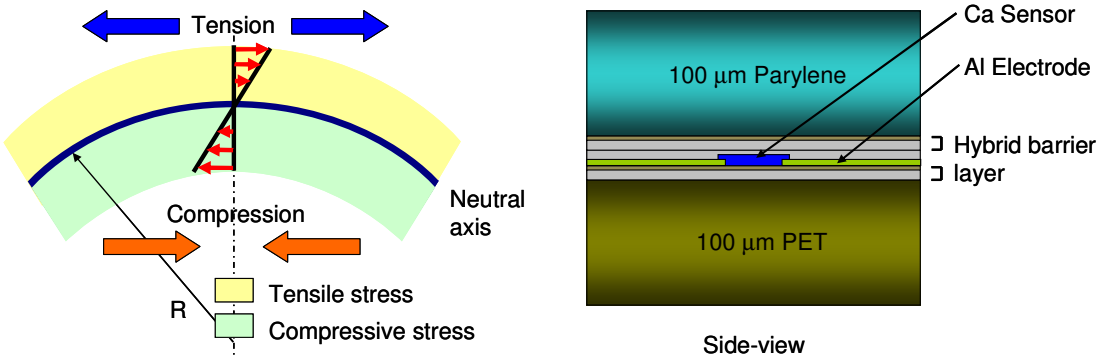

Figure 7.3 Schematic (a) shows the compressive and tensile stress when the structure is bent. While the top surface relative to the neutral axis experiences highly tensile stress, the bottom surface experiences compressive stress. Consequently, the neutral axis experiences no stress from bending. Schematic (b) shows the highly flexible encapsulation structure. Hybrid barrier layers and a Ca sensor are sandwiched between two polymer layers.

This structure was expected to be able to encapsulate organic devices with high barrier performance as well as highly flexibility. However, delamination between

parylene and the top layer of the hybrid structure occurred during bending because the adhesion between the two layers is less of a chemical bonding than a mechanical adhesion. Although adhesion can be improved by applying an adhesion agent between the parylene and hybrid layer, this approach would require one additional process step. Therefore, epoxy deposited by spin-coating was used instead of parylene because of its good adhesion properties. While epoxy is more hydrophilic compared to parylene, most of the resistance against water and oxygen comes from the inorganic layer. Replacing parylene with epoxy does not affect the overall barrier performance of the hybrid layer. The modulus of cured epoxy was measured to be 4.6 GPa, which is comparable to that of the PET substrate,[125] and the thickness was determined based upon Equation (7.4).

As discussed previously, encapsulated Ca sensors with an epoxy sealant were bent at a radius of curvature of 6.4 mm, and the barrier performance was investigated under bending in a controlled environmental chamber. By placing the brittle barrier layer close to the neutral axis, the encapsulation structure sustains its barrier performance under bending. In order to visually observe the effectiveness of this structure, GT logos printed paper were wrapped around the cylinder underneath the encapsulated Ca sensors. The oxidation of the encapsulated Ca can be seen because the Ca becomes transparent after oxidation, revealing the GT logos underneath. In Figure 7.4, the top three samples are encapsulated without a top layer of epoxy resulting in tensile stress on the hybrid layer. The bottom three samples have an epoxy top layer resulting in reduced stress on the hybrid layer due to the shift of neutral axis to the hybrid layer. After 2 days, the GT logos can be clearly seen in the case of encapsulation without an additional epoxy coating (top samples) due to water permeation through cracks, while the Ca sensor is still opaque in the case of encapsulation with an epoxy coating (bottom samples). Consequently, this demonstrates that the encapsulation structure developed for high flexibility does sustain its barrier performance when bent to a small radius of curvature. This result is very promising for the future development of highly flexible organic electronics.

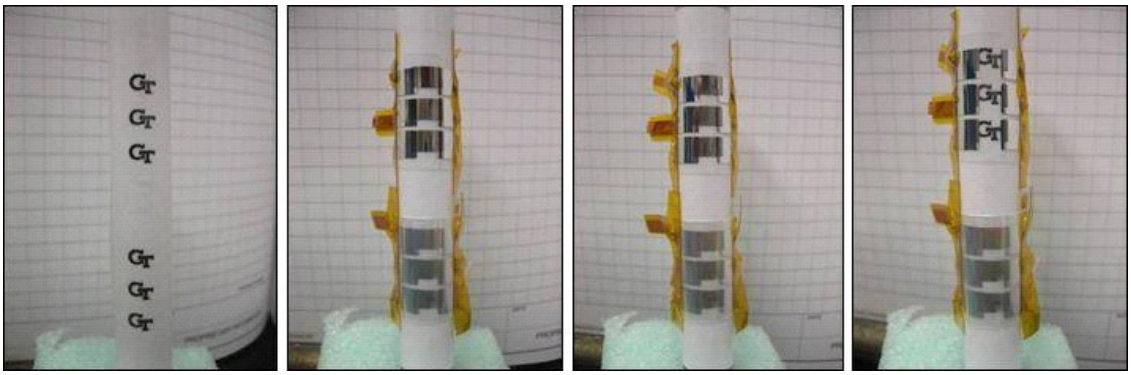

Figure 7.4 Picture (a) shows GT logos wrapped around the cylinder for visual inspection. In pictures (b) ~ (d), the top three Ca sensors are encapsulated without a top epoxy coating and the bottom three are with a top epoxy coating; (b) after bending, (c) after 10 min, (d) after 2 days.

7.6 Summary

The first goal of this chapter was to investigate mechanical response of various thin films. To this end, nanoindentation was employed and the modulus of films and substrates were investigated. Also, cracking development as a function of strain for single inorganic films and hybrid structure was investigated using optical microcopy and results show that cracks developed for strains greater than ~ 0.8 % of strain in most inorganic films. This result was also verified by measuring the barrier performance of multilayer encapsulation under bending. This mechanical limitation of encapsulation layer corresponds to that of organic electronics because fractures in the encapsulation layers cause rapid device failure due to the increased permeation rates of water vapor and oxygen.

Overcoming the mechanical limitations of encapsulation layers was the second goal of this chapter. To this end, hybrid layers were coated on a PET substrate and additional hybrid layers combined with epoxy were applied on top of Ca censors. This structure leads in a shift of the neutral surface toward the barrier layer resulting in

reduced strain. This experiment demonstrates high barrier performance as well as high flexibility. However, additional testing should be performed to investigate long term stability of this structure by applying repeated bending.

CHAPTER 8

INTEGRATION OF ENCAPSULATION WITH ORGANIC SOLAR CELLS

8.1 Overview

In this chapter, the encapsulation layers that were developed and characterized in chapter 4 and 6 are integrated with organic solar cells to validate their effectiveness as barrier layers. Annealed SiN_x/parylene multilayer structures with 1 to 3 dyads and hybrid structures using either SiO_x or SiN_x were integrated with organic solar cells in this study. By encapsulating organic solar cells with these fully characterized encapsulation layers, it is possible to obtain a one to one correlation between the barrier performance and the shelf-lifetime of encapsulated organic solar cells. Therefore, the main goal of this chapter is to evaluate the effectiveness of developed barrier layers by presenting the performance parameters of encapsulated organic device as a function of exposure time. The device geometry used in this study was explained in section 3.5. The compatibility of encapsulation with organic solar cells was investigated by comparing the device performance parameter before and after encapsulation. The device performance parameters were measured periodically and results are presented in this chapter.

8.2 Process Compatibility with Organic Solar Cells

The first concern when encapsulating organic devices is whether the processing of the thin-film encapsulation impacts the performance of the organic devices. In this study, two types of encapsulation structures were studied. One is a multilayer structure and the other is a hybrid structure. For both encapsulation structures, a SiO_x interlayer deposited by PECVD at 110 °C is the first layer to contact the devices. After fabrication of the

SiO_x interlayer, encapsulation continues with repeated processes of parylene CVD at room temperature and PECVD at 110 °C in the case of the multilayer structure, or one process each of ALD at 110 °C and parylene CVD at room temperature in the case of the hybrid encapsulation structure.

Table 8.1 Performance parameters of solar cells before and after encapsulation with a multilayer structure. For each type of encapsulation, the data is averaged over 3 devices.

No. of layers (SiN_x/parylene)	Before encapsulation			
	η (%)	J_{SC} (mA/cm^2)	*FF*	V_{OC} (mV)
0 dyad	3.2 ± 0.0	11.6 ± 0.3	0.54 ± 0.01	387 ± 1
1 dyads	3.2 ± 0.0	11.6 ± 0.1	0.53 ± 0.01	385 ± 2
2 dyads	3.5 ± 0.1	12.7 ± 0.4	0.55 ± 0.01	399 ± 3
3 dyads	3.2 ± 0.1	11.9 ± 0.4	0.53 ± 0.01	385 ± 1
Average	3.4 ± 0.2	12.0 ± 0.7	0.54 ± 0.03	390 ± 4

No. of layers (SiN_x/parylene)	After encapsulation			
	η (%)	J_{SC} (mA/cm^2)	*FF*	V_{OC} (mV)
0 dyad	NA	NA	NA	NA
1 dyad	3.3 ± 0.0	11.1 ± 0.1	0.49 ± 0.01	407 ± 2
2 dyads	3.5 ± 0.1	11.8 ± 0.1	0.53 ± 0.01	410 ± 5
3 dyads	3.1 ± 0.1	11.1 ± 0.1	0.49 ± 0.01	408 ± 4
Average	3.3 ± 0.2	11.4 ± 0.5	0.52 ± 0.02	412 ± 7

First, the main performance parameters of devices with multilayer encapsulation were compared before and after the encapsulation process, and the parameters are summarized in Table 8.1. These main performance parameters were extracted from the current density (*J*) - voltage (*V*) curves which are plotted in Figure 8.1 for SiN_x/parylene encapsulation with 1 – 3 dyads. The *J-V* curves were measured with a Keithley source meter unit under a broadband Xeon lamp (ASB-XE-175EX, CVI). The data in Table 8.1 and Figure 8.1 show the thermal annealing effect that has been reported in other references after encapsulation due to the PECVD process at an elevated temperature (110 °C).[63] This thermal annealing effect results in a small shift up in open-circuit voltage and a reduction in the diode reverse saturation current density as shown in the Figure 8.1.

However, efficiency averaged over 9 devices does not change significantly, indicating no strong negative impact. These results show that the multilayer encapsulation process does not harm pentacene/C_{60}-based organic solar cells and is therefore compatible with these devices.

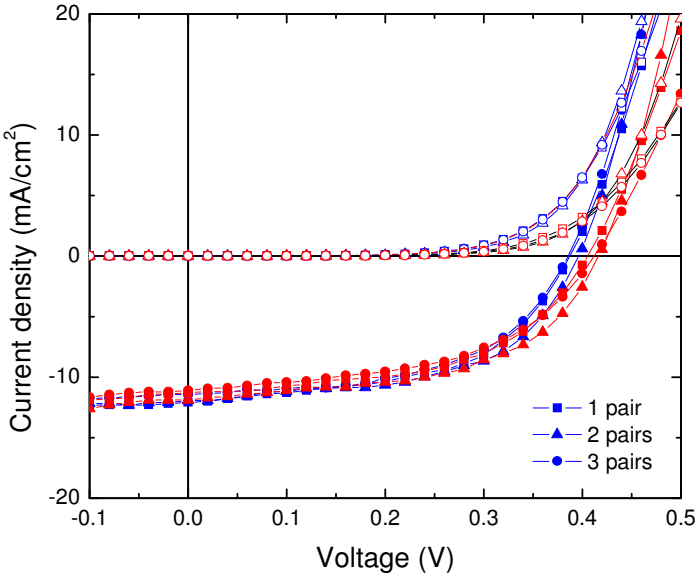

Figure 8.1 Electrical characteristics measured in the dark (empty shapes) and under illumination (filled shapes) for the same pentacene / C_{60}-based solar cells before (blue shapes) and after (red shapes) deposition of a multilayer consisting of 1 ~ 3 dyads of annealed SiN_x/parylene.

Secondly, the compatibility of the hybrid encapsulation process with pentacene/ C_{60}-based organic solar cells was investigated in same way as the multilayer encapsulation process. While the total number of process steps are reduced in the case of the hybrid structure compared to the multilayer structure, the processing time at elevated temperature is longer than that of the multilayer due to the long processing time with ALD. The main performance parameters before and after encapsulation are summarized in Table 8.2, and *J-V* curves are plotted in Figure 8.2 for both SiO_x and SiN_x based hybrid structures. The main performance parameters were not changed significantly, but

thermal annealing effects were also observed as expected. All data clearly show the devices suffered no significant damage due to the hybrid encapsulation process.

Table 8.2 Performance parameters of solar cells before and after encapsulation with a hybrid structure. For each type of encapsulation, the data is averaged over 3 devices.

No. of layers (SiN_x/parylene)	Before encapsulation			
	η (%)	J_{SC} (mA/cm^2)	FF	V_{OC} (mV)
w/o encapsulation	3.2 ± 0.0	11.6 ± 0.3	0.54 ± 0.01	387 ± 1
SiO_x/ Al_2O_3/P	3.2 ± 0.0	10.4 ± 0.0	0.56 ± 0.01	392 ± 2
SiN_x/ Al_2O_3/P	3.1 ± 0.1	10.4 ± 0.2	0.55 ± 0.01	394 ± 2
Average	3.2 ± 0.1	10.8 ± 0.4	0.55 ± 0.01	391 ± 3

No. of layers (SiN_x/parylene)	After encapsulation			
	η (%)	J_{SC} (mA/cm^2)	FF	V_{OC} (mV)
w/o encapsulation	NA	NA	NA	NA
SiO_x/ Al_2O_3/P	3.3± 0.1	9.8 ± 0.1	0.53 ± 0.02	448 ± 2
SiN_x/Al_2O_3/P	3.5 ± 0.0	9.2 ± 1.0	0.54 ± 0.01	450 ± 7
Average	3.4 ± 0.1	9.5 ± 0.1	0.53 ± 0.01	449 ± 7

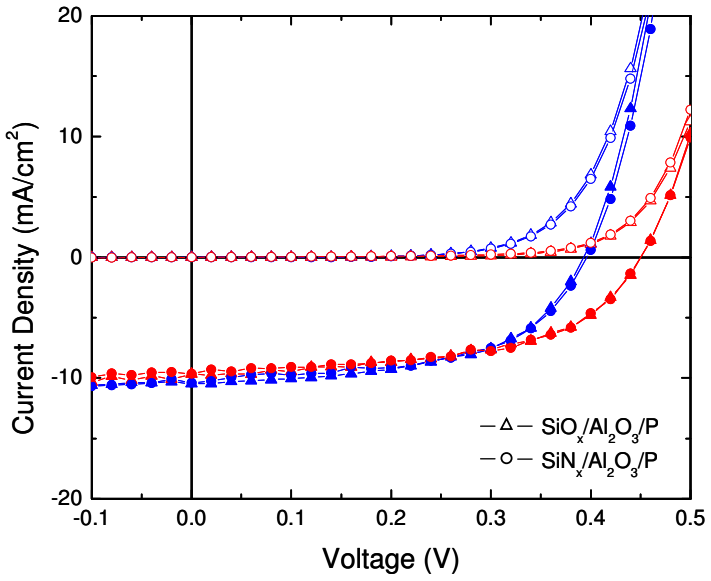

Figure 8.2 Electrical characteristics measured in the dark (empty shapes) and under illumination (filled shapes) for the same pentacene/C_{60}-based solar cells before (blue

shapes) and after (red shapes) deposition of a hybrid layer of SiO_x/Al_2O_3/parylene (triangles) or SiN_x/Al_2O_3/parylene (circles).

In conclusion, both the multilayer and hybrid encapsulation processes do not affect the performance of pentacene/C_{60}-based organic solar cells significantly based upon the comparison of the main performance parameters before and after the encapsulation process. While thermal annealing effects were observed in both cases in this study as previously reported, these did not deteriorate the performance of the encapsulated organic solar cells. Therefore, the compatibility of the encapsulation process with pentacene/C_{60}-based organic solar cells was verified. It is believed that this process is compatible with other organic devices that have a similar glass transition temperature.

8.3 Shelf-Lifetime Study of Encapsulated Organic Solar Cells

8.3.1 Multilayer Encapsulation

After the verification of the compatibility of the encapsulation processes with organic solar cells, the effectiveness of the multilayer structures as an encapsulation layer was investigated over a long period of time. Fully characterized encapsulation structures consisting of alternating SiN_x/parylene layers were integrated with pentacene/C_{60}-based organic solar cells. Structures with 1 to 3 dyads were tested to study the correlation between the barrier performance in terms of the effective WVTR and the shelf-lifetime of encapsulated solar cells. Encapsulated organic solar cells were stored in a controlled environmental chamber with the same environmental conditions as during the Ca corrosion tests (20 °C and 50 % R.H.). Main performance parameters were extracted from the *J-V* curves as done in section 8.2. The *J-V* curves were measured periodically with a Keithley source meter unit in the lab environment under a solar simulator (91169, Oriel) to investigate device degradation as a function of time.

Figure 8.3 displays the change in the normalized power conversion efficiency of the organic solar cells encapsulated with 1 to 3 dyads of SiN_x/paryelene versus exposure time. The data in Figure 8.5 show a clear trend of improving shelf-lifetime of encapsulated pentacene/C_{60}-based organic solar cells with an increasing number of SiN_x/parylene dyads. As generally expected in organic devices, un-encapsulated organic solar cells in the environmental chamber degraded very fast. The values of η dropped to less than 20 % of their initial values within 50 h, and the cells stopped generating power completely after 200 h. This fast degradation of the un-encapsulated solar cells stresses the importance of encapsulation for the practical application of organic solar cells. In the case of the 1 dyad SiN_x/parylene encapsulation structure, normalized η decreases by 50 % after ~1,000 h. While the shelf-lifetime of the device encapsulated with 1 dyad of SiN_x/parylene is longer compared to that of un-encapsulated device, the improved shelf-lifetime is still too short for most actual applications. As the number of encapsulation dyads is increased, the shelf-lifetime improves. For the samples encapsulated with 3 dyads of SiN_x/parylene, less than 10 % degradation in the device performance was observed within the first 7,000 h as seen in Figure 7. This encapsulation architecture yields an effective WVTR of $7.3 \pm 5.0 \times 10^{-6}$ g/m^2/day as measured. Considering the current results, encapsulation layers with barrier performance on the order of or less than 10^{-5} g/m^2/day are thought to block oxygen and water vapor effectively for organic solar cells consisting of pentacene and C_{60}.

It should be noted that devices might start to degrade during the multilayer encapsulation process, especially during the parylene CVD process due to its long processing in relatively weak vacuum condition. Additional degradation can occur during transport of the devices from one process to another. Ca corrosion tests cannot account for this degradation because the Ca corrosion test only reflects the conductance measurement after the encapsulation process. One solution is to use a moisture and oxygen getter like CaO that can remove permeated water vapor and oxygen during the

encapsulation process.[19] Furthermore, in-line processing of the device from device fabrication through encapsulation can reduce the chances for degradation during the encapsulation process. Degradation during the encapsulation process can be especially detrimental because the devices are not fully encapsulated yet.

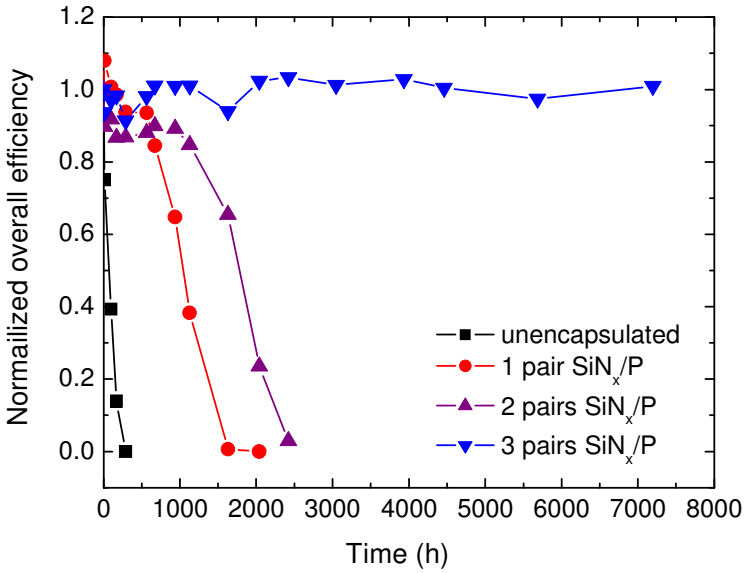

Figure 8.3 Normalized efficiency as a function of exposure time for pentacene/C_{60}-based organic solar cells encapsulated with 1 to 3 dyads of annealed SiN_x/parylene including an un-encapsulated device as a reference. Clear trends between the number of encapsulation layers and the shelf-lifetime are observed.

In conclusion, the shelf-lifetime of over 7000 h with 3 dyads of annealed SiN_x/parylene encapsulation and the one-to-one correlation between the barrier performance and the shelf-lifetime of the encapsulated organic solar cells achieved in this study represent a fundamental step towards the further improvement of the shelf-lifetime of encapsulated organic solar cells.

8.3.2 Hybrid Encapsulation

A second shelf-lifetime study of encapsulated organic solar cells was performed with the hybrid encapsulation structure. As explained in Chapter 6, the hybrid structure

combines the advantages of the high quality of ALD and the fast processing of PECVD and yielded an effective WVTR on the order of 10^{-5} g/m^2/day. The compatibility of the hybrid encapsulation process with pentacene/C_{60}-based solar cells was already verified in the previous section. In order to investigate the effectiveness of the hybrid structure as a barrier layer for organic devices, both SiN_x and SiO_x based hybrid structures were integrated with pentacene/C_{60}-based organic solar cells. Encapsulated organic solar cells were stored in a controlled environmental chamber with the same environmental conditions as during the Ca corrosion tests (20 °C and 50 % R.H.).

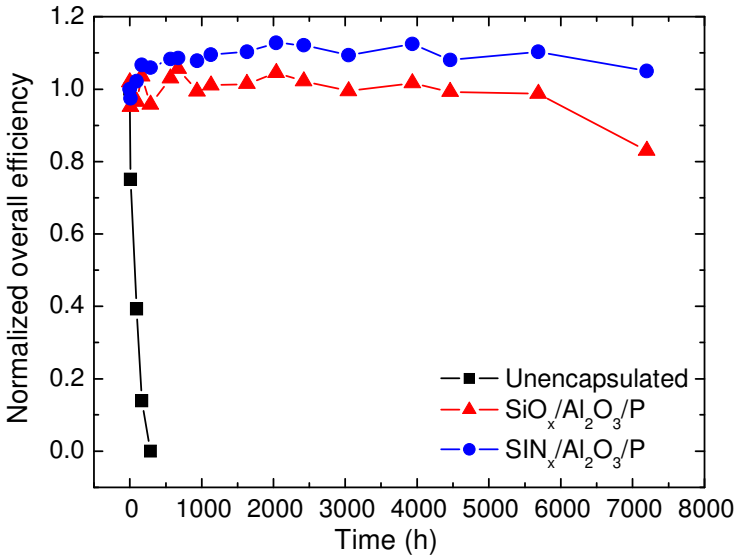

Figure 8.4 Normalized efficiency as a function of exposure time for pentacene/C_{60}-based organic solar cells encapsulated with hybrid structures consisting of either 100 nm of SiO_x or SiN_x, 50 nm of Al_2O_3, and 1 µm of parylene as a protecting layer. No degradation was observed for up to 6000 h in both cases.

The data in Figure 8.4 show the evolution of the normalized power conversion efficiency η versus exposure time for both SiN_x and SiO_x based hybrid encapsulation structures. The structure was the same as those which were tested in Chapter 4, and the effective WVTRs are 2.3 ± 1.5 × 10^{-5} g/m^2/day and 3.0 ± 1.4 × 10^{-5} g/m^2/day at 20 °C

and 50 % RH for SiO_x and SiN_x based structures, respectively. Even after 6000 h, the normalized η still remain the same compared to initial values for both structures.

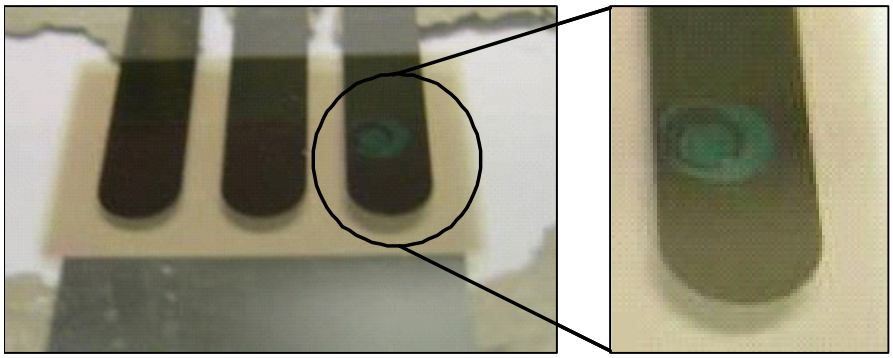

Figure 8.5 Optical images taken after 7300 h show the delamination of the device on the right encapsulated with the SiO_x-based hybrid layer.

The results in the Figure 8.4 indicates that encapsulated devices with the SiO_x-based hybrid layer started to degrade after 7000 h, while those encapsulated with the SiN_x-based hybrid layer still showed no degradation. This degradation is due to the permeation of water vapor through a defect in the hybrid layer. At the beginning of the test, the permeation of water vapor through the defect was not significant enough to affect device performance. However, permeated water vapor into the defect eventually induced a device degradation and volume expansion of the thin films simultaneously after long exposure to ambient air. Pictures in Figure 8.5 show the partial delamination of the constituent films in the device on the right. It led to delamination between films with weak adhesion and catastrophic failure. Hence, this finding emphasizes that even few defects during the encapsulation process can be detrimental to the long-term reliability of encapsulated organic devices.

In conclusion, improved shelf-lifetime of devices encapsulated with hybrid layer is thought to be caused by the Al_2O_3 layer more effectively preventing the permeation of water vapor and oxygen through hybrid layer structure. Shorter processing time of the hybrid structure compared to the multilayer structure might contribute to the extended shelf-lifetime because this can reduce the degradation during the fabrication of the encapsulation. Furthermore, there is less chance for the side permeation of water vapor

and oxygen through the organic layer because a parylene organic layer was used only for the top protective layer. While further shelf-lifetime experiments will have to be performed over longer periods of time and in harsher conditions, the results obtained so far with the hybrid structures are very promising for the realization of long-lived organic solar cells encapsulated with thin films deposited directly on the devices. The use of these hybrid structures represents a critical first step towards achieving lifetimes of 3-5 years, which are expected to be necessary for the commercialization of organic solar cells.

8.4 Summary

The main goal of this chapter was to evaluate the effectiveness of developed barrier layers. To this end, pentacene/C_{60}-based based organic solar cells were used in this study and encapsulated with hybrid layer and multilayer with known effective WVTR. The compatibility and effectiveness of both encapsulation structures were successfully validated on pentacene/C_{60}-based organic solar cells.

In the case of multilayer encapsulation, the devices shelf-lifetimes of over 2,000 h can be achieved by encapsulating with barrier films that have effective WVTRs on the order of 10^{-4} g/m^2/day. For over 7,000 h of shelf-lifetime in organic devices, a barrier layer with a WVTR of 10^{-6} g m^{-2} day^{-1} is required based upon our results. Hybrid encapsulation structures based on both SiO_x/Al_2O_3 and SiN_x/Al_2O_3 provide over 7,000 h shelf-lifetime of organic devices. These results show that encapsulation films with effective WVTRs on the order of 10^{-5} g/m^2/day are sufficient for protecting the shelf-lifetime of pentacene/C_{60}-based solar cells. However, while this work provides the correlation between the effective WVTR of barrier layers and shelf-lifetime of encapsulated organic devices, no test has been performed in harsh condition such as at high temperature, high humidity, and under solar irradiation. Hence, it is strongly suggested for encapsulated organic device to be tested in harsh condition, thereby

providing reliable protection for organic devices which are used under insolation with solar energy with further research.

CHAPTER 9

CONCLUSIONS AND OUTLOOK

Thin-film encapsulation is a critical technology for the commercialization of flexible organic electronics. Effective encapsulation to prevent the permeation of water vapor and oxygen, which degrade organic devices, is a key for achieving the lifetime required for most applications. The main research contributions of this dissertation were providing a systematical study exploring the parameters which impact both multilayer and single-layer encapsulation films and their integration with organic electronic devices. Through the efforts of this work, we were able to establish the importance of defects in determining the overall film barrier performance and through this, created a new hybrid layer barrier film. This new film effectively provides an ultra higher barrier performance film with a simplified architecture by treating the defects which commonly exist in low temperature vacuum deposited inorganic materials. Analytical simulations of the permeation through encapsulation films provided the basic understanding for the permeation mechanism of water vapor and the critical guidelines for designing efficient barrier layers. Comparisons to both WVTR and lag time measurements in films elucidate the role of the diffusion coefficient, solubility, and defects in the barrier layer performance. Overall, such analytical modeling provides a tool to understand how the manipulation of barrier film architecture can impact the overall performance the encapsulation. Additional studies of the mechanical behavior of thin films enable the development of highly flexible encapsulation structures by controlling the position of the neutral axis within the device architecture. Such concepts are important for extending the flexibility of the device while maintaining good barrier performance. The following are important findings of this dissertation and insight gained from those findings which are

summarized by chapter. Furthermore, based on current results of this dissertation, future work to address outstanding research issues is suggested.

In Chapter 4, the experimental results of multilayer encapsulation architectures including a comprehensive study of the water vapor permeation through various films are presented. SiN_x/parylene and SiO_x/parylene dyads were fabricated, and the barrier performance was investigated to correlate it with the number of dyads. This study is one of the first to show the strong correlation between the number of dyads and the barrier performance and diminishing effect of improvement in the barrier performance after 4 dyads. This diminishing effect suggests that there should be a limitation in improving barrier performance of multilayer structure by simply adding dyad. Instead of increasing the number of dyad, the development of high quality film is critical to improve the overall barrier performance of multilayer structures. In addition, the results concerning the improvement of barrier performance by annealing parylene layers were presented. Parylene annealing provided a smoother surface helping in producing a subsequent inorganic layer with higher quality. This finding also supports that the quality of inorganic layer is dominant factor in determining the barrier performance of multilayer structure. In addition, it should be worth trying to find other organic layers which can reduce processing time and provide smoother surface for subsequent inorganic layer deposition and investigating its impact on the overall barrier performance.

Based on the results of Chapter 4, an analytical simulation study was undertaken in Chapter 5 to investigate how individual properties of constituent films impact on the overall barrier performance. By comparing analytical simulation results with experimental results from Ca corrosion test, the expected range of permeation properties, such as the diffusion and solubility coefficients of individual films were determined. Permeation properties of inorganic film are dominant in determining the permeation rate in the steady state region as well as lag time. In addition, this result provides that lag time can be further increased up to several years, which can be longer than required

lifetime of organic devices. This lag time is dependent on the permeation properties of constituent films as well as on the effective length of permeation path through organic layer, which is directly related to the defect spacing in the case of multilayer encapsulation structure. Hence, it was concluded that lowering the steady-state permeation rate as well as increasing the lag time is critical to extending the shelf-lifetime of encapsulated organic devices. However, very little attention is given to engineering in a lag time effect. Future work should consider the use of desiccant layers which improve lag time effects. Layers such as TiO_x or other materials can be easily integrated into the films to give such behavior.

Chapter 6 presents the results of single-layer and hybrid-layer encapsulation structures. While single film fabricated by ALD as a barrier layer has advantage in high barrier performance with simple process step and structure, long processing times makes it difficult to be adapted widely. A hybrid encapsulation structure, which combines the advantages of single and multilayer structures, was proposed, developed and tested. This structure showed promising results due to its high quality barrier performance as well as its simpler structure compared to that of multilayer encapsulation. Defects in films quickly deposited by PECVD are well passivated by an ultra-thin layer deposited by ALD. A synergistic effect from combining PECVD and ALD was found by applying lamination theory and verified by comparing activation energy with those of current results.

While this contribution of creating a hybrid-layer encapsulation was deemed a successful approach, more work must be done to fully capture the effects of the hybrid approach. First, detailed experiments should be performed to investigate the cross-section of interlayer between the ALD deposited film and PECVD deposited film by using TEM. Also, the approach of defect filling using ALD can be expanded to other techniques such as Pulsed PECVD. Pulsed PECVD is known to deposit higher quality films and would render the approach a single chamber deposition method, simplifying the

processing even further. Also, techniques such as Plasma ALD being developed should be considered as they increase the deposition of ALD while maintain excellent film quality. In general, additional processing methods which can exploit rapid defect filling must be investigated.

In Chapter 7, the mechanical response of thin films was investigated by using nanoindentation and the wafer curvature method for the measurement of modulus and residual stress, respectively. The crack behavior of various thin films under tensile stress was investigated, and cracks were found at a radius of curvature of 6.4 mm, which corresponds to a strain of 0.8 % in both SiO_x, SiN_x, and hybrid layers. In order to improve the mechanical limitations of brittle inorganic layers, which should be utilized to satisfy the stringent requirements on barrier performance, a novel approach for highly flexible encapsulation structures was proposed. By placing the brittle barrier layer close to the neutral axis using an additional epoxy layer with suitable thickness, the encapsulation structure can sustain its barrier performance under bending smaller radii of curvature due to the reduction in strain on the films. This effect was demonstrated experimentally in this Chapter 7. For actual application of this structure, long-term stability and fatigue tests of the proposed structure under repeated bending should be performed.

The effectiveness of developed hybrid and multilayer encapsulation structures which were characterized in Chapters 4 and 6 were verified by encapsulating organic devices in the Chapter 8. The compatibility of the encapsulation processes with organic devices was investigated by comparing device performance parameters before and after encapsulation. Encapsulated organic devices were stored at constant conditions and their performance parameters were measured periodically for comparison with their initial values. Both multilayer encapsulation with 3 dyads of SiN_x/parylene and hybrid encapsulation provided over 7,000 h of shelf-lifetime. Therefore, it was concluded that 10^{-5} g/m^2/day is a minimum requirement for barrier performance for at least 7,000 h of

shelf-lifetime in pentacene/C_{60}-based organic solar cells. In addition, reported shelf-lifetime of encapsulated organic device can be further improved by applying inline processing. Organic devices start degrading during the encapsulation due to the exposure to air during processing and transferring from one process to another. This degradation can be prevented using inline processing without exposure to the air. This process also can reduce the barrier failure caused by particle contamination which can occur during transferring organic devices. Additional work should also consider barrier performance at high temperatures and humidity (65°C and 85% RH). Also, barrier performance under UV or AM 1.5 illumination must be addressed for application to solar cells.

The primary advantage of plastic organic electronics is their ability to produce lightweight, mechanically flexible, and dimensionally large electronics at low manufacturing cost. However, many challenges still remain before the paradigm shift in electronics from conventional silicon based electronics to plastic organic electronics can be fully realized, including developing fabrication processes, increasing device performance, and improving reliability. In the area of reliability, more thin-film encapsulation technologies must be developed that can provide adequate barrier performance while being compatible with the unique properties of plastic electronics. More fundamental studies behind barrier layers such as water vapor diffusion, which shows non-ideal gas behavior through the various films and interaction with water vapor resulting in changing properties of barrier films, and its impact on the performance of organic devices should be investigated extensively. In addition to the application with organic solar cells, developed thin-film barrier layers can be applied in encapsulating other organic electronic devices such as OLED and OTFT. Hence, further study concerning the compatibility and the effectiveness of barrier layers with these devices should be a future research area. Furthermore, it is very important to consider optical effects created by barrier layers. Transparency of barrier layers is a major consideration for the application of displays, lightings, and solar cells because it directly influences the

efficiency of these devices. Yoshida et al. used silicon oxynitride (SiON) for the encapsulation of OELD and changed the oxygen-density ratio (O/O + N) in order to improve the transparency (> 90 %).[126] Therefore, those efforts should be combined with improvement in the barrier performance and mechanical flexibility for fully exploiting advantages of thin-film encapsulation.

Regarding the commercialization of organic electronics, manufacturers demand increased line speeds and reduced material consumption in thin-film barrier processing. Hence, based on the current results using widely adapted deposition techniques in this dissertation, further study for reducing processing time and steps should be performed. Spin coating process with reduced annealing time, ink-jet printing, roll to roll processing, and spraying methods for film deposition can be several of the candidates. However, it should be noted that the film quality of these processes have not outperformed that of processes used in our study so far. Hence, efforts for improving the quality of films should be addressed before adapting these technologies. As an alternative, based on the barrier structures developed in this study, optimizing the dimension of individual films or replacing some of the constituent films with others deposited by different processes can be considered. In addition to reducing processing steps and time, studies concerning the reliable and continuous yield of encapsulation process and effort to decrease failure rate should be performed because the increased failure rate of processing leads to increases in manufacturing cost. The capability for producing homogeneous film on large areas should be addressed to realize low cost manufacturing of encapsulation. When encapsulation barrier layers can be processed with highly efficient organic electronics, the realization of plastic electronics is expected to become a reality in our daily lives.

APPENDIX - QUARTZ CRYSTAL MICROBALENCE

8.1 Basic theory

To measure *D* and *S* of parylene which was used as an organic film in the multilayer structure, a quartz crystal microbalance (QCM) was employed. Details concerning QCM measurements and its application to transport property measurements are well explained in other references. [127,128] In this appendix, we briefly explain how to calculate *D* and *S* using QCM. Mass uptake can be measured by monitoring the frequency change of a quartz crystal resonator coated with a film of interest based on the Sauerbrey equation,

$$\Delta m = \frac{\Delta f}{C_f} A \tag{A.1}$$

where, Δm, Δf, C_f, A are mass change, frequency change, integral sensitivity constant (0.056 Hz/ng/cm^2), and the active oscillation area (34.19 mm^2), respectively.

In our application, mass change is due to water absorption in the parylene film and we assume that this process follows 2nd Fick's law for 1 dimensional transport,

$$\frac{\partial c}{\partial t} = D \frac{\partial^2 c}{\partial x^2} \tag{A.2}$$

With boundary conditions of fixed concentration on one side and zero flux on the other side, solutions can be derived as follows,[127]

$$\frac{M_t}{M_\infty} = 2\left(\frac{Dt}{L^2}\right)^{1/2}\left(\frac{1}{\pi^{1/2}} + 2\sum_{n=1}^{\infty}(-1)^n \, ierfc\frac{nL}{\sqrt{Dt}}\right) \tag{A.3}$$

where M_t and M_∞ are the mass gains at any time, t, and at equilibrium, respectively. L is the thickness of film. At short times, this solution can be simplified to[128]

$$\frac{M_t}{M_\infty} = \frac{2}{L}\left(\frac{Dt}{\pi}\right)^{1/2} \tag{A.4}$$

This equation is often referred to as the 'short time' equation and is used to estimate Fickian *D*. Hence, *D* of parylene film can be determined from the initial slope of the absorption curve ($M_t/M_\infty < 0.6$)[128] which will be shown in the next section.

Next, the solubility of water vapor in parylene can be calculated based on the following expression,[129]

$$S = \frac{M_\infty}{M_0}\frac{\rho_{polymer}}{MW_{penetrant}} \times \frac{22,414}{p} \tag{A.5}$$

M_∞ *(the equilibrium mass uptake)* can be measured using QCM experiments. M_o, $\rho_{polymer}$, $MW_{penetrant}$, and p are the mass of water-free parylene, density of parylene, water molecular weight, and water vapor pressure, respectively.

To perform these experiments, quartz crystal resonantors were coated with 1 μm and 3 μm thick parylene layers. The thicker films ensured enough signal to noise ratio from mass uptake and to ensure that our D and S were not a function of sample thickness. The system utilized was a Maxtek RQCM system with a flow cell attachment for exposing the sample to dry nitrogen or humid nitrogen (Figure A.1). To create humid nitrogen, dry nitrogen was bubbled through two bubbler systems in order to saturate the nitrogen before entering the flow cell. A second line allowed only dry nitrogen to enter the flow cell. By exposing the surface of the film to either dry nitrogen or humid saturated nitrogen, the boundary condition on the film was changed and the mass uptake or decrease could be measured by monitoring the frequency change of the quartz crystal resonator.

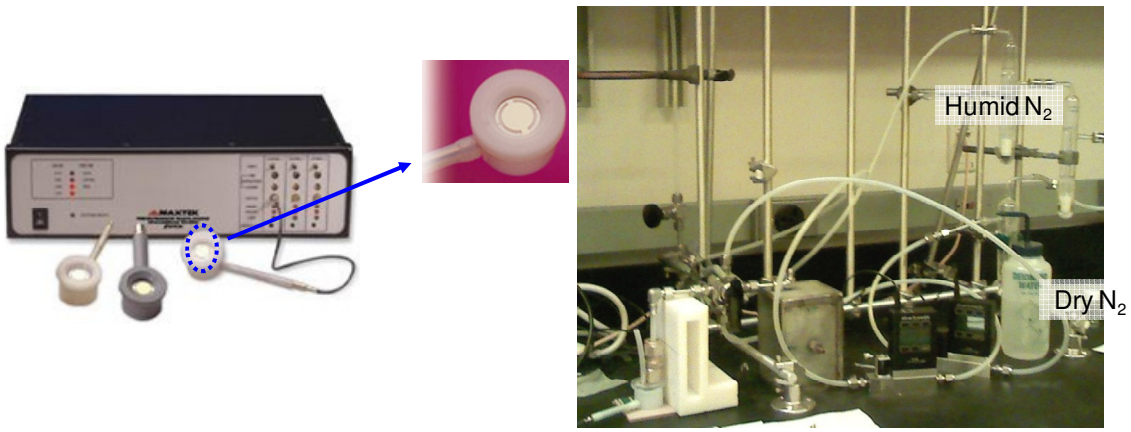

Figure A.1 (left) Picture showing the Maxtek RQCM quartz crystal microbalance measurement system with flow cell (middle). On the right, a depiction of the test system with both dry and humid nitrogen which can be passed into the flow cell.

8.2 Experimental results

The frequency change as a function of time is plotted in Figure A.2 (a) and these were converted into M_t/M_∞ as a function of time based on Sauerbrey equation. As shown in the Figure A.2 (a), frequency drops as the flow change from dry N_2 into humid N_2. Experiment was conducted at 20 °C and the RH of humid N_2 was 50 %. Fractional water vapor uptake was plotted as a function of time in Figure A.2 (b). Plotted data exhibited Fickian diffusion behavior in the initial short time phase of the sorption process. Same cycles were repeated at least three times for consistent measurement. Determined Fickian D is based on short time approximation as previously explained. Results for both D and S of parylene for water vapor before and after 10 min anneal at 110 °C were summarized in Table A.1 and A.2. Experiments and analysis were conducted mainly by Annapoorani Sundaramoothi of Prof. Henderson's group at Georgia Institute of Technology.

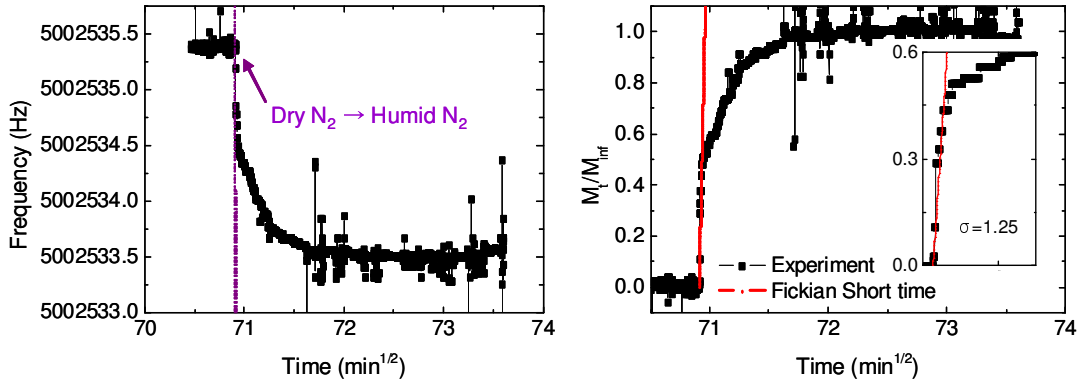

Figure A.2 (a) Typical raw data for the QCM frequency response to sorption of water in parylene film as a function of time, courtesy of Annapoorani Sundaramoothi of Prof. Henderson's group at Georgia Institute of Technology. It shows frequency drops as humid N_2 starts flow. (b) Comparison of short time Fickian predicted fractional water vapor uptake to typical observed experimental mass uptake in parylene.

Table A.1 Estimated *D* of parylene for water sorption before and after annealing.

Test #	Diffusion coefficient, *D* (cm^2/s)	
	Before annealing	After annealing
1	7.4×10^{-8}	1.0×10^{-8}
2	8.3×10^{-8}	1.5×10^{-8}
3	1.1×10^{-9}	1.3×10^{-8}
Average	8.0×10^{-9}	1.2×10^{-8}
STDV	1.0×10^{-9}	4.0×10^{-9}
95 % confidence	1.8×10^{-9}	2.6×10^{-9}

Table A.2 Determined *S* of parylene for water sorption before and after annealing.

Test #	Solubility coefficient, *S* (g/cm^3atm)	
	Before annealing	After annealing
1	0.025	0.029
2	0.021	0.027
3	0.028	0.025
Average	8.0×10^{-9}	1.2×10^{-8}
STDV	1.0×10^{-9}	4.0×10^{-9}

References

[1] J. Shen, D. Wang, E. Langlois, W. A. Barrow, P. J. Green, C. W. Tang, J. Shi, *Synth. Met.* 2000, *111,* 233.
[2] S. T. Lee, Z. Q. Gao, L. S. Hung, *Appl. Phys. Lett.* 1999, *75,* 1404.
[3] Z. D. Popovic, H. Aziz, N. X. Hu, A. M. Hor, G. Xu, *Synth. Met.* 2000, *111,* 229.
[4] Y. C. Luo, H. Aziz, Z. D. Popovic, G. Xu, *J. Appl. Phys.* 2007, *101,* 34510.
[5] H. Aziz, Z. D. Popovic, *Chem. Mater.* 2004, *16,* 4522.
[6] H. Aziz, Z. D. Popovic, N. X. Hu, A. M. Hor, G. Xu, *Science* 1999, *283,* 1900.
[7] Z. D. Popovic, H. Aziz, *IEEE J. Sel. Top. Quantum Electron.* 2002, *8,* 362.
[8] J. McElvain, H. Antoniadis, M. R. Hueschen, J. N. Miller, D. M. Roitman, J. R. Sheats, R. L. Moon, *J. Appl. Phys.* 1996, *80,* 6002.
[9] J. Ficker, H. von Seggern, H. Rost, W. Fix, W. Clemens, I. McCulloch, *Appl. Phys. Lett.* 2004, *85,* 1377.
[10] M. I. Arroyovillan, G. A. Diazquijada, M. S. A. Abdou, S. Holdcroft, *Macromolecules* 1995, *28,* 975.
[11] C. J. Brabec, A. Cravino, D. Meissner, N. S. Sariciftci, M. T. Rispens, L. Sanchez, J. C. Hummelen, T. Fromherz, *Thin Solid Films* 2002, *403,* 368.
[12] L. M. Do, E. M. Han, Y. Niidome, M. Fujihira, T. Kanno, S. Yoshida, A. Maeda, A. J. Ikushima, *J. Appl. Phys.* 1994, *76,* 5118.
[13] H. Aziz, Z. Popovic, S. Xie, A. M. Hor, N. X. Hu, C. Tripp, G. Xu, *Appl. Phys. Lett.* 1998, *72,* 756.
[14] M. Schaer, F. Nuesch, D. Berner, W. Leo, L. Zuppiroli, *Advanced Functional Materials* 2001, *11,* 116.
[15] K. Horiuchi, K. Nakada, S. Uchino, S. Hashii, A. Hashimoto, N. Aoki, Y. Ochiai, M. Shimizu, *Appl. Phys. Lett.* 2002, *81,* 1911.
[16] P. E. Burrows, V. Bulovic, S. R. Forrest, L. S. Sapochak, D. M. Mccarty, M. E. Thompson, *applied physics letters* 1994, *65,* 2922.
[17] D. Kolosov, D. S. English, V. Bulovic, P. F. Barbara, S. R. Forrest, M. E. Thompson, *Journal of Applied Physics* 2001, *90,* 3242.
[18] M. S. Weaver, L. A. Michalski, K. Rajan, M. A. Rothman, J. A. Silvernail, J. J. Brown, P. E. Burrows, G. L. Graff, M. E. Gross, P. M. Martin, M. Hall, E. Mast, C. Bonham, W. Bennett, M. Zumhoff, *Applied Physics Letters* 2002, *81,* 2929.
[19] J. S. Lewis, M. S. Weaver, *IEEE Journal of Selected Topics in Quantum Electronics* 2004, *10,* 45.
[20] B. McCormick, P. F. Baude, G. D. Verstrom, *International Patent* **2002**, *WO 02/05361 A1*.
[21] T. B. Harvye, Shi, S. Q., So, F. , *US Patent* **1998**, *5757126*.
[22] T. B. Harvye, S. Q. Shi, F. So, *US Patent* **1997**, *5686360*.
[23] M. Hanika, H. C. Langowski, U. Moosheimer, W. Peukert, *Chem. Eng. Technol.* 2003, *26,* 605.
[24] A. P. Roberts, B. M. Henry, A. P. Sutton, C. R. M. Grovenor, G. A. D. Briggs, T. Miyamoto, A. Kano, Y. Tsukahara, M. Yanaka, *Journal of Membrane Science* 2002, *208,* 75.
[25] G. L. Graff, R. E. Williford, P. E. Burrows, *J. Appl. Phys.* 2004, *96,* 1840.

[26] J. Crank, *The mathematics of Diffusion*, Clarendon University Press, **1975**.
[27] Y. G. Tropsha, N. G. Harvey, *Journal of Physical Chemistry B* 1997, *101,* 2259.
[28] B. M. Henry, F. Dinelli, K. Y. Zhao, C. R. M. Grovenor, O. V. Kolosov, G. A. D. Briggs, A. P. Roberts, R. S. Kumar, R. P. Howson, *Thin Solid Films* 1999, *356,* 500.
[29] A. G. Erlat, R. J. Spontak, R. P. Clarke, T. C. Robinson, P. D. Haaland, Y. Tropsha, N. G. Harvey, E. A. Vogler, *Journal of Physical Chemistry B* 1999, *103,* 6047.
[30] A. G. Erlat, B. C. Wang, R. J. Spontak, Y. Tropsha, K. D. Mar, D. B. Montgomery, E. A. Vogler, *Journal of Materials Research* 2000, *15,* 704.
[31] R. H. Doremus, *Glass Science*, Wiley, New York **1973**.
[32] A. S. D. Sobrinho, G. Czeremuszkin, M. Latreche, M. R. Wertheimer, *Journal of Vacuum Science & Technology A* 2000, *18,* 149.
[33] A. S. D. Sobrinho, M. Latreche, G. Czeremuszkin, J. E. Klemberg-Sapieha, M. R. Wertheimer, *Journal of Vacuum Science & Technology A* 1998, *16,* 3190.
[34] A. S. D. Sobrinho, G. Czeremuszkin, M. Latreche, G. Dennler, M. R. Wertheimer, *Surf. Coat. Technol.* 1999, *119,* 1204.
[35] M. Hanika, H. C. Langowski, U. Moosheimer, *45th Annual Tech. Conf. Proceedings*, Germany **2002**. (Year) 519.
[36] E. H. H. Jamieson, A. H. Windle, *Journal of Materials Science* 1983, *18,* 64.
[37] A. G. Erlat, B. M. Henry, J. J. Ingram, D. B. Mountain, A. McGuigan, R. P. Howson, C. R. M. Grovenor, G. A. D. Briggs, Y. Tsukahara, *Thin Solid Films* 2001, *388,* 78.
[38] M. Hanika, H. C. Langowski, U. Moosheimer, W. Peukert, *46th Annual Tech. Conf.*, San Francisco **2003**. *26* (Year) 592.
[39] W. G. Perkins, D. R. Begeal, *Journal of Chemical Physics* 1971, *54,* 1683.
[40] P. F. Carcia, R. S. McLean, M. H. Reilly, M. D. Groner, S. M. George, *Appl. Phys. Lett.* 2006, *89*.
[41] J. Meyer, P. Gorrn, F. Bertram, S. Hamwi, T. Winkler, H. H. Johannes, T. Weimann, P. Hinze, W. Kowlasky, *Advanced Materials* 2009, *21*.
[42] J. Crank, *The mathematics of diffusion*, Clarendon Press, **1975**.
[43] K. Kessler, Vol. Ph.D., Federal Technical University of Wsitzerland (E.T.H.), Zurich **1994**, 75.
[44] http://www.mocon.com/pdfperm/wvtrtestultrabarriers.pdf.
[45] R. Paetzold, A. Winnacker, D. Henseler, V. Cesari, K. Heuser, *Rev. Sci. Instrum.* 2003, *74,* 5147.
[46] G. Nisato, P. C. P. Bouten, P. J. Slikkerveer, W. D. Bennett, G. L. Graff, N. Rutherford, L. Wiese, *Proc. Int. Display Workshop/Asia Display*, **2001**. *61* (Year) 1435.
[47] M. Stevens, S. Tuomela, D. Mayer, *48th Annual Technical Conference* 2005, *505,* 189.
[48] R. Paetzold, A. Winnacker, D. Henseler, V. Cesari, K. Heuser, *Rev. Sci. Instrum.* 2003, *74,* 5147.
[49] G. Dennler, Lungenschmied, C., Neugebauer, H., Sariciftci, N. S., *Journal of Materials Research* 2005, *20,* 3224.
[50] L. Moro, N. M. Rutherford, R. J. Visser, *Proc. SPIE*, **2006**. *6334* (Year) 63340M.
[51] N. Kim, W. J. Potscavage, B. Domercq, B. Kippelen, S. Graham, *Appl. Phys. Lett.* 2009, *94,* 163308.

[52] S. H. K. Park, J. Oh, C. S. Hwang, J. I. Lee, Y. S. Yang, H. Y. Chu, K. Y. Kang, *ETRI Journal* 2005, *27,* 545.
[53] Y. Leterrier, *Progress in Materials Science* 2003, *48,* 1.
[54] A. S. D. Sobrinho, M. Latreche, G. Czeremuszkin, J. E. Klemberg-Sapieha, M. R. Wertheimer, *J. Vac. Sci. Technol., A* 1998, *16,* 3190.
[55] W. Huang, X. Wang, M. Sheng, L. Xu, F. Stubhan, L. Luo, T. Feng, X. Wang, F. Zhang, S. Zou, *Materials Science and Engineering B* 2003, *98,* 248.
[56] P. Mandlik, J. Gartside, L. Han, I. C. Cheng, S. Wagner, J. A. Silvernail, R.-Q. Ma, M. Hack, J. J. Brown, *applied physics letters* 2008, *92,* 103309.
[57] W. J. Potscavage, S. Yoo, B. Domercq, B. Kippelen, *Appl. Phys. Lett.* 2007, *90,* 253511.
[58] S. H. K. Park, J. Oh, C. S. Hwang, J. I. Lee, Y. S. Yang, H. Y. Chu, *Electrochem. Solid-State Lett.* 2005, *8,* H21.
[59] A. P. Ghosh, L. J. Gerenser, C. M. Jarman, J. E. Fornalik, *Appl. Phys. Lett.* 2005, *86,* 223503.
[60] P. F. Carcia, R. S. McLean, M. H. Reilly, M. D. Groner, S. M. George, *Appl. Phys. Lett.* 2006, *89,* 031915.
[61] J. Meyer, P. Gorrn, F. Bertram, S. Hamwi, T. Winkler, H. H. Johannes, T. Weimann, P. Hinze, T. Riedl, W. Kowalsky, *Adv. Mater.* 2009, *21,* 1.
[62] A. A. Dameron, S. D. Davidson, B. B. Burton, P. F. Carcia, R. Scott McLean, S. M. George, *J. Phys. Chem. C* 2008, *112,* 4573.
[63] S. Yoo, W. J. Potscavage, B. Domercq, S. H. Han, T. D. Li, S. C. Jones, R. Szoszkiewicz, D. Levi, E. Riedo, S. R. Marder, B. Kippelen, *Solid-State Electron.* 2007, *51,* 1367.
[64] J. Fenrych, E. C. Reynhardt, I. Basson, *Powder Diffraction* 1997, *12,* 49.
[65] H. Jung, T. Lim, Y. Choi, M. Yi, J. Won, S. Pyo, *Appl. Phys. Lett.* 2008, *92*.
[66] S. Cho, K. Lee, A. J. Heeger, *Adv. Mater.* 2009, *21,* 1.
[67] C. C. Chiang, D. S. Wuu, H. B. Lin, Y. P. Chen, T. N. Chen, Y. C. Lin, C. C. Wu, W. C. Chen, T. H. Jaw, R. H. Horng, *Surf. Coat. Technol.* 2006, *200,* 5843.
[68] T. N. Chen, D. S. Wuu, C. C. Wu, C. C. Chiang, Y. P. Chen, R. H. Horng, *Plasma Processes and Polymers* 2007, *4,* 180.
[69] M. S. Weaver, A. B. Chwang, M. A. Rothman, J. A. Silvernail, M. G. Hack, J. J. Brown, P. E. Burrows, G. L. Graff, M. E. Gross, P. M. Martin, M. Hall, E. Mast, C. C. Bonham, W. D. Bennett, M. Zumhoff, *Proc. SPIE Int. Soc. Opt. Eng.*, **2002**. *4712* (Year) 237.
[70] A. B. Chwang, M. A. Rothman, S. Y. Mao, R. H. Hewitt, M. S. Weaver, J. A. Silvernail, K. Rajan, M. Hack, J. J. Brown, X. Chu, L. Moro, T. Krajewski, N. Rutherford, *applied physics letters* 2003, *83,* 413.
[71] T.-N. Chen, D.-S. Wuu, C.-C. Wu, C.-C. Chiang, Y.-P. Chen, R.-H. Horng, *J. Electrochem. Soc.* 2006, *153,* F244.
[72] J. D. Affinito, M. E. Gross, C. A. Coronado, G. L. Graff, E. N. Greenwell, P. M. Martin, *Thin Solid Films* 1996, *291,* 63.
[73] J. Greener, K. C. Ng, K. M. Vaeth, T. M. Smith, *Journal of Applied Polymer Science* 2007, *106,* 3534.
[74] G. Nisato, *Proc. Soc. Info. Display Symp., Digest Tech.* 2003, *34,* 550.

[75] M. Yan, T. W. Kim, A. G. Erlat, M. Pellow, D. F. Foust, H. Liu, M. Schaepkens, C. M. Heller, P. A. McConnelee, T. P. Feist, A. R. Duggal, *Proc. IEEE* 2005, *93,* 1468.
[76] T. W. Kim, M. Yan, G. Erlat, P. A. McConnelee, M. Pellow, J. Deluca, T. P. Feist, A. R. Duggal, M. Schaepkens, *J. Vac. Sci. Technol., A* 2005, *23,* 971.
[77] C. Lungenschmied, G. Dennler, H. Neugebauer, S. N. Sariciftci, M. Glatthaar, T. Meyer, A. Meyer, *Sol. Energy Mater. Sol. Cells* 2007, *91,* 379.
[78] J. A. Hauch, P. Schilinsky, S. A. Choulis, R. Childers, M. Biele, C. J. Brabec, *Sol. Energy Mater. Sol. Cells* 2008, *92,* 727.
[79] J. S. Lewis, *Materials today* 2006, *9,* 38.
[80] M. Yanaka, Y. Kato, Y. Tsukahara, N. Takeda, *Thin Solid Films* 1999, *356,* 337.
[81] D. R. Cairns, R. P. Witte, D. K. Sparacin, S. M. Sachsman, D. C. Paine, G. P. Crawford, R. R. Newton, *Appl. Phys. Lett.* 2000, *76,* 1425.
[82] S. K. Park, J. I. Han, D. G. Moon, W. K. Kim, *Jpn. J. Appl. Phys.* 2003, *42,* 623.
[83] J. Lewis, *Materials Today* 2006, *9,* 38.
[84] S. Grego, J. Lewis, E. Vick, D. Temple, *Journal of the Society for Information Display* 2005, *13,* 575.
[85] G. Rochat, Y. Leterrier, P. Fayet, J. A. E. Manson, *Thin Solid Films* 2003, *437,* 204.
[86] M. Yanaka, B. M. Henry, A. P. Roberts, C. R. M. Grovenor, G. A. D. Briggs, A. P. Sutton, T. Miyamoto, Y. Tsukahara, N. Takeda, R. J. Chater, *Thin Solid Films* 2001, *397,* 176.
[87] J. Andersons, Y. Leterrier, I. Fescenko, *Thin Solid Films* 2003, *434,* 203.
[88] S. Grego, J. Lewis, E. Vick, D. Temple, *Thin Solid Films* 2007, *515,* 4745.
[89] Y. Leterrier, P. Bouten, X. Jiang, in *Layer mechanics, Experimental methods and models*, Information society technologies, **2001**, 1.
[90] Z. Suo, E. Y. Ma, H. Gleskova, S. Wagner, *Appl. Phys. Lett.* 1999, *74,* 1177.
[91] S. K. Park, J. I. Han, D. G. Moon, W. K. Kim, *Jpn. J. Appl. Phys.* 2003, *42,* 623.
[92] T. Sekitani, S. Iba, Y. Kato, Y. Noguchi, T. Someya, T. Sakurai, *Appl. Phys. Lett.* 2005, *87*.
[93] D. S. Wuu, W. C. Lo, C. C. Chiang, H. B. Lin, L. S. Chang, R. H. Horng, C. L. Huang, Y. J. Gao, *Surf. Coat. Technol.* 2005, *197,* 253.
[94] A. P. Ghosh, L. J. Gerenser, C. M. Jarman, J. E. Fornalik, *Appl. Phys. Lett.* 2005, *86*.
[95] M. D. Groner, J. W. Elam, F. H. Fabreguette, S. M. George, *Thin Solid Films* 2002, *413,* 186.
[96] B. S. Lim, A. Rahtu, R. G. Gordon, *Nature Materials* 2003, *2,* 749.
[97] M. D. Groner, F. H. Fabreguette, J. W. Elam, S. M. George, *Chem. Mater.* 2004, *16,* 639.
[98] H. J. Ueng, D. B. Janes, K. J. Webb, *Ieee Transactions on Electron Devices* 2001, *48,* 758.
[99] S. D. Phillips, B. Toman, W. T. Estler, *Journal of Research of the National Institute of Standards and Technology* 2008, *113,* 143.
[100] W. C. Oliver, G. M. Pharr, *Journal of Materials Research* 1992, *7,* 1564.
[101] J. Thurn, R. F. Cook, M. Kamarajugadda, S. P. Bozeman, L. C. Stearns, *Journal of Applied Physics* 2004, *95,* 967.

[102] A. Bieder, V. Gondoin, Y. Leterrier, G. Tornare, P. R. von Rohr, J. A. E. Manson, *Thin Solid Films* 2007, *515,* 5430.
[103] L. B. Freund, J. A. Floro, E. Chason, *Appl. Phys. Lett.* 1999, *74,* 1987.
[104] S. Yoo, B. Domercq, B. Kippelen, *Appl. Phys. Lett.* 2004, *85,* 5427.
[105] C. J. Brabec, J. A. Hauch, P. Schilinsky, C. Waldauf, *Mrs Bulletin* 2005, *30,* 50.
[106] T. Toyama, T. Kitagawa, W. Yoshida, Y. Sobajima, H. Okamoto, *Journal of Non-Crystalline Solids* 2006, *352,* 941.
[107] A. Bieder, A. Gruniger, P. R. von Rohr, *Surface & Coatings Technology* 2005, *200,* 928.
[108] H. Kim, K. Najafi, *Journal of Microelectromechanical Systems* 2005, *14,* 1347.
[109] W. J. Koros, D. R. Paul, *Abstracts of Papers of the American Chemical Society* 1978, *176,* 36.
[110] R. Thyen, A. Weber, C. P. Klages, *Surface & Coatings Technology* 1997, *97,* 426.
[111] R. Ash, R. M. Barrer, D. G. Palmer, *British Journal of Applied Physics* 1965, *16,* 873.
[112] R. Ash, R. M. Barrer, J. H. Petropoulos, *British Journal of Applied Physics* 1963, *14,* 854.
[113] J. Brandrup, E. H. Immergut, *Polymer handbook, 3rd Ed.*, Wiley, New York **1989**.
[114] S. Gorhkali, D. R. Cairns, G. P. Crawford, *Soc. Inform. Display Symp.*, **2003**. *34* (Year) 1332.
[115] M. D. Groner, S. M. George, R. S. McLean, P. F. Carcia, *Applied Physics Letters* 2006, *88*.
[116] M. Vogt, R. Hauptmann, *Surf. Coat. Technol.* 1995, *75,* 676.
[117] S. Robles, E. Yieh, B. C. Nguyen, *J. Electrochem. Soc.* 1995, *142,* 580.
[118] O. L. Anderson, D. A. Stuart, *J. Am. Ceram. Soc.* 1964, *37,* 573.
[119] M. F. Doerner, W. D. Nix, *Crc Critical Reviews in Solid State and Materials Sciences* 1988, *14,* 225.
[120] W. H. Chuang, T. Luger, R. K. Fettig, R. Ghodssi, *Journal of Microelectromechanical Systems* 2004, *13,* 870.
[121] E. WU, Y. A. J. D., S. Ching-An, *54th electronic components & technology conference* Las Vegas NV **2004**. (Year) 414.
[122] T. N. Chen, D. S. Wuu, C. C. Wu, C. C. Chiang, Y. P. Chen, R. H. Horng, *Journal of the Electrochemical Society* 2006, *153,* F244.
[123] A. B. Horsfall, K. Wang, J. M. M. Dos-Santos, S. M. Soare, S. J. Bull, N. G. Wright, A. G. O'Neill, J. G. Terry, A. J. Walton, A. M. Gundlach, J. T. M. Stevenson, *Ieee Transactions on Device and Materials Reliability* 2004, *4,* 482.
[124] J. Kawashima, Y. Yamada, I. Hirabayashi, *Physica C* 1998, *306,* 114.
[125] K. M. Conley, J. E. Ritter, T. J. Lardner, *J. Mater. Res.* 1992, *7,* 2621.
[126] A. Sugimoto, H. Ochi, S. Fujimura, A. Yoshida, T. Miyadera, M. Tsuchida, *IEEE J. Sel. Top. Quantum Electron.* 2004, *10,* 107.
[127] J. Crank, G. S. Park, *Method of Measurement. In Diffusion in Polymers*, Academic press: London, **1968**.
[128] C. Henderson, C. Berger, *Polymer* 2003, *44,* 2101.
[129] C. McDowell, in *Chemical engineering*, Vol. 98, **1998**.

VITA

Namsu Kim

Namsu Kim received his B.S. degree in mechanical engineering from Hanyang University, Seoul, Korea in 1998 and his M.S. degree in the same major from the University of Texas at Austin in 2004. He is currently working on his Ph.D. degree in mechanical engineering at Georgia Institute of Technology. His current research areas are thin-film processing and characterization with a primary emphasis on developing and studying the reliability of encapsulation for organic electronics. Also, he investigates the mechanics of thin films for flexible electronics.